Turbulent Boundary Layer Flow Over Two-Dimensional Bottom Roughness Elements

by

Analía Inés Barrantes

Submitted to the Department of Civil and Environmental Engineering
in partial fulfillment of the requirements for the degree of

Doctor of Science in the field of hydrodynamics

at the

MASSACHUSETTS INSTITUTE OF TECHNOLOGY

February 1997

Author .....
Department of Civil and Environmental Engineering
September 12, 1996

Certified by .....
Ole S. Madsen
Professor, Civil and Environmental Engineering
Thesis Supervisor

Accepted by .....
Joseph M. Sussman
Chairman, Departmental Committee on Graduate Studies

Turbulent Boundary Layer Flow Over Two-Dimensional Bottom Roughness Elements

by

Analía Inés Barrantes

Submitted to the Department of Civil and Environmental Engineering
on September 12, 1996, in partial fulfillment of the
requirements for the degree of
Doctor of Science in the field of hydrodynamics

Abstract

Waves and current do not generally propagate in the same direction in a coastal environment. When the near-bottom flow is wave dominated, a two-dimensional ripple bedform develops on the bottom. Accordingly, the ripple axis is perpendicular to the direction of wave propagation and the current is incident at angle to this axis. Field observations have shown that, in this typical situation, the bottom roughness experienced by the waves is different from the bottom roughness experienced by the current. Moreover, they have revealed that the bottom roughness experienced by the current depends on the angle between the ripple axis and the direction of the current.

The goal of this thesis is to understand the nature of the near-bottom flow that is produced when a wave and a current are propagating in different directions over a wave-generated ripple bedform.

For this purpose laboratory experiments were performed in the existing wave flume in Parsons Laboratory. The combined wave and current flow in this flume consist of waves and a current propagating in the same direction. The ripple bedform was represented by artificial roughness elements that covered the bottom of the flume. They consisted of triangular bars of 1.5 cm height that were placed at 10 cm intervals at an angle $\theta = 0^o, 30^o, 45^o$ and 60^o, where θ is the angle between the ripple axis and the direction perpendicular to the incident flow. This set-up is not completely realistic because the artificial roughness elements, which represent the wave-generated ripples, in principle, should be aligned with the wave crests. It has nonetheless made it possible to perform critical experiments to characterize the near-bottom flow that results from ripples at an angle to the incident current. The physical insights gained from the experimental results have in turn allowed us to develop a simple model capable of describing quantitatively field data.

Pure wave energy attenuation experiments were performed to obtain the energy friction factor which was expressed in terms of a drag force representing the bottom resistance. The angle dependence of the energy friction factor obtained in the experiments could be explained by assuming that the drag force scales proportionally to the square of the component of the velocity in the direction perpendicular to the

ripple axis, and that the drag coefficient is independent of the angle.

Measurements of the three components of the velocity were performed for a pure current, pure waves, and combined wave and current flow. The velocity profiles measured in the pure current experiments were analyzed using the log-profile method to obtain the bottom roughness. The analysis showed that the bottom roughness experienced by the incident flow depends strongly on the angle of incidence, decreasing by more than one order of magnitude when θ varies from 0^o to 60^o. In contrast, the bottom roughness experienced by the component of the flow in the direction perpendicular to the ripple axis was found to be constant, corroborating the conclusion obtained in the pure wave attenuation experiments where a drag coefficient independent of angle was used to represent the drag force. These experiments also revealed the existence of a component of the velocity in the direction perpendicular to the incident flow that indicates that the velocity is turned towards the ripple axis as the bottom is approached.

The velocity was measured in the pure wave and wave-current experiments when the angle was 45^o. The first harmonic wave amplitude and phase showed that the profiles of the component of the velocity in the direction parallel to the ripple axis present a thiner wave boundary layer thickness than the one present in the profiles of the component of the velocity in the direction perpendicular to the ripple axis. The differences in the wave boundary layer thickness is an indication of the difference in the roughness experienced by the component of the flow in the direction parallel and perpendicular to the ripple axis.

The experimental results obtained in the thesis have provided the basis to develop a general model to predict the near-bottom flow and angle dependence of the bottom roughness to be applied to the field. The model is basically a modification of the Grant-Madsen model (1979) and assumes that the wave-current interaction depends on the direction.

The model predictions are tested against laboratory and field experiments of combined wave-current flows propagating in different directions. It is concluded that the model is able to reproduce quantitatively the observed bottom roughness dependence on the angle between the waves and the current in the limited set of experiments available at present.

Thesis Supervisor: Ole S. Madsen
Title: Professor, Civil and Environmental Engineering

Acknowledgments

The research presented in this thesis was sponsored by the National Science Foundation under the grant No: OCE-9314366.

I first would like to thank my thesis advisor, Professor Ole Madsen, for all his encouragement, his valuable guidance, and his patient support during these years in MIT. He has always been enthusiastic and full of good ideas that have been extremely helpful for my thesis. I feel that I have learned a lot from having been exposed to his insightful way of approaching complex physical problems. I also thank him for having been so understanding during this last stretch of my thesis, helping me cross the finish line.

I would like to thank the other members of my thesis committee, Professor Heidi Nepf and Dr. John Trowbridge, for their contributions and advise. Thank you Heidi for your time helping me to solve numerous problems in the lab.

I feel fortunate to have done my thesis in Parsons Lab where I had the opportunity to learn so much from all its professors. I am grateful to Professor Ken Melville who supported me and introduced me to the wonderful world of waves during my first year in MIT. I thank Sheila Frankel for her effort running the lab and her understanding. Thanks to Pat Dixon for her warm welcome to the lab. I also want to thank Veronica, Karen and Vicky for their time. I am very grateful to Professor Rubén Rosales for having initially advised me to do my thesis in Parsons Lab.

I have met many people who helped me and shared happy moments during the course of my thesis in Parsons Lab. I will always remember with gratitude and affection the old generation, Eric, Francis and Mark, who helped me to get started in the lab. Sammarco, thank you for the coffee breaks! I also would like to thank the students who shared with me the old office in the first floor, Susan, Becky, Kent, Ziad and Phil for their camaraderie. Thanks also to the new office-mates, Jennifer and Paulo who helped me through the stories of Sanjay.

I am specially grateful to Paul Mathisen for his patience in teaching me the basic tools needed to set-up the experiments. I will always remember the immensely helpful

technical help of Hoang and his advise and support when nothing worked.

Thank you all the Parsonians.

Many other friends outside Parsons Lab have supported me during these years. Thanks to the group of West Gate, Chitrus, Cari, Adro, Adri and Luis. I also want to thank, Anthea, Silvina, Marie, Quinto and Igor. I very much appreciate the encouragement of my former advisors from Argentina, Professor Marta Rosen and Professor Adriana Calvo. From far away, the support I received from my friends has been invaluable, thanks Irene, Betty and Silvia.

I am eternally grateful to my parents and sisters who have supported me with love and enthusiasm since the beginning of my studies. Finally, I thank my husband Alain, for his constant love and patience during the course of my thesis.

Contents

List of Figures

List of Tables

Chapter 1

Introduction

1.1 Introduction

Combined waves and current turbulent boundary layer flows have been extensively studied during the last few decades because of their relevance in engineering and environmental applications in coastal waters.

Offshore structures are affected by the fluid forces associated with waves and currents. For this reason, the prediction of wave characteristics is of fundamental importance for engineering purposes. The modification of wave characteristics is related to the energy dissipation within the boundary layer developed above the sea bottom, which in general is turbulent. The large shear stresses present in this turbulent boundary layer are also responsible for the resuspension of bottom sediments. The resulting transport of sediments produce shoreline erosion and changes in beach profile. A knowledge of the near-bottom flow is relevant for the prediction of the transport of pollutants and chemicals in environmental applications. All these processes are intimately related to the flow dynamics of the bottom boundary layer. Therefore, the knowledge of the flow characteristics of the bottom boundary layer developed under the combined action of waves and currents is required for a complete understanding of any of these processes.

The waves observed in the shallow coastal region have a typical period of the order of 10 sec which is short in comparison to the time scale associated with the

wind generated or tidal currents that is of the order of hours. The boundary layer thickness depends on the time scale associated with the diffusion of vorticity generated at the bottom. As a result of the difference in the time scales, the boundary layer associated with the wave motion has a thickness of the order of a few centimeters while the thickness of the current boundary layer is of the order of meters or comparable with the water depth.

When waves and currents are both present, the bottom boundary layer can be characterized by two different length scales. One is the thickness of an oscillatory boundary layer (of the order of centimeters) corresponding to the wave boundary layer immediately above the bottom. The other is the thickness of a larger boundary layer above the wave boundary layer which is associated with the slowly varying flow. Within the wave boundary layer, the shear stresses and turbulence intensity are due to the combined effect of the waves and currents, while above the wave boundary layer they are due only to currents. The flow-sediment interaction takes place in the wave boundary layer. Depending on the strength of the shear stresses acting on the bottom, the bed topography can be flat or rippled. In a wave dominated environment the bottom bedforms have a symmetrical shape and their axes are aligned with the wave crests. The presence of the ripples induces flow separation producing an increase of the effective bottom roughness felt by the flow. In the absence of ripples, the characteristic scale of the bottom roughness is the grain diameter (of the order of 0.1 mm) and, in the presence of ripples, it is the ripple height (of the order of 1 cm). The appearance of ripples produces an increase in the shear stresses and energy dissipation, which change the near-bottom flow characteristics. In this way, any coastal process related to the near-bottom flow characteristics, such as wave attenuation, sediment transport, etc, is intimately related to the bottom bedform, or equivalently, to the bottom roughness.

Several theoretical models describing the turbulent boundary layer under combined waves and currents flows have been proposed. The simplest models are those that solves the turbulence closure problem by relating the Reynolds stresses to the gradient of the velocity through an eddy viscosity (Prandtl's mixing length theory).

A time-invariant eddy viscosity was used in the wave-current problem by Lundgren (1972), Smith (1977), Grant and Madsen (1979 and 1986), Tanaka and Shuto (1981) and Christoffersen and Jonsson (1985). These models solved the linearized turbulent boundary layer equation where the wave is assumed to be a simple periodic progressive wave. The use of a time-invariant eddy viscosity makes it possible to separate the equation into an equation for the time -dependent (wave) component of the velocity and an equation for the steady (current) component. The bedform geometry is treated as an equivalent bottom roughness in the formulation and is used to specify the non-slip boundary condition of the velocity at the bottom.

The vertical distribution of the eddy viscosity is different in each of these models, but the bottom roughness used is assumed to be the same for the wave and the current. The assumption of a single roughness length scale to characterize the bottom boundary layers for pure currents, pure waves, and combined wave and current flows has been extensively used but has not been verified until recently, when experiments of turbulent boundary layer flow under combined co-directional waves and currents over a rippled bed were performed by Mathisen and Madsen (1996). The results obtained in these experiments showed that the bottom roughness for pure waves, pure currents and combined wave and current flows is characterized by the same length scale provided waves and currents are co-directional and perpendicular to the ripple crests.

1.2 Motivation

In the coastal environment, waves and current are generally not in the same direction. In shallow water, waves tend to be perpendicular to the shore due to refraction, whereas currents tend to be more or less parallel to the shore. Field observations have shown that in a wave dominated environment, a two-dimensional ripple bedform aligned with the wave crests is formed. The ripple axis is perpendicular to the direction of wave propagation and at an angle to the incident current. Under this situation it is not clear if the assumption of a single bottom roughness scale for pure

waves, pure currents and wave and current flows is still valid.

The bottom roughness consists of three elements: the skin friction contribution associated with the sediment grains, the roughness associated with the turbulent dissipation in the near-bed sediment transport layer and the form drag contribution associated with flow separation around the individual roughness elements (Grant and Madsen (1982), Wiberg and Rubin (1989)).

For rough turbulent flow, the roughness associated with skin friction is of the order of the grain diameter $\approx$ 0.1 mm. If the bottom is rippled, or if there is significant sediment transport, the skin friction contribution can be neglected. If the bottom shear stresses are not strong enough to produce a considerable transport of sediment, the total bottom roughness can be assumed to be given only by the form drag contribution.

Let us consider an idealized situation where the waves have interacted with the sediment grains producing ripples on the bottom. The wave is removed and a steady current is assumed to be flowing in the same direction as the wave, *i.e*, in the direction perpendicular to the rippled bed as shown in Figure 1-1 (a). Flow separation occurs at the crest of the ripples. The difference of pressure between the front and the back side of the ripples induces a pressure drag force. This resistance force exerted on the fluid can be translated into an equivalent bottom roughness length scale (Madsen 1991). It is reasonable to assume that the resulting flow resistance acting on the pure current is similar to that exerted on the pure wave motion. Therefore, the bottom roughness experienced by the current is expected to be of the same order as that experienced by the pure wave flow, as was proved experimentally by Mathisen and Madsen (1996).

When the current is incident at an angle with respect to the ripple axis, as shown in Figure 1-1 (b), the flow effectively encounters a less steep ripple than in the case of normal incidence. Flow separation is reduced, producing a smaller resistance force acting on the fluid. In this case the bottom roughness is expected to be smaller than the one experienced by the same current when it is incident perpendicular to the ripple axis.

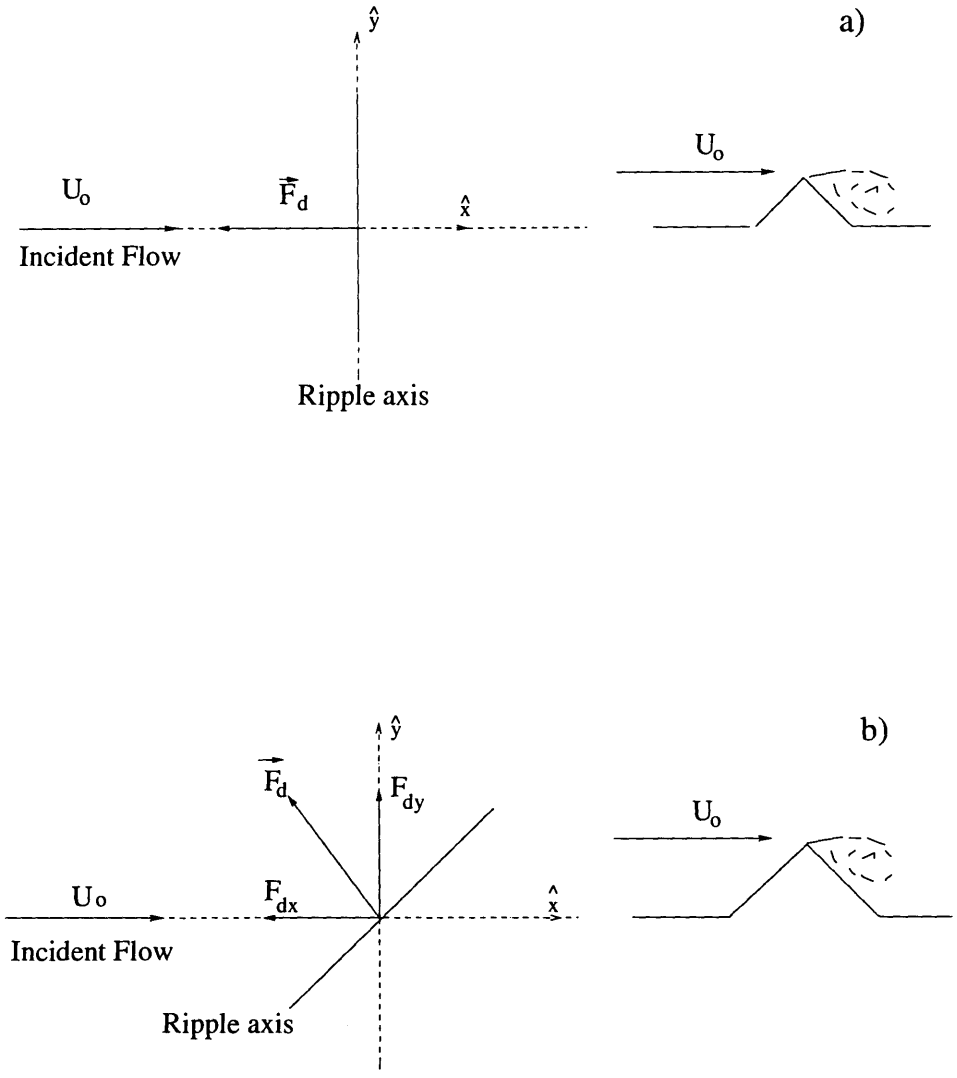

Figure 1-1: a) Flow incident perpendicular to the ripple axis. b) Flow incident at an angle to the ripple axis.

This simple argument based on the concept of a drag force suggests that the bottom roughness experienced by the current will depend on the angle between the current direction and the ripple axis, *i.e.*, on the angle between the waves and currents. This conclusion is supported by field experiments performed on the inner shelf of Northern California by Drake and Cacchione (1992). The horizontal components of the velocity were measured up to 1 m above the bottom. The bottom topography was also characterized by symmetrical wave generated ripples. The analysis of the experiments revealed a correlation between the bottom roughness and the angle between the waves and the ripple axis. More recently, Trowbridge and Agrawall (1995) obtained velocity measurements with a laser Doppler velocimeter over the rippled bed formed in a wave dominated environment in North Carolina. The experimental results qualitatively indicate a possible dependence between the bottom roughness and the angle between the waves and the currents. Sorenson (1995) analyzed data collected during a 7 day storm in North Carolina under non-wave dominated flow conditions. Based on previous ripple-geometry models of movable bed it was found that the bottom roughness depends on the angle between the waves and currents.

Another characteristic of the near-bottom flow can be anticipated from the drag force considerations presented above. It is related to the nature of the drag force which originates due to the difference of the pressure between the back and the front of the ripples. Due to its origin the drag force is directed perpendicular to the ripple axis as indicated in Figure 1-1 (b). If the current is incident at an angle with respect to the ripple axis, the component of the drag force in the direction of the incident flow, F_{dx}, is smaller than F_d. The flow resistance is decreased implying a smaller bottom roughness than the one experienced by the flow when it is incident perpendicular to the ripple axis. In addition, the component of the drag force in the direction perpendicular to the incident current, $F_{dy} \neq 0$, will cause the near-bottom flow to be deflected towards the ripple axis.

When waves and currents are not in the same direction, the argument presented above implies:

(i) the bottom roughness experienced by the current component of the velocity

will depend on the angle between the waves and the current, and, (ii) the time-independent component of the velocity will be turned towards the ripple axis as the bottom is approached from above.

The expected three-dimensional nature of the near-bottom flow makes the problem difficult to treat theoretically. Laboratory experiments seem to be the better approach to improve our understanding of this complex problem.

Several laboratory experiments of turbulent boundary layers under waves and currents have been performed for colinear waves and currents. Experiments in wave flumes over artificial bottom roughness elements have been performed by Bakker and Van Doorn (1978), and Mathisen and Madsen (1996). Kemp and Simons (1982,1983) performed experiments over smooth and rippled beds for waves propagating with and against the current.

Recently, the limiting case of waves propagating at a right angle to the current has been considered. Simons *et al.* (1992) measured the velocity and bottom shear stress under combined wave-current flow at right angles in a wave basin over fixed three-dimensional roughness (sand) . Sleath (1991) performed experiments over 3-dimensional roughness (sand and gravel). The waves were simulated by oscillating the rough bed across the unidirectional current. The same experimental set-up was used later by Ranasoma and Sleath (1994) to measure the flow under the combined action of waves and currents over a rippled bottom. The direction of the steady current was parallel to the ripple axis and at a right angle to the oscillatory flow.

At present, no laboratory experiments have been reported that considered the case of wave and currents incident at an angle.

The purpose of this thesis is to investigate experimentally the nature of the near-bottom flow that is produced when a flow is incident at an angle with respect to the axis of two-dimensional bottom roughness elements.

1.3 Outline of thesis

The experimental setup and the procedures used to perform the measurements are described in Chapter 2. An experimental setup capable of representing the problem under consideration is not easy to design. The experiments were performed in the wave flume in the R. M. Parsons Laboratory which is equipped with a programmable piston-type wavemaker and a current generation system. The combined wave and current flow in this flume consists of a wave and a current propagating in the same direction. As a reasonable representation of the real problem, the bottom of the flume was covered with artificial bedforms placed at different angles with respect to the incident flow. This set-up, however, is unrealistic because the artificial roughness elements are representing the wave-generated ripples which, in principle, must be aligned with the wave crests. Therefore, the pure wave and the combined wave and current experiments do not represent the real situation in the present experimental setup.

In Chapter 3 the pure wave and the pure current experiments are described. Pure wave energy attenuation measurements were performed. The energy friction factor obtained in these experiments is interpreted in terms of a drag force flow resistance. The main result derived from the analysis is that the drag coefficient is independent of the angle if the drag force is scaled with the square of the velocity component in the direction perpendicular to the ripple axis.

The velocity measurements performed in the pure current experiments are described and analyzed in this chapter. The three-dimensional structure of the near-bottom flow predicted by the drag force argument , *i.e*, a turning of the near-bottom velocity towards the direction parallel to the ripple axis was observed in the experiments. Similarly, the analysis of the velocity profiles shows the bottom roughness depends on the angle of incidence.

In Chapter 4 a simple theoretical model is presented to describe the near-bottom flow observed in the experiments when a pure current is incident at an angle with respect to the ripple axis. This model takes into account the presence of the walls

in the flume. Because of the finite width of the flume the near-bottom flow induced by the unbalanced drag force is not fully developed. The predicted velocity profile is able to describe the experimental observations. This model is extended to the case of the combined wave and current flow and is compared to the wave and current experiments in Chapter 5.

For the case of an infinite domain, the near-bottom flow due to the unbalanced component of the drag force is able to reach a steady state. This component of the flow is incorporated in the wave and current interaction model proposed by Grant and Madsen (1986). In Chapter 6 the predicted velocity profiles are compared to laboratory and field experiments of combined wave and current flows. Conclusions are presented in Chapter 7.

Chapter 2

Experimental Setup

2.1 Experimental Setup

The experiments were performed in the wave flume in the R. M. Parsons Laboratory. A side view of the experimental set up is shown in Figure 2-1. The flume is 28 m long, 0.76 m wide and 0.90 m deep. The sidewalls and the bottom are made of glass. The waves are generated with a piston-type programmable wavemaker located at one end of the flume. To minimize wave reflections there is a 1-on-10 sloping beach at a distance of 19.5 m from the wavemaker. The flume has a current generation system that consists of a 1200-gpm pump. The inlet is located in front of the wavemaker and the outlet is behind the beach.

A plastic honeycomb filter, 76 cm wide, 70 cm height, and 35 cm long, was used to ensure a uniform flow. The filter was placed after the inlet of the current and it was removed when needed to run wave experiments. The water depth used in the experiments was $h = 60$ cm and the corresponding depth-averaged velocity was 16 cm/sec.

The wavemaker was controlled by using a Dash-1600 D/A converter board installed in a PC. Its motion was programmed to generate Stokes waves of permanent form according to the the second order wavemaker theory proposed by Madsen (1971). The waves used had a period of T=2.63 sec and an amplitude of approximately 6 cm.

The roughness elements used in the experiments consisted on triangular bars of

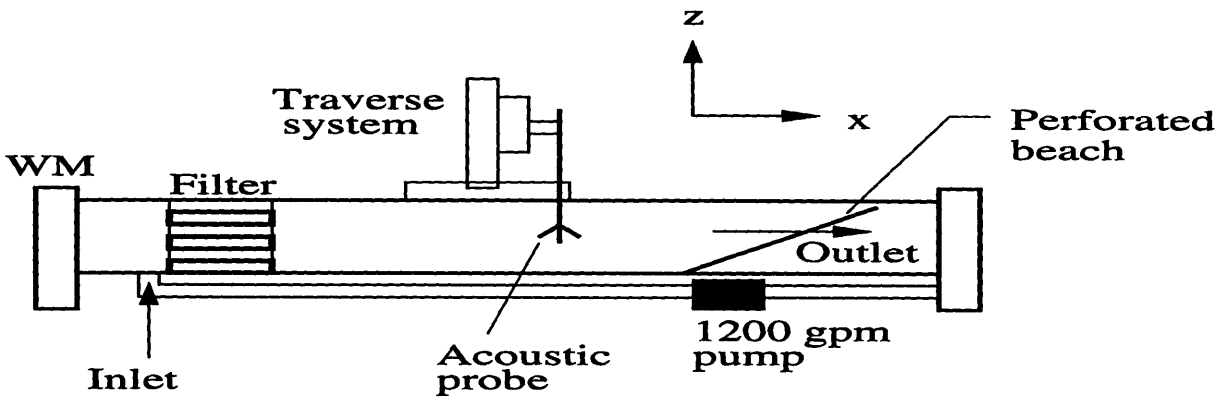

Figure 2-1: Experimental Setup

90° edge and a hight of 1.5 cm. They were placed along the bottom of the flume at 10 cm intervals, crest to crest measured perpendicular to the axes. The height and spacing of the bars were chosen to represent the bedform characteristics measured under similar wave conditions in movable bed experiments performed by Rosengaus (1987) and Mathisen (1989). In the present experiments four configurations were used depending on the angle θ between the ripple axis and the $\hat{y}$ - direction as shown in Figure 2-2. In this Figure the coordinate system is defined by the $\hat{x}$ - axis in the direction of the incident flow, and the $\hat{y}$ - axis perpendicular to the $\hat{x}$ - axis. Velocity measurements were made with a Sontek Acoustic Doppler Velocimeter (ADV). A three-axis traverse system was used to facilitate the velocity measurements. The traversing system was placed over the wave flume as indicated in Figure 2-1. Each of the axis has independent motors connected to a controller-motor amplifier. The controller is connected through a serial communication interface (RS232) to the sampling computer. The acoustic sensor of the ADV was mounted on the vertical axis of the traverse system: $\hat{z}$ - axis. The horizontal motion is produced by the other two axis: the $\hat{x}$ - axis motion is along the lengthwise direction of the flume and the $\hat{y}$ - axis motion is across the flume width.

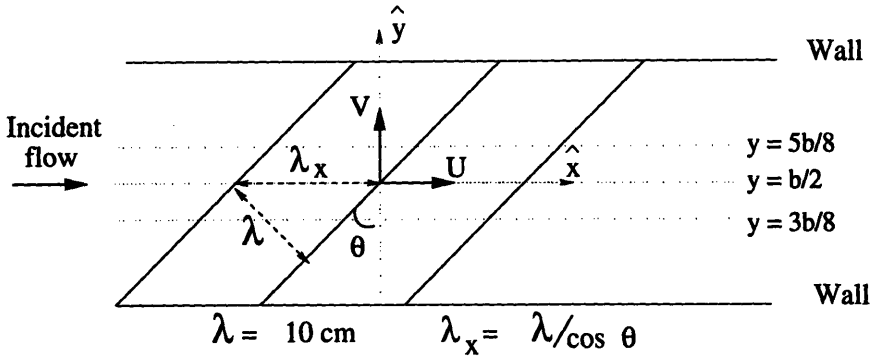

Figure 2-2: Definition of the coordinate system $(\hat{x}, \hat{y})$. θ: angle between the $\hat{y}$ - direction and the ripple axis. The flow is incident in the direction $\hat{x}$. The flume width is $b = 76$ cm. The distance between the ripples is $\lambda = 10$ cm, and the separation between two ripples measured along the $\hat{x}$ - direction is λ_x.

2.2 Summary of the Experiments

The experiments performed can be divided in three groups: pure current, pure wave and wave and current experiments and they are summarized in Tables 2.1 and 2.2.

2.2.1 Pure Current Experiments

Velocity measurements were made at the center of the flume for ripples placed at $\theta = 0^o$, 30^o, 45^o and 60^o. The velocity profiles were used to obtain an estimate of the bottom roughness. As the distance between ripples was $\lambda = 10$ cm, Figure 2-2, the spacing between two ripple crests along the $\hat{x}$ - axis was given by $\lambda_x = \lambda / \cos\theta$. Therefore, for $\theta = 0^o$ the spacing was $\lambda_x = \lambda = 10$ cm, and for $\theta = 60^o$ was $\lambda_x = 20$ cm.

For each angle θ, the first velocity profile was measured over the crest of the ripple located at $x = 0$ in Figure 2-3. The acoustic sensor was then moved along the $\hat{x}$ - axis and velocity profiles were obtained at $\Delta x \approx 1$ cm intervals from crest to crest. The maximum number of profiles measured between the two crests depend on the angle θ

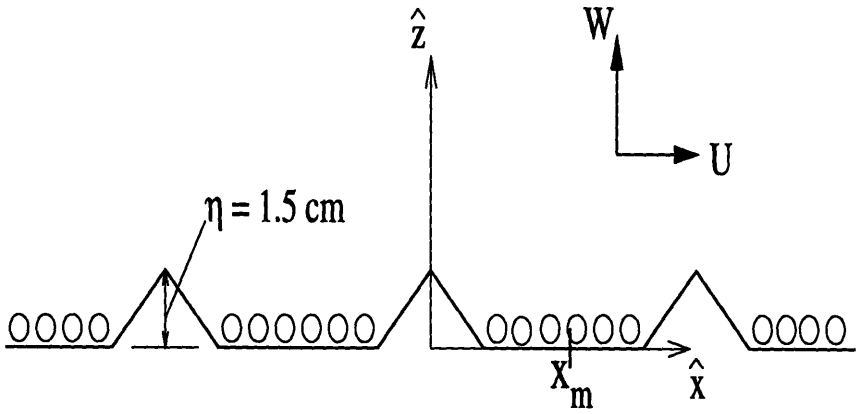

Figure 2-3: Side view of the roughness elements when the bottom of the flume is covered by a monolayer of beads of diameter $d = 0.64$ cm. The velocity profiles were measured along the $\hat{x}$ - axis at a distance x_m from the first crest located at $x = 0$.

and is given by $N_{max} = \lambda_x/\Delta x + 1$, where the profiles measured over the two crests are taken into account. For example, for $\theta = 0^o$ the number of profiles measured was $N_{max} = 11$, and for $\theta = 60^o$ was $N_{max} = 21$. The minimum distance above the bottom at which the velocity was measured was $z = 0.3$ cm and the highest elevation was $z = 50$ cm.

When the ripples were placed at an angle with respect to the incident current a strong transverse flow was established. In order to obtain a more complete characterization of the flow in these cases and to study the possible variability of the estimate of the bottom roughness, measurements were repeated at $y = 3b/8$ and $y = 5b/8$, where $b = 76$ cm is the flume width. Only for $\theta = 45^o$ were the measurements carried out at 1 cm intervals at the three transverse locations, *i.e.* the number of profiles measured between the two crests was N_{max}. For the other two angles less profiles were measured at $y = 3b/8$ and $y = 5b/8$. The number of profiles measured in each of the experiments performed is listed in Tables 2.1 and 2.2 and is denoted by N. The ratio between the distance from the first crest where the velocity profile was measured, x_m, and Δ_x is shown in the last column of this table. For example, $x_m/\Delta_x = 6$, indicates that the velocity profile was measured at approximately 6 cm from the first crest.

These experiments were performed both with and without a monolayer of beads

Table A)						
No Beads	θ	y/b	Δ_x	N_{max}	N	x_m/Δ_x
	0	1/2	1.00	11	11	0 to 10
		3/8			4	0, 6, 8, 11
	30	1/2	1.05	12	12	0 to 11
		5/8			4	0, 6, 8, 11
		3/8			15	0 to 14
	45	1/2	1.01	15	15	0 to 14
		5/8			15	0 to 14
		3/8			5	0, 2, 10, 18, 20
	60	1/2	1.00	21	21	0 to 20
		5/8			5	0, 2, 10, 18, 20
Table B)						
Beads	θ	y/b	Δ_x	N_{max}	N	x_m/Δ_x
	0	1/2	1.00	11	11	0 to 10
		3/8			6	0, 3, 5, 6, 8, 11
	30	1/2	1.05	12	12	0 to 11
		5/8			6	0, 3, 5, 6, 8, 11
		3/8			15	0 to 14
	45	1/2	1.01	15	15	0 to 14
		5/8			15	0 to 14
		3/8			5	0, 6, 10, 12, 16, 20
	60	1/2	1.00	21	21	0 to 20
		5/8			5	0, 6, 10, 12, 16, 20

Table 2.1: Summary of the pure current experiments WITH FILTER. N_{max} = maximum number of profiles measured in an experiment. N = the total number of profiles measured between two crests. x_m = the distance from the first crest where the velocity profile was measured. $\Delta_x = 10/((N_{max} - 1)\cos\theta)$ cm. Table A) Experiments without beads. Table B) Experiments with beads

of diameter $d = 0.64$ cm placed between the ripples, as shown in Figure 2-3.

For the wave and wave and current experiments the filter system was removed from the flume. Pure current experiments without the filter were performed to be used as a reference for the wave and current experiments. In this case only the profiles at the center of the flume were measured when the angle $\theta = 0^o$ and 45^o and they are summarized in Table 2.2.

The N velocity profiles of a given component of the flow measured in each experiment were used to calculate the *spatial average velocity profile* of that component as follows:

$$u = \frac{0.5\ (u_0 + u_{N_{max}-1}) + \sum_{m=1}^{N-1} u_m}{N} \tag{2.1}$$

where u_m is the velocity component measured at a distance x_m from the ripple crest located at $x = 0$ (Figure 2-3), u_0 is the component of the velocity measured over the crest located at $x = 0$, and, $u_{N_{max}-1}$ is the component of the velocity measured over the crest located at $x = \lambda_x$.

2.2.2 Wave Experiments

The energy dissipation due to bottom friction experienced by pure waves and waves in presence of a current was estimated in terms of an energy friction factor. For this purpose, the free surface was measured at 33 locations along the flume at 0.5 m intervals using a set of conductivity wave gauges. A description of these wave gauges and the procedure followed for their calibration can be found in Mathisen (1993). The free surface was sampled at 19 hz for approximately 100 sec. These records were used to obtain the amplitude and phase of the wave as a function of x, the downstream distance measured from the wavemaker. From this information the incident and reflected wave components as well as the energy friction factor were obtained as in Mathisen and Madsen (1996). Pure wave energy attenuation experiments were performed for the same ripple configurations as for the pure current experiments: θ = 0^o, 30^o, 45^o and 60^o, without beads and with beads. Velocity profiles were also

PC	Beads	θ	y/b	N	x_m/Δ_x
	No	0	1/2	11	0 to 10
	No	45	1/2	3	0, 8, 14
	Yes	45	1/2	3	0, 8, 14
PW	Beads	θ	y/b	N	x_m/Δ_x
	No	45	1/2	8	0, 2, 4, 6, 8, 10, 12, 14
	Yes	45	1/2	8	0, 2, 4, 6, 8, 10, 12, 14
WC	Beads	θ	y/b	N	x_m/Δ_x
	No	0	1/2	11	0 to 10
	No	45	1/2	3	0, 8, 14
	No	45	1/2	3	0, 8, 14

Table 2.2: Summary of the experiments performed WITHOUT FILTER. PC: Pure Current experiments. PW: Pure Wave velocity profile measurements. WC:Wave and Current velocity profile measurements. N = the total number of profiles measured between two crests. x_m = the distance from the first crest where the velocity profile was measured. $\Delta_x = 1$ and 1.05 cm for $\theta = 0^o$ and 45^o, respectively.

measured for pure waves and for waves and current, without beads and with beads covering the bottom of the flume, but only for case of $\theta = 45^o$ at the center of the flume. These experiments are summarized in Table 2.1.

In the pure wave experiments the spatial average profile of the first harmonic wave amplitude and phase of the component of the flow in the $\hat{x}$ and $\hat{y}$ - directions were obtained using Eq. 2.1.

2.3 Velocity Measurements

2.3.1 Acoustic Doppler Velocimeter

Velocity profiles of the three-components of the flow were obtained using the Acoustic Doppler Velocimeter from Sontek Inc. In this section a brief description of the ADV system is presented. The details of this velocimeter and its properties can be found in Kraus, Lohrman and Cabrera (1994), Anderson and Lohrman (1994).

The ADV system consists of three modules: an acoustic sensor, a signal conditioning module, and a processing board installed in a 486 AT-compatible computer

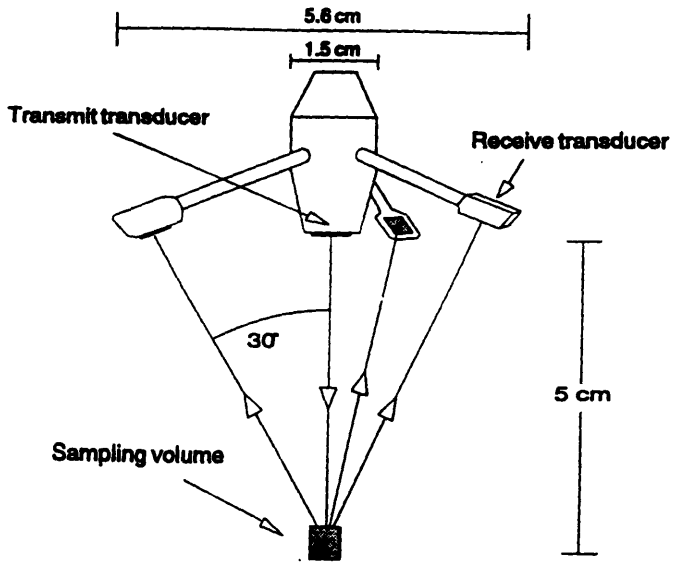

Figure 2-4: Acoustic sensor from Kraus *et.al* (1994).

used for data aquisition. The ADV sensor is shown in Figure 2-4. It consists of four ultrasonic transducers. The three receiver transducers are positioned in 120^o increments on a circle around the transmitter transducer. The transducers are located and oriented such that their acoustic beams all intercept at a common volume located at about 5 cm in front of the transmitter transducer. This volume is defined as the sampling volume. The sampling volume is approximately a cylinder of 6 mm diameter and 3.6 mm height and is oriented with its axis parallel to the transmitter axis.

The system operates by transmitting periodic acoustic pulses of 10-MHz. The pulses propagate through the water and are scattered by the suspended particles in the flow. The three receivers only detect the scattered signals originating from the sampling volume. The signal is then amplified in the conditioning module and sent to the processing board. In this module the signal is digitized and analyzed for frequency. The frequency is Doppler shifted according to the relative velocity of the flow with respect to the probe and is translated to a velocity measurement. In order to have a good measurement of the velocity the scattered signal must be strong enough to be clearly distinguishable from the random noise. The strength of the scattered signal is determined by the concentration and the size of the suspended particulates in the

water and is quantified in terms of a Signal to Noise Ratio expressed in dB. To obtain a good signal it was necessary to seed the water of the flume by adding the seeding material provided by Sontek Inc. This material consists of spherical particles of about 10 μm diameter that have a density close to that of the water. Another parameter to take into account is the correlation of the signal. In the present experiments a good signal was obtained when the Sound to Noise Ratio was $\approx$ 15 dB and the correlation was between 80% and 90%. The ADV also provides the information on the distance between the center of the sampling volume and the flume bottom. For the purpose of the roughness determination from the velocity profiles it is important to have a precise measurement of the location of the sampling volume. A check of the distance measured by the ADV was performed. It was found that the accuracy of the distance measured by the ADV was of the order of 0.1 cm, which corresponds to the error specified by Sontek Inc.

2.3.2 Pure Current Velocity Measurements

The three components of the velocity at a given position were obtained using the time-average of the time series measured with the ADV. Preliminary experiments were performed to determine the appropriate averaging length of the time series that produced an acceptable variability of the velocity measurements. The flow velocity was sampled for 40 min at a fixed elevation. The total record was then divided in sub-time series of shorter length and the corresponding time-average velocity was evaluated and compared with the time-average velocity of the original record of 40 minutes. This process was repeated at three different elevations above the bottom: 1 cm, 6 cm and 36 cm. It was found that a 200 sec record was sufficient to obtain the velocity measurements for the pure current experiments when the filter was installed. The corresponding standard deviation obtained from this study for the U - component of the velocity was 0.5 cm/sec, for the V - component 0.2 cm/sec, and for the W - component 0.1 cm/sec. The number of samples used in the measurements was 1600, resulting in a sampling frequency of 8 hz.

For the experiments with no filter the sampling time needed to ensure a stable

average was longer. When the angle $\theta = 0^o$ the standard deviation for the U - component was 0.5 cm/sec for a time series of length of 20 min. The sampling time for the no filter experiments was reduced when the angle $\theta = 45^o$. In this case the sampling time used was 400 sec in order to have the same standard deviation obtained in the experiments with filter. To operate the ADV it is neccesary to specify the Velocity Range. To avoid uncertainties in the velocity it is recommended to set the velocity range as the minimum value that covers the range of velocities expected in a given experiment. In the pure current experiments the Velocity Range was set to be $\pm$ 30 cm/sec. When measuring the velocity close to the bottom it was found in some cases that the velocity was biased towards zero. This problem was evident when the measuring volume was placed over the slope of the ripples. Between the ripples the bottom is plane and it was possible to obtain reliable measurements up to 0.3 cm to 0.4 cm above the bottom.

2.3.3 Wave Velocity Measurements

Velocity profiles for pure waves and for waves and current were measured when the ripples were placed at 45^o with respect to the incident wave. The Fast Fourier Transform algorithm was applied to the time series to obtain the first harmonic amplitude and phase of the velocity. The average velocity was obtained from the time-average of the time series. The phase information was obtained using the output voltage signal of the wavemaker transducer as the reference. The wavemaker signal was connected to a DAS-50 A/D converter board installed in the sampling computer that was synchronized with the ADV measurements. Preliminary experiments were carried out to obtain the appropriate sampling length and sampling frequency for these experiments. The sampling frequency used was 19 hz. For the pure wave experiments the velocity was sampled for 216 sec and the corresponding number of periods was 82. For the waves and current experiments the sampling time used was 430 sec in order to obtain a time average-velocity with the same standard deviation as the one present in the pure current experiments. The total number of periods in this case was 164. The estimated standard deviation for the first harmonic amplitude of the U - component

of the velocity was 0.2 cm/sec and for the V and W - components of the velocity was 0.1 cm/sec. Analysis of the time series close to the bottom showed that the signal exhibited drop-outs. To avoid this problem it was necessary to use a velocity range of $\pm$ 100 cm/sec when the measuring volume was placed at distances less than 4 cm above the bottom. For higher elevations the velocity range used was $\pm$ 30 cm/sec.

2.4 Alignment Procedures

Preliminary experiments were performed with ripples placed perpendicular to the incident current ($\theta = 0^o$). The purpose of these experiments were two-fold. First, to verify if the flow was fully developed at the test section, and second, to verify the uniformity of the flow generated by the current system. These experiments were performed without the filter installed.

Measurements of the velocity throughout the cross section of the flume were done at different downstream locations. The results of the experiments showed that the flow was fully developed at the test section located 11 m from the wavemaker.

In Figure 2-5 a) the time average of the $\hat{x}$ - component of the velocity averaged over 20 min records is presented. The measurements were done at the test section at $y = b/4, b/2$ and $3b/4$. The results show the flow is not uniform. Close to the bottom, at $z = 7$ cm, the velocity varies from approximately 15 cm/sec at $y = b/4$ to 11 cm/sec at $y = 3b/4$.

This problem was corrected by installing the filter described earlier. Measurements of the cross sections were repeated at the test section and are shown in Figure 2-5 b). The minimum distance above the bottom at which the velocity was measured was $z = 3$ cm. It can be seen in the figure that the presence of the filter corrects the nonuniformity of the flow. In addition the sampling time was reduced from 20 min to 200 sec. Therefore, all the pure current experiments were performed with the filter installed.

When the flow is incident at an angle with respect to the ripple axis, a three-dimensional flow is expected. The purpose of the experiments is to measure the

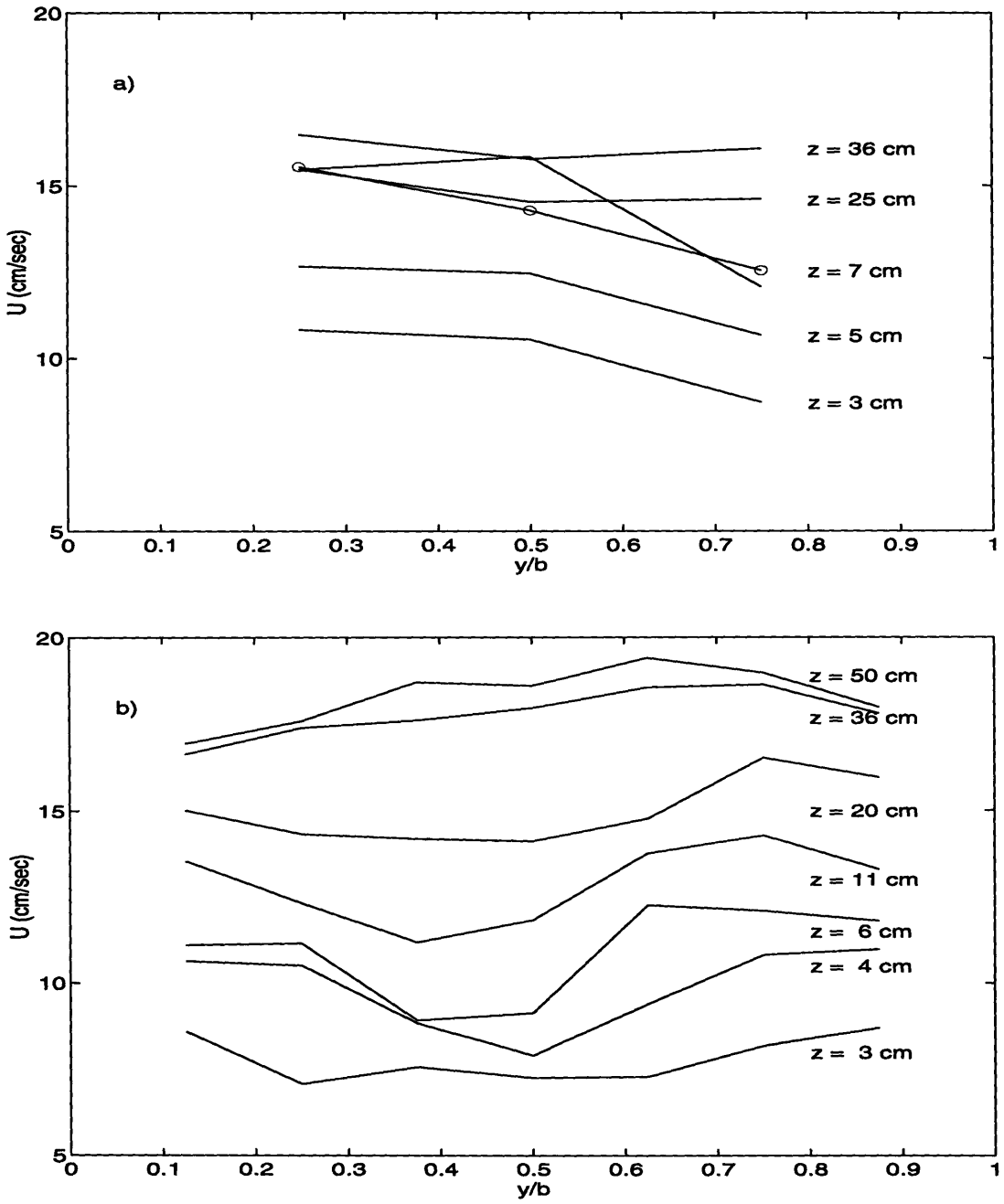

Figure 2-5: Cross Section Measurements at $x = 11$ m: U - component of the velocity as a function of y. a) Measurements without the filter. b) Measurements with the filter

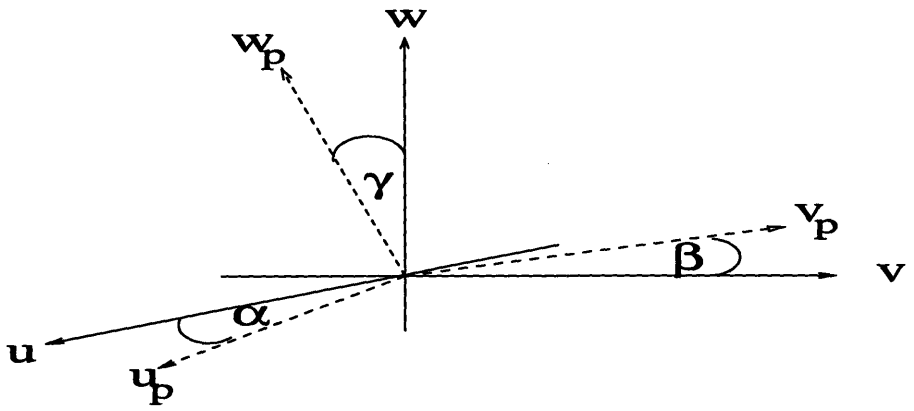

Figure 2-6: Definition of the rotation between the probe axis (u_p, v_p, w_p) and the physical axis (u, v, w).

characteristics of this flow. A bad alignment of the axis of the acoustic probe with respect to the physical axis can yield an incorrect interpretation of the measurements. Let (u_p, v_p, w_p) be the velocity measured by the probe and (u, v, w) the real velocity of the flow as indicated in Figure 2-6. The real velocity and the measured velocity are related by a rotation defined by the angles (α, β, γ). As an expample, we consider the simple case when the probe is rotated an angle α with respect to the physical z-axis, *i.e.*, $\beta = \gamma = 0$. The measured values (u_p, v_p) will be affected by the (u,v) components of the real flow, in particular: $v_p = u \sin\alpha + v \cos\alpha$. If the v - component is negligible with respect to the main flow, a small rotation of the angle will produce a measurement of $v_p \approx u \sin\alpha$. For $\alpha = 3^o$ and $u_p = 18$ cm/sec one obtains $v_p \approx 1$ cm/sec.

As an illustration, we consider the measurements of the (V, W) - components of the flow measured at the test section when the current is incident perpendicular to the ripple axis. This vector plot is shown in Figure 2-7 a). The vertical axis is the height measured above the bottom divided by the flow depth $h = 60$ cm. The U - component of the flow is pointing out from the plane of the Figure. The results show a secondary flow of the order of 1 cm/sec close to the free surface and directed from left to right, indicating a net flow going towards the right wall of the flume. This result is not realistic.

But if the measured value of the velocity is rotated an angle $(\alpha, \beta, \gamma) = (3^o, 0^o, 0.2^o)$, the resulting vector plot in Figure 2-7 a) is transformed into the vector plot in Figure 2-7 b). The angles of rotation (α, β, γ) were chosen as those that transformed the measured velocity at $z = 50$ cm and $y = b/2$ to be equal to zero. The transformed vector plot shows an organized flow pattern of 2 counter rotating cells in the lower half of the flow. Close to the bottom at $z = 3$ cm the flow moves from the side walls towards the center and the maximum magnitude of the velocity at that level is ≈ 0.8 cm/sec.

The secondary flow in Figure 2-7 b) is not unexpected, and is consistent with the minimum of the U component of the velocity observed in Figure 2-5 b). This secondary flow could originate from the unbalanced Reynolds stresses in the region of the flow close to the boundaries, (Townsend (1956), Einstein and Li (1958), Tracy (1965)). Another possible cause of the secondary flow could be the difference in roughness. These types of secondary flow have been studied in their relation to the formation of sand ribbons in shallow water (McLean, 1981). It is reasonable to expect the existence of a secondary flow in the present experiments, either from the unbalanced traverse Reynolds stresses close to the corners of the flume or due to the difference in roughness between the bottom and the smooth walls or a combination of both.

From this result it is concluded that a small rotation of the x_p probe axis affects the results while measuring small components of the velocity. The experiments performed when the ripples were placed at an angle with respect to the incident flow will be described in the next chapter. It was observed that the resulting V - component of the flow was of the order of the U - component at elevations close to the bottom. A poor probe orientation will not have a large effect on these measurements. But far from the bottom the V - component is small compared to the U - component so the possibility of a misalignment of the probe must be considered. To take this problem into account the measured velocity profiles were corrected by angle. The angles α, β and γ were selected in such a way that the depth average velocity of the V - component of the flow measured at $y = b/2$ after the rotation was equal to zero.

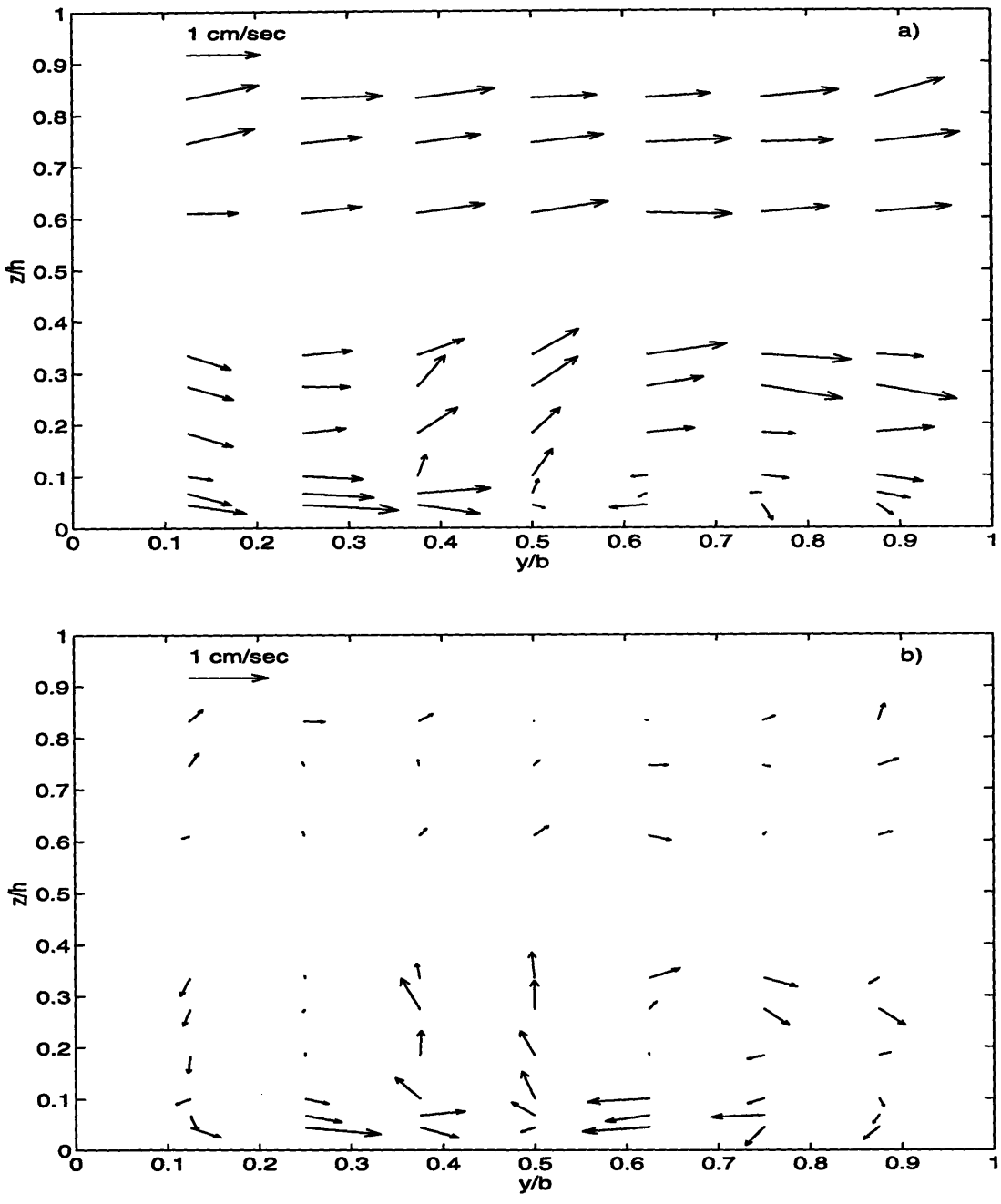

Figure 2-7: Vector plot of the (V, W) components of the flow measured at $x = 11$ m: a) Before angle correction b) After angle correction.

Chapter 3

Experiments

In this chapter the experiments performed when the ripples were placed at an angle $\theta = 0^o$, 30^0, 45^o and 60^o with respect to the incident flow are presented . The angle θ is defined in Figure 3-1 as the angle between the ripple axis and the $\hat{y}$ - direction. The wave experiments are described in section 3.1, and the pure current experiments are described and analyzed in the section 3.2.

The bottom resistance experienced by the flow is expressed in terms of a drag force which is the result of the pressure difference at the front and at the back of the ripples and is directed normal to the ripple axis. The drag force is assumed to be proportional to the ripple height, a drag coefficient and the square of a reference velocity. When the flow is incident at an angle to the ripple axis it is not clear if the drag coefficient is independent of the angle nor it is clear which reference velocity is appropriate to use in the expression for the drag force. The analysis of the experimental results presented in this chapter suggests that the drag coefficient is constant if the reference velocity used to express the drag force is the component of the velocity perpendicular to the ripple axis.

Another characteristic of the flow is revealed in the measurements presented in this chapter. Because of its nature the drag force is directed normally to the ripple axis. As shown in Figure 3-1 the drag force, $\vec{F_d}$, has two components. The component of the drag force in the $\hat{x}$ - direction represents the resistance force experienced by the incident flow and can be expressed in terms of a bottom roughness. The bottom

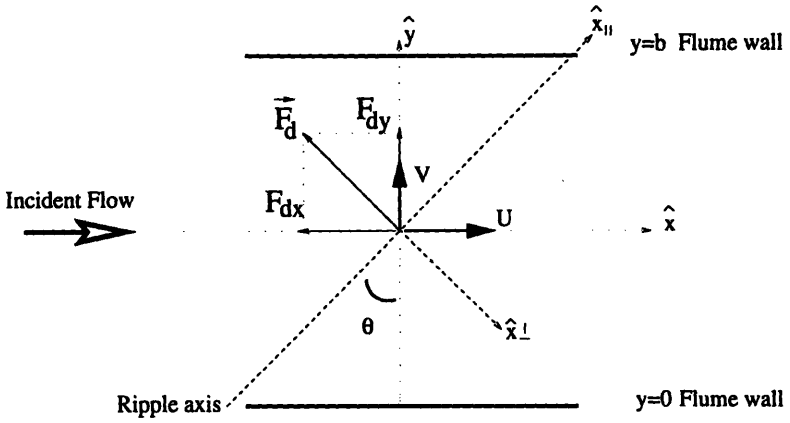

Figure 3-1: Definition of the Reference System

roughness is observed to be smaller the larger the angle of incidence.

In addition, the component of the drag force in the $\hat{y}$ - direction is unbalanced and induces the flow near the bottom to be turned towards to the ripple axis.

3.1 Pure Wave Experiments

3.1.1 Velocity Measurements

The description of the velocity measurements performed when second order Stokes waves were generated are presented in this section. The velocity profiles were obtained when the ripples were placed at an angle of 45^o with respect to the incident wave, which is in the $\hat{x}$ - direction as shown in Figure 3-1. The generated waves had a period of T = 2.63 sec and an amplitude of $\approx$ 6 cm. The water depth used in these experiments was h= 60 cm.

The measurements of the velocity in the pure wave experiments were made only when $\theta = 45^o$. These measurements were repeated for the case when the bottom of the flume was covered with the beads. In this section the experiments without the beads are described. The experiments with beads are presented in Appendix A. The velocity profiles were obtained by moving the traverse system along the $\hat{x}$ - axis, at steps of $\approx$ 2 cm between two crests. The amplitude of the first harmonic

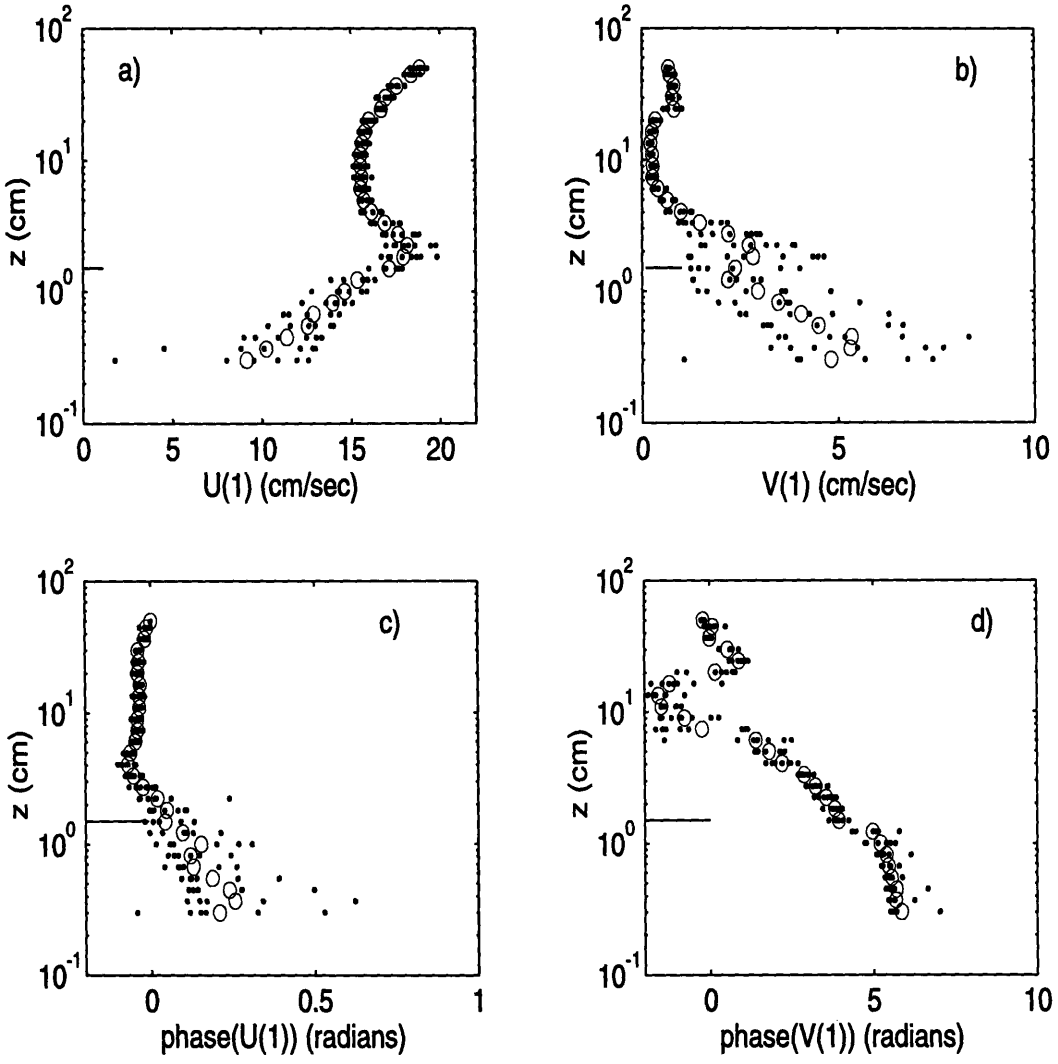

Figure 3-2: First harmonic of the wave amplitude and phase measured for the case of $\theta = 45^o$ in the experiments without beads. a) $U_{(1)}$ is the amplitude of the component of the velocity in the $\hat{x}$ - direction. b) $V_{(1)}$ is the amplitude of the component of the velocity in the $\hat{y}$ - direction. c) phase of the velocity component in the $\hat{x}$ - direction. d) phase of the velocity component in the $\hat{y}$ - direction.

obtained from the time series of the velocity measurements are shown in Figure 3-2 (a) and (b). In this figure $U_{(1)}$ and $V_{(1)}$ denote the first harmonic amplitude of the wave velocity in the $(\hat{x}, \hat{y})$ - directions. The phase of the first harmonic of the wave velocity components in the $\hat{x}$ and $\hat{y}$ directions are shown in Figure 3-2 (c) and (d), respectively. Both phases are plotted relative to the phase of the measurement of the $\hat{x}$ - component of the velocity obtained at the highest elevation, $z = 50$ cm, above the bottom of the flume. The 9 profiles measured in the experiments, represented by the dots in the figure, were used to obtain the spatial average profile (as explained in Chapter 2) represented by the circles. The small horizontal solid line corresponds to the top of the roughness elements.

Far from the bottom the wave orbital velocity amplitude $U_{(1)}$ can be described by potential wave theory. At a hight between 4 to 6 cm there is a large gradient in the wave velocity indicating the presence of turbulent shear stresses. The profile of the phase of the wave velocity in the $\hat{x}$ - direction starts to deviate from potential theory as well at that elevation. From these results the wave boundary layer thickness is $\delta_{wc} \approx 4$ to 6 cm. Inside the wave boundary layer the phase velocity first increases as z decreases. The wave amplitude reaches a maximum at $z \approx 2$ cm and then it decreases close to the bottom. The general behavior observed in the amplitude and phase of the wave velocity qualitatively agrees with the predictions of turbulent wave-boundary layer models (Grant and Madsen, 1986, Davies *et. al.*, 1988). Analogous profiles of the first harmonic wave amplitude have been obtained in the experiments performed by Mathisen and Madsen (1996) using similar wave conditions . In their experiments the artificial bottom roughness elements were the same as those used in the present experiments but the ripples were placed perpendicularly to the incident waves.

In the measurements described in Figure 3-2 the ripple axis is oriented at an angle of 45^o with respect to the incident wave. As in the case of the pure current experiments, a near-bottom flow in the $\hat{y}$ - direction is observed. The amplitude of this wave velocity component is shown in Figure 3-2 (b). It can be seen that the amplitude of the $\hat{y}$ component of the velocity is ≈ 5 cm/sec at the lower height

measured, $z = 0.3$ cm. It presents a maximum at $z \approx 0.5$ cm, decreases with distance above the bottom, and becomes ≈ 0 for $z > 6$ cm. At a height of ≈ 20 cm there is slight increase in the $\hat{y}$ - component of the wave velocity, indicating that there is some oscillation of the flow in the $\hat{y}$ - direction. The origin of this transverse oscillation is not clear. One possible explanation could be a bad orientation of the probe. It must be noted that the profiles presented in the Figure 3-2 were not corrected by angle. Far from the bottom the first harmonic wave amplitude $U_{(1)}$ is much larger than the $V_{(1)}$ component. In this region a small angle between the probe axis, x_p, and the $\hat{x}$ - direction can affect the measurements of $V_{(1)}$ as explained in Chapter 2. At $z \approx 20$ cm, $U(1)$ increases from 16 cm/sec to 16.7 cm/sec, whereas $V(1)$ increases from 0.3 cm/sec to 0.8 cm/sec, indicating that $U(1)$ is approximately constant but $V(1)$ increases by a factor of ≈ 2.5. As the probe was not repositioned during the experiment, this increased on the observed value of $V(1)$ at $z \approx 20$ cm cannot be explained by an incorrect orientation of the probe axis.

The profile of the phase of the wave component of the velocity in the $\hat{y}$ - direction in Figure 3-2 (d) has a maximum at the bottom of $\approx 335^o$. At this location the phase difference between the $U_{(1)}$ and $V_{(1)}$ components is $\approx 320^o$, indicating that they are approximately in phase. In this region the amplitude of the wave velocity $V_{(1)}$ is large, therefore an incorrect orientation of the probe will not have a big effect on the measured value of this component of the flow. The phase difference between the two components of the velocity can be explained through the drag force being responsible for the generation of the V component of the flow. As illustrated schematically in Figure 3-3, when the component of the flow velocity in the $\hat{x}$ - direction increases in time, the magnitude of the drag force, $\vec{F_d}$, increases and so does its component in the $\hat{y}$ - direction, producing the V component of the flow to increase.

The first harmonic wave amplitude and phase of the vertical component of the flow W are shown in Figure 3-4. The phase profile is plotted relative to the of the U - component of the wave velocity obtained at $z = 50$ cm. Similar to what was observed for the U -component, both the amplitude and phase of the W - component can be represented by potential theory for elevations above 6 cm, that is, outside the wave

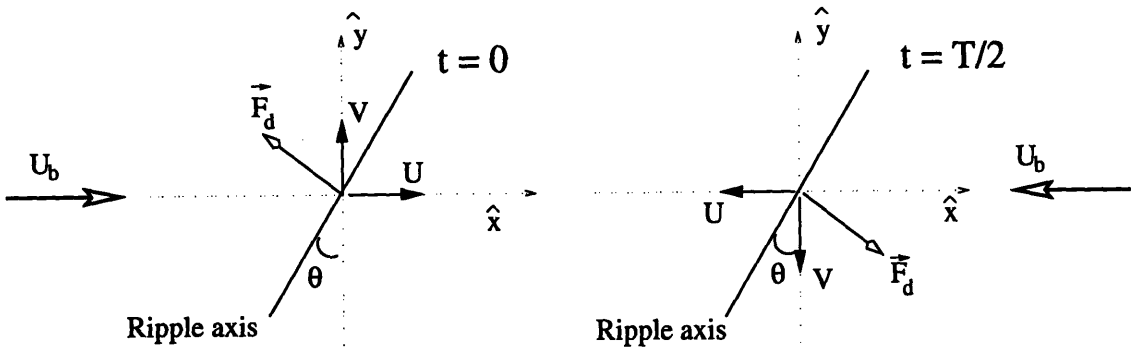

Figure 3-3: Schematic representation of the near-bottom flow in the pure wave experiments, where u_b is the maximum near-bottom wave orbital velocity

boundary layer. The wave amplitude decreases with height and the phase remains constant for $z > 6$ cm.

Using the measurements of the first harmonic amplitude and phase of the velocity components in the $(\hat{x}, \hat{y})$ direction, it is possible to construct the amplitude and the phase profiles of the wave velocity components in the $(\hat{x}_\perp, \hat{x}_\parallel)$ - directions by using the transformation:

$$\begin{aligned} U_\perp &= U\cos\theta - V\sin\theta \\ U_\parallel &= U\sin\theta + V\cos\theta \end{aligned} \tag{3.1}$$

These profiles are presented in Figure 3-5. The amplitude and the phase of the wave component in the direction perpendicular to the ripple axis in Figure 3-5 (a) and (c), respectively, present similar characteristics to those observed in the U - component of the velocity. For distances above $\approx$ 4 to 6 cm the profiles can be described by the potential theory solution. Inside the wave boundary layer the phase decreases with height and the amplitude of the velocity presents the overshoot at $z \approx 2$ cm, similar to but stronger than the one observed in the $U_{(1)}$ component profile. In constrast, the amplitude and phase of the component of the velocity in the direction parallel to the ripple axis do not present any significant change in their profiles at $z \approx 6$ cm. The

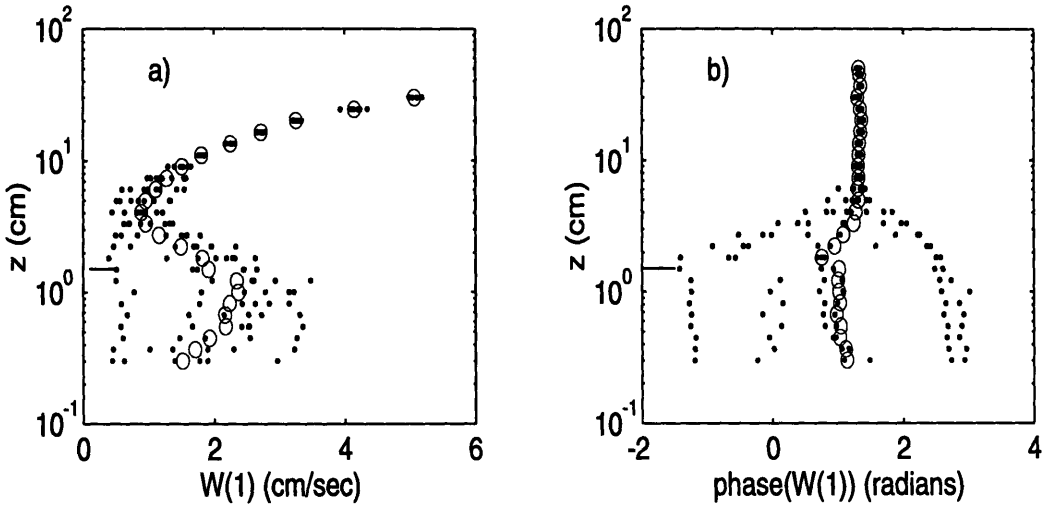

Figure 3-4: First harmonic wave amplitude and phase of the component of the wave velocity in the $\hat{z}$ direction obtained for $\theta = 45^o$ in the experiments without the beads

wave amplitude remains approximately constant throughout the region between $z \approx$ 1.5 to 20 cm with only a very small overshoot in the wave amplitude at a heigh of $z \approx 1.5$ cm.

There is a remarkable difference in the profiles of the wave amplitude and phase of the components of the flow in the direction perpendicular and parallel to the ripple axis. In the direction perpendicular to the ripple axis, a large wave boundary layer thickness indicates larger turbulence intensities, therefore larger bottom roughness. On the other hand, the flow in the direction parallel to the ripple axis presents a thinner wave boundary layer indicating that the bottom roughness experienced by the flow in this direction is smaller than the one experienced by the component of the flow in the direction perpendicular to the ripple axis.

3.1.2 Wave Energy Attenuation Experiments

The energy dissipation of the generated waves was measured when the ripples were placed at $\theta = 0^o, 30^o, 45^o$ and 60^o with respect to the direction of the incident wave.

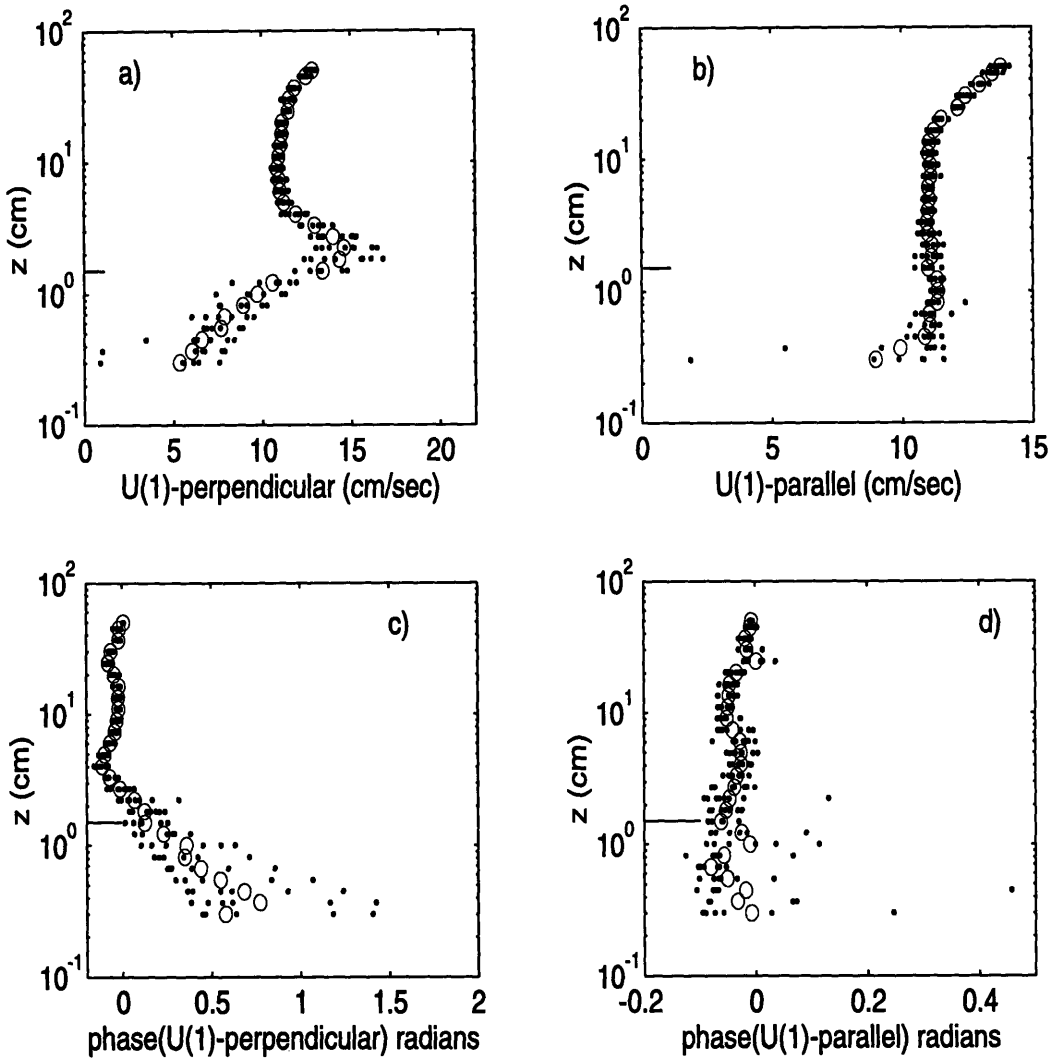

Figure 3-5: First harmonic amplitude and phase for the case of $\theta = 45^o$ in the experiments without beads. a) $U_{(1)\perp}$ the amplitude of the component of the velocity in the $\hat{x}_\perp$ - direction. b) $U_{(1)\|}$ the amplitude of the component of the velocity in the $\hat{x}_\|$ - direction. c) phase of the velocity component in the $\hat{x}_\perp$ - direction. d) phase of the velocity component in the $\hat{x}_\|$ - direction.

The energy dissipation can be expressed in terms of an energy friction factor, f_e. The details of the procedure followed to obtain the energy friction factor can be found in Mathisen and Madsen (1996). The free surface was measured at 33 locations along the flume at 0.5 m intervals. The measured first harmonic wave amplitude is expressed as:

$$|\zeta| \approx a_i(x) + a_r \cos(2kx + \beta) \tag{3.2}$$

where x is the position along the $\hat{x}$ - axis measured from the wavemaker, a_i and a_r are the amplitudes of the incident and the reflected waves, respectively, β is the phase difference between the incident and reflected wave , and, k is the wave number. The amplitude of the incident wave is assumed to decay linearly with respect to x:

$$a_i = A + B\,x \tag{3.3}$$

where A corresponds to the amplitude of the incident wave at the wavemaker and B is the wave attenuation slope. To obtain the energy friction factor, f_e, the representative wave amplitude was assumed to be the amplitude of the incident wave a_i evaluated at the mid-point between the first and the last location of measurement: $x_o \approx 10$ m measured from the wave-maker. The results of the experiments are summarized in Table 3.1. The values of the f_e listed in the table were obtained after accounting for sidewalls dissipation. The listed value $u_b \approx 17$ cm/sec corresponds to the near-bottom orbital velocity predicted by potential theory based on $a_i(x_o)$. The main source of error involved in the estimation of f_e, is given by the variability in the wave attenuation slope: B. The attenuation experiments were repeated at least twice for each angle and the error estimate based on the variability of the parameter B is the one listed in the Table 3.1. The relative error of the f_e estimates varies from approximately 10% to 30% when the angle θ increases from 0^o to 60^o. From the results shown in Table 3.1 , it is clear that the energy friction factor is a function of the angle between the wave direction and the ripple axis. To uncover the dependency of the energy friction factor on the angle of incidence a simple analysis is presented.

Assuming that the skin friction can be neglected, the energy dissipation inside the

TABLE A) NO BEADS							
θ	A (cm)	$B.10^{-4}$	a_i (cm)	a_r (cm)	β (rad)	u_b (cm/sec)	f_e
0	5.14	-3.71	4.71	0.67	-5.77	17.05	0.25±0.03
30	5.18	-3.29	4.80	0.79	-5.77	17.34	0.21±0.03
45	5.16	-2.25	4.90	0.76	-5.67	17.64	0.13±0.03
60	5.20	-1.50	5.03	0.84	-5.70	18.03	0.07±0.02
TABLE B) BEADS							
θ	A (cm)	$B.10^{-4}$	a_i (cm)	a_r (cm)	β (rad)	u_b (cm/sec)	f_e
0	5.14	-2.90	4.81	0.71	-5.77	17.34	0.18±0.004
30	5.25	-2.55	4.95	0.82	-5.77	17.84	0.14±0.01
45	5.18	-1.85	4.97	0.76	-5.67	17.85	0.09±0.01
60	5.24	-1.45	5.07	0.84	-5.70	18.19	0.06±0.01

Table 3.1: Pure Wave attenuation experiments. A) Experiments without beads. B) Experiments with beads.

wave boundary layer is only due to drag. Following the approach of Kajiura (1968), the energy dissipation E_d per unit area, averaged over a wave period is given by:

$$E_d = \overline{\vec{\tau_w} \cdot \vec{U_b}} \tag{3.4}$$

where the overbar represents the time average, $\vec{\tau}_w$ is the bottom shear stress and $\vec{U}_b = \vec{u}_b \cos \omega t$ is the velocity at the edge of the wave boundary layer $z = \delta_w$.

The energy dissipation can be expressed in terms of the energy friction factor:

$$E_d = \frac{\rho}{4} f_e \, u_b^3 \tag{3.5}$$

As shown in Figure 3-2, the first harmonic amplitude of the wave velocity in the $\hat{y}$ - direction has a maximum value at the bottom and decreases with height. At the elevation of $z = \delta_w$ the amplitude of the $V_{(1)}$ - component is negligible. Although velocity measurements were not performed for other angles than $\theta = 45^o$, it is reasonable to expect the effect of the bottom to be negligible at the edge of the wave boundary layer. Therefore, the V - component of the flow can be neglected. Under

this assumption, the near-bottom orbital velocity can be considered to be in the $\hat{x}$ - direction: $\vec{U}_b = u_b \cos \omega t \, \hat{x}$ and the scalar product in Eq. (3.4) involves only the $\hat{x}$ - component of the bottom shear stress: τ_{wx}. The bottom resistance experienced by the flow is represented by τ_{wx} and can be expressed in terms of the drag force:

$$\tau_{wx} = \frac{F_{dx}}{\lambda} \tag{3.6}$$

where λ is the distance between two ripple crests, (measured in the $\hat{x}_\perp$ - direction), and the subscript x indicates the projection of the drag force in the $\hat{x}$ - direction given by: $F_{dx} = F_d \cos \theta$. The drag force is assumed to have the following time dependency:

$$\vec{F}_d = \frac{\rho}{2} C_d \, \eta \, U_{r\perp} \, |U_{r\perp}| \, \hat{x}_\perp \tag{3.7}$$

where C_d is the drag coefficient, η is the ripple height, which for the experiments without beads is $\eta = 1.5$ cm and for the experiments with beads is $\eta = 1.5$ cm - $d = 0.9$ cm, and $U_{r\perp}$ is the reference velocity that depends on time. The reference velocity in Eq (3.7) is assumed to be given by the perpendicular component of the flow velocity at the edge of the wave boundary layer:

$$U_{r\perp} = u_b \cos\omega t \cos \theta \tag{3.8}$$

Replacing Eqs. (3.8) to (3.5) into (3.4) the result obtained after taking the time average is:

$$\frac{f_e \, u_b^3}{4} = \frac{4}{3\pi} \frac{1}{2} C_d \frac{\eta}{\lambda} u_b^3 \cos^3 \theta \tag{3.9}$$

Eq. (3.9) suggests that f_e is proportional to $\cos^3 \theta$ if the value of the drag coefficient C_d is independent of θ, and if the proper choice of the reference velocity is the velocity component in the direction perpendicular to the ripple axis.

The values of f_e in Table 3.1 were fitted by the least square method vs $\cos^3 \theta$ according to:

$$f_e = m \cos^3 \theta + b \tag{3.10}$$

A) f_e	R	m	b	C_d
No Beads	0.9823	0.21±0.03	0.05±0.02	1.65±0.22
Beads	0.9945	0.14±0.01	0.05±0.01	1.77±0.13
B) f_{ed}	R	m	b	C_d
No Beads	0.9826	0.22±0.03	0.04±0.02	1.72±0.23
Beads	0.9940	0.16±0.01	0.02±0.01	2.09±0.16

Table 3.2: Fitting parameters according to Eq. (3.10). A) f_e vs θ B) f_{ed} vs θ obtained by the second approach described in text.

The resulting parameters obtained in the fitting, the correlation coefficient, R , the slope, m, and the intercept, b, are presented in Table 3.2 (A). The drag coefficient listed in the last column of the table was obtained from Eq (3.9) and (3.10) as a function of the estimated slope, m, as:

$$C_d = \frac{3\pi}{8}\frac{\lambda}{\eta} m \tag{3.11}$$

The error of C_d listed in the last column of the table was estimated based on the standard deviation of the slope m obtained by fitting Eq. (3.10) with the least square method.

The analysis presented is based on the assumption that the energy dissipation is due only to drag. This approximation is not necessarily true. In the case of the experiments with beads the contribution of the energy dissipation due to skin friction could be important. To take into account the skin friction term in the evaluation of the total energy dissipation it is assumed, that

$$E_d = \overline{\vec{\tau_w} \cdot \vec{U_b}} + \frac{\lambda'}{\lambda}\overline{\vec{\tau_w'} \cdot \vec{U_b'}} \tag{3.12}$$

The first term of the equation corresponds to the energy dissipation due to drag and is expressed as a function of the drag force as done before to obtain Eq. (3.9). The second term is the energy dissipation due to skin friction, where $\vec{U_b'}$ is now the flow velocity at $z = \delta_w'$, the thickness of the wave boundary layer due to skin friction. In

principle, δ'_w is unknown, and is assumed to be proportional to $\delta'_w \approx \kappa\, u'_{*w}/\omega$, where u'_{*w} is the skin shear velocity defined based on the skin friction bottom shear stress as: $u'_{*w} = \sqrt{\tau'_w/\rho}$. The factor multiplying the skin friction term, λ'/λ, takes into account the fact that when there is a layer of beads between the ripples, the effective distance over which the skin friction bottom shear stress acts is $\lambda' = \lambda - 2\eta$. The skin friction bottom shear stress can be expressed in terms of an energy friction factor due to skin friction, f'_e, as:

$$\overline{\vec{\tau}'_w \vec{U}'_b} = \frac{\rho}{4} f'_e u'^3_b \tag{3.13}$$

Using Eqs. (3.13) and (3.12), the total energy friction factor is written as:

$$f_e u_b^3 = f_{ed} u_b^3 + \frac{\lambda'}{\lambda} f'_e u'^3_b \tag{3.14}$$

where, f_{ed}, the energy friction factor due to drag is introduced to represent the drag term contribution to the total energy dissipation. From Eq. (3.14) the energy friction factor due to drag is expressed as a function of the total energy friction factor obtained in the wave attenuation experiments and the energy friction factor due to skin friction:

$$f_{ed} = f_e - \frac{\lambda'}{\lambda} f'_e \left(\frac{u'_b}{u_b}\right)^3 \tag{3.15}$$

The problem now is to evaluate the skin friction factor, f'_e, and u'_b. Two ways of estimating f'_e are considered.

The first approach is to assume that the flow close to the bottom is described by the model proposed by Grant and Madsen (1986). This model is applied in the following way:

i) Using the measured values of f_e and the near-bottom orbital velocity u_b as input parameters to the model, the wave velocity, $u_w(z)$, inside the wave boundary layer is obtained.

ii) Assuming a given value of δ'_w smaller than δ_w, an estimate of u'_b is obtained by evaluating the velocity predicted in i) at z = δ'_w: $u'_b = u_w(\delta'_w)$.

iii) The model is applied again using as input the value of u'_b obtained in ii) and the

bottom roughness given by $z'_o = d/30$ under the assumption of rough turbulent flow. In this way the shear velocity $u'_{*w} = \sqrt{f'_w/2}\, u'_b$ is determined, and therefore a new estimate of $\delta'_w = 2\,\kappa\, u'_{*w}/\omega$ is obtained.

The process is repeated until the assumed value of δ'_w in i) agrees with the value obtained in iii). Following this procedure, the value of the energy friction factor due to skin friction obtained for the experiments with beads is listed on the third column of Table 3.3 (B) under the heading f'_e(I).

The second approach to obtain f'_e is to assume that u'_b is given by the wave velocity obtained in i) at the ripple crest: $u'_b = u_w(z = \eta)$. Then, the Grant-Madsen model is solved by specifying u'_b and the roughness $z'_o = d/30$. The resulting values of f'_e obtained by using this approach are listed in the fourth column of Table 3.3 (B) under the heading f'_e(II).

This method was also applied to the experiments without the beads. In this case, the Grant-Madsen model is solved by specifying $u'_b = u_w(\eta)$ and the bottom roughness, which without beads is given by $z'_o = \nu/(9\, u'_{*w})$ assuming the flow is smooth turbulent. The estimates of f'_e for the experiments without beads are listed in the Table 3.3 (A).

Having the values of u'_b and f'_e Eq. (3.15) is used to evaluate the energy dissipation due to drag. The corresponding results of f_{ed} for each of the experiments are listed in the last column of Table 3.3.

The error in the estimates of f_{ed} is mainly related to the variability of the total energy friction factor, f_e (listed in the second column of Table 3.3). The results presented in Table 3.3 show that the two proposed methods of estimating f_{ed} give virtually identical results result. Comparing the listed values of f_e and f_{ed}, the contribution of the skin friction to the total energy dissipation is negligible, except for the case of the experiments with beads when $\theta = 60^o$.

The listed values of f_{ed} obtained by using the second approach were fitted vs $\cos^3\theta$. Using Eq. (3.11) the value of the drag coefficient was obtained and are shown in the last column of Table 3.2 (B). For the case of the experiments without beads $C_d = 1.72 \pm 0.23$, and for the experiments with beads $C_d = 2.09 \pm 0.16$. The error of

TABLE A) NO BEADS					
θ	f_e		f'_e(II)		f_{ed}(II)
0	0.25±0.03		0.013		0.24± 0.03
30	0.21±0.03		0.013		0.20± 0.02
45	0.13±0.03		0.011		0.12± 0.03
60	0.07±0.02		0.011		0.06± 0.02
TABLE B) BEADS					
θ	f_e	f'_e(I)	f'_e(II)	f_{ed}(I)	f_{ed}(II)
0	0.18±0.004	0.044	0.055	0.17 ±0.004	0.17 ±0.005
30	0.14±0.010	0.043	0.049	0.14 ± 0.01	0.13 ± 0.01
45	0.09±0.010	0.043	0.045	0.09 ± 0.02	0.07 ± 0.02
60	0.06±0.010	0.043	0.043	0.04 ± 0.01	0.03 ± 0.01

Table 3.3: Energy friction factor due to drag f_{ed} vs θ. A) Experiments with no beads: f'_e is obtained using the second method explained in the text. B) Experiments with beads: f'_e is obtained by using the two methods explained in the text. (I) indicates the first method, and (II) the second method.

C_d was estimated based on the standard deviation of the slope m obtained by fitting of Eq. (3.10) with the least square method.

The fitting parameters obtained are listed in Table 3.2 (B) and the resulting curve is shown in the Figure 3-6. The intercept b corresponds to the limiting case of ripples parallel to the direction of wave propagation ($\theta = 90^o$), therefore, it is expected $b = 0$. After accounting for skin friction, the values of b (Table 3.2 (B)) are slightly smaller than the values of b obtained by fitting the total energy friction factor f_e vs. $\cos^3\theta$ (Table 3.2 (A)). The resulting slope obtained based on the fitting of f_{ed} is bigger than the one obtained based on the fitting of f_e. This result is reflected in the values of C_d obtained by using Eq. (3.11). Although the values of the correlation coefficient is not very heigh, the fitted line in Figure 3-6 lies inside the range of the estimated error of the measurements.

It is concluded that the energy friction factor due to drag $f_{ed} \propto \cos^3\theta$. This result was obtained by assuming that the drag force is scaled by the square of the reference velocity in the perpendicular direction, $U_{r\perp}$.

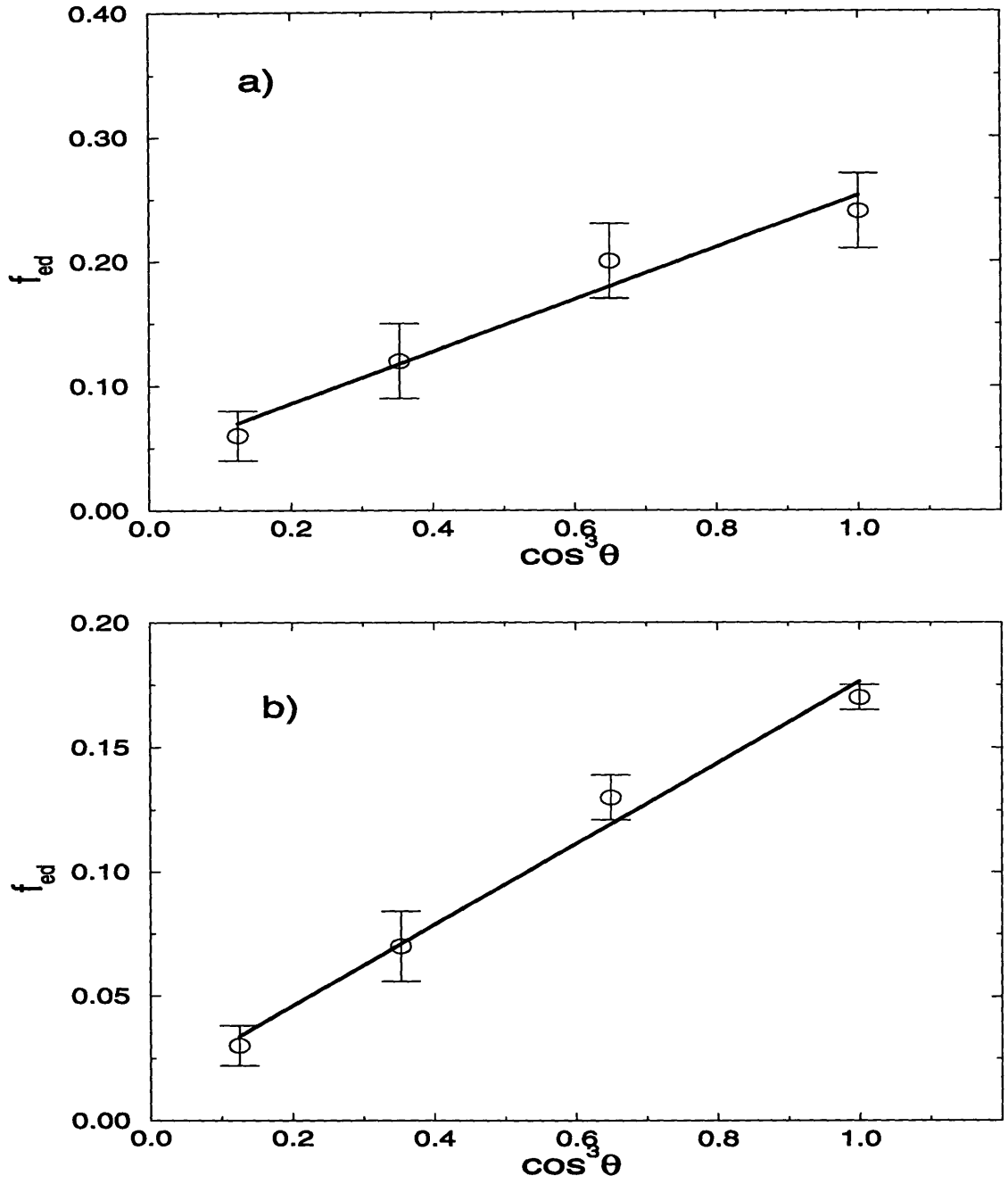

Figure 3-6: Fitting of f_{ed} vs $\cos^3\theta$. a) Experiments with no beads b) Experiments with beads. The fitting parameters are listed in Table 3.2 B)

3.2 Pure Current Experiments

3.2.1 Description of the measurements

In this section the main characteristics of the flow observed in the measurements performed when the current is incident at an angle with respect to the ripple axis are described based on the experiments made for the case of $\theta = 45^o$ without beads. The rest of the experiments performed are presented in Appendix A. All the pure current profiles were corrected by angle using the criterion explained in Chapter 2.

In Figure 3-7 a vector plot of the (V, W) components of the flow measured for the case when the ripples were placed at an angle $\theta = 45^o$ with respect to the incident current is shown. The horizontal axis in the vector plot is the distance measured along the $\hat{y}$ - direction divided by the flume width: $b = 76$ cm. The vertical axis is the distance above the bottom normalized by the water depth $h = 60$ cm. The incident current is in the $\hat{x}$ - direction pointing out of the figure.

The figure shows that at the lower height measured: $z = 3$ cm above the bottom, the V - component of the velocity is approximately uniform at the center region of the flume with a magnitude of $\approx$ 2.2 cm/sec. Close to the free surface, at $z = 54$ cm, V = -1.5 cm/sec at the center region.

Because of the physical limitation of the traverse system it was not possible to measure the flow very close to the walls of the flume. But there is evidence based on flow visualization of suspended particles in the water that the flow close to the left wall, $y/b = 0$, is directed downwards and the flow close to the right wall, $y/b = 1$, is directed upwards implying that the flow can be approximately described as one cell rotating anti-clockwise.

As mentioned in Chapter 2, the velocity profiles were obtained by moving the traverse system along the $\hat{x}$ - axis at steps of $\approx$ 1 cm between the two crests. The vector plot of the (U, W) - components of the flow measured at the center of the flume, $y/b = 1/2$, for $\theta = 45^o$ is presented in Figure 3-8 (a). Only the velocity vectors close to the bottom, $z < 4$ cm, are shown. The horizontal axis is in the $\hat{x}$ - direction, *i.e.*, the direction of the incident current. The first profile was measured above the

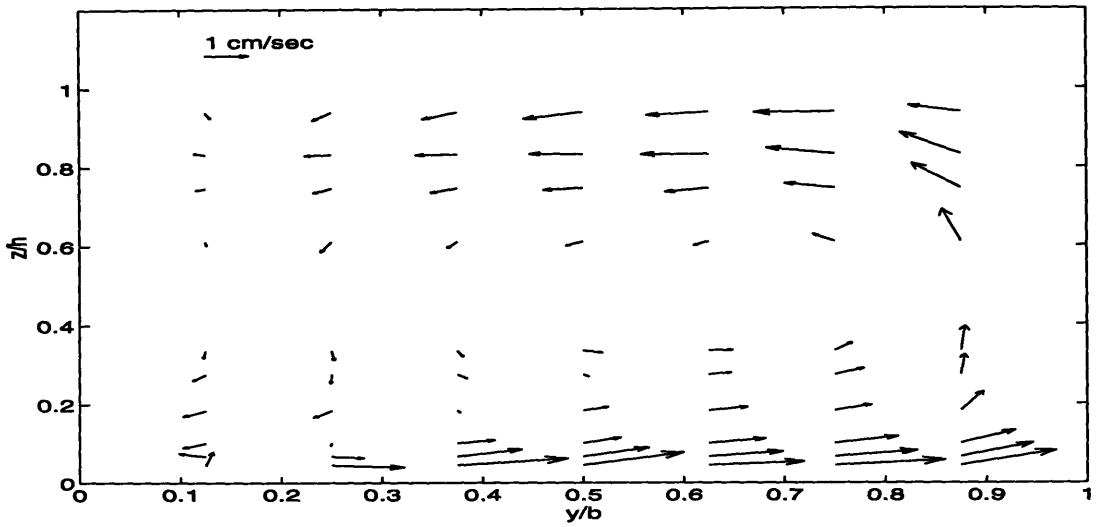

Figure 3-7: Vector plot of the (V, W) velocity components measured for $\theta = 45^o$ for the NO BEADS experiments

crest located at $x = 0$ cm and the last profile was measured at $x = 10/\cos 45^o = 14.14$ cm. The effect of the ripples on the flow is represented by the undulations seen in the flow pattern. There is no evidence of flow separation at the ripple crest located at $x = 0$ cm. The profile measured at $x \approx 12$ cm was included in the vector plot for completeness. It can be seen that the velocity at this location is approximately 0. Analysis of the corresponding time series obtained showed that the signal acquired with the ADV was influenced by reflections coming from the upstream side of the ripple. Therefore, these points were not considered in the calculation of the spatial average velocity profile. In Figure 3-8 (b) the velocity measurements close to the bottom made when the flow was incident perpendicularly to the ripple axis, $\theta = 0^o$, are shown in a vector plot of the (U, W)-components. The horizontal axis is in the $\hat{x}$ - direction, which is the direction of the incident flow. In contrast to Figure 3-8 (a), the flow presents a well defined recirculation region downstream of the ripple located at $x = 0$ cm. The flow separates at the crest and reattaches at a distance $x \approx 5$ cm. The two experiments presented in Figure 3-8 (a) and (b) were performed using the same flow conditions, i.e, a water depth of $h = 60$ cm and the same depth-averaged

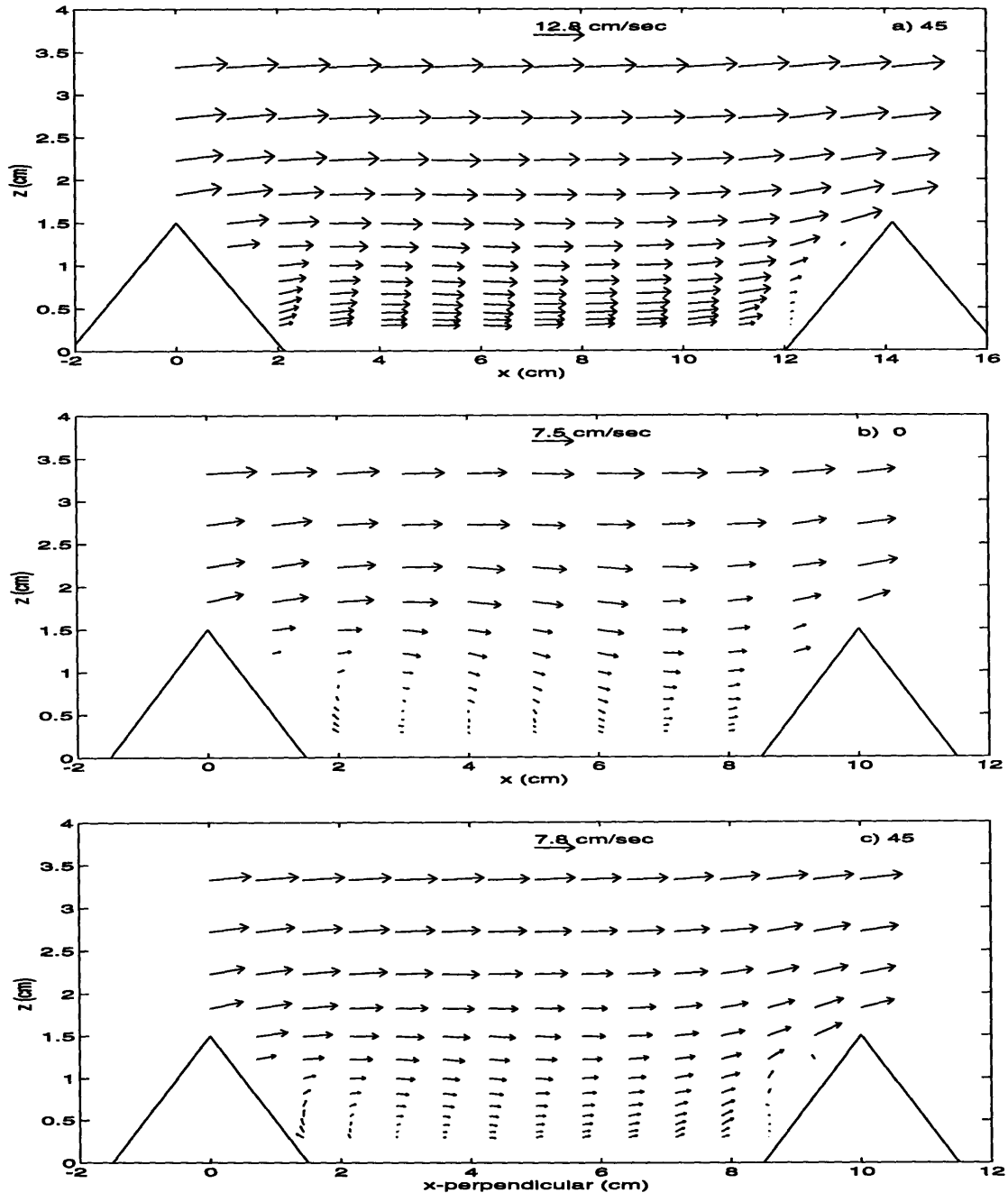

Figure 3-8: Detailed Velocity Field between two ripple crests in the NO BEADS Experiments: a) Vector plot of the (U, W) velocity components measured for $\theta = 45^o$, b) Vector plot of the (U, W) velocity components measured for $\theta = 0^o$, c) Vector plot of the $(U_\perp, W)$ velocity components measured for $\theta = 45^o$.

velocity of $\approx$ 17 cm/sec. The only difference between them is the angle between the incident current and the ripple axis.

In Figure 3-1 the direction perpendicular to the ripple axis is noted by $\hat{x}_\perp$ and the direction parallel to the ripple axis is noted by $\hat{x}_\parallel$. The velocity components (U, V) measured in the $(\hat{x}, \hat{y})$ - direction can be transformed into the component $(U_\perp, U_\parallel)$ in the $(\hat{x}_\perp, \hat{x}_\parallel)$ - direction using the transformation given by Eq. (3.19).

The vector plot of the $(U_\perp, W)$ components of the velocity for the experiments performed when $\theta = 45^o$, *i.e* corresponding to the results in Figure 3-8 (a), is presented in Figure 3-8 (c). The horizontal axis is the distance measured from the ripple crest in the $\hat{x}_\perp$ - direction (perpendicular to the ripple axis). This vector plot shows a flow pattern similar to the one presented in Figure 3-8 (b) for the measurements obtained when $\theta = 0^o$. The flow separates at the crest of the ripple located at $x_\perp = 0$ cm and it reattaches at a distance of approximately 4 cm from the ripple crest.

Similar flow characteristics were observed for the rest of the experiments performed when $\theta = 30^o, 60^o$, and when a monolayer of beads was placed over the bottom of the flume between the ripples. These experiments are presented in Appendix A. The flow pattern in the $\hat{x}$ - direction does not indicate the presence of a region of separation. In the direction perpendicular to the ripple axis, the flow separates at the crest of the ripples. It must be noted that for the case of the experiments when $\theta = 60^o$ and when the beads were present, the separation region was not as well defined as for the other cases.

For the particular case of $\theta = 45^o$, the perpendicular component of the velocity in the region close to the bottom has the same magnitude as the velocity measured for the case of $\theta = 0^o$. As indicated in the Figures 3-8 (b) and (c), the magnitude of the $U(\theta = 0^o)$ and $U_\perp(\theta = 45^o)$ velocity components at $z \approx 3$ cm is of approximately 7.5 cm/sec. This value is smaller than that observed in Figure 3-8 (a) for the component of the velocity in the $\hat{x}$ - direction, which is $U(\theta = 45^o) = 12.8$ cm/sec. A larger velocity in the $\hat{x}$ - direction indicates that the flow resistance experienced by the component of the flow in this direction, is smaller than the one experienced by the flow in the perpendicular direction. This conclusion is verified by the analysis of the

experiments presented below.

The spatial average profile of the velocity components were evaluated, as explained in Chapter 2, based on the velocity profiles obtained by moving the traverse along the $\hat{x}$ - direction between the two ripple crests. To study the dependence of the near-bottom flow on the angle θ, the spatial average velocity profiles of the U and V components of the flow are plotted in Figures 3-9 (a) and (b). These profiles correspond to the measurements made at the center of the flume, $y = b/2$, when ripples were placed at $\theta = 0^0$, 30^0, 45^0 and 60^0 without beads on the bottom of the flume. Also included in this figure are the velocity components perpendicular, $U_\perp$, and parallel, $U_\parallel$, to the ripple axis. The small horizontal solid line corresponds to the top of the roughness elements, *i.e.*, the ripple height $\eta = 1.5$ cm.

The spatial average profiles corresponding to the U - component of the velocity in Figure 3-9 (a) show that the flow close to the bottom is reduced when the angle θ is reduced from 60^o to 0^o. As was anticipated, this figure demonstrates the angle dependence of the bottom roughness in the direction of the incident current.

The spatial average velocity profiles corresponding to the V - component of the flow in Figure 3-9 b) has a value of approximately 3 to 5 cm/sec at the lower height measured: $z = 0.3$ cm. These values are of the same order as those measured in the pure wave experiment shown in Figure 3-2 (b). It must be noted that the observed values of the V - component of the flow are surprisingly large if they are compared with the corresponding values of the U - component of the velocity measured at the same height as seen from the results listed in Table 3.4. Further away from the bottom, the V - component decreases, is equal to zero at $z \approx 30$ cm , and reaches a minimum of approximately -1 cm/sec close to the free surface ($z = 50$ cm).

The spatial average profiles corresponding to the $U_\perp$ and the $U_\parallel$ components of the velocity are shown in Figure 3-9 (c) and (d), respectively. These figures show an important characteristic of the flow: the direction of the velocity vector depends on the height above the bottom. For a given angle θ and in the region close to the bottom, the V - component of the flow is of the same order than the U - component . Therefore, $U_\perp \approx 0$ and the velocity is almost directed parallel to the ripple axis. For higher

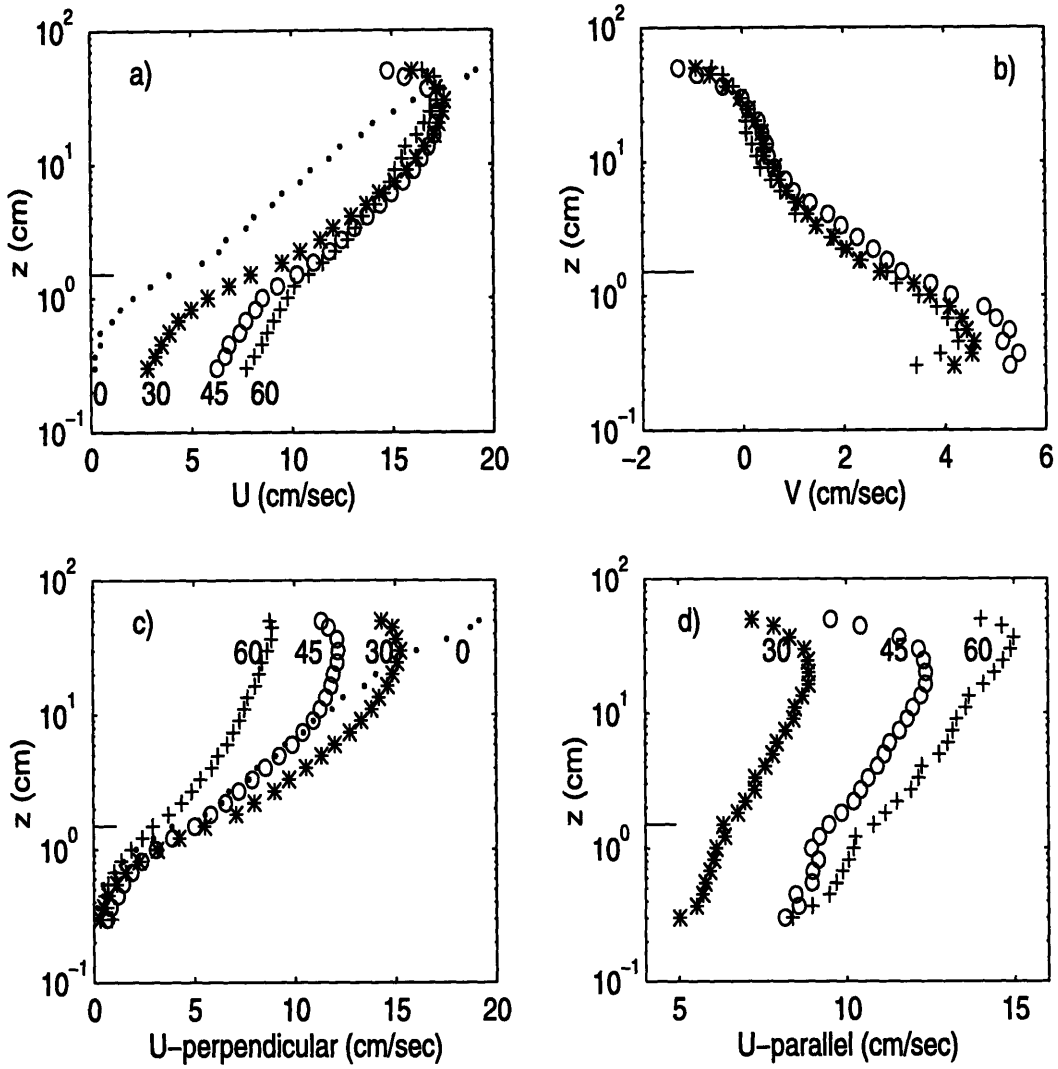

Figure 3-9: Spatial average velocity profiles of the NO BEADS experiments at the center of the flume, $y/b = 1/2$, as a function of the angle θ. a) U, b) V, c) $U_\perp$ and d) $U_\parallel$ - component. The symbols correspond to the different ripple configurations used: ... $\theta = 0^o$, * $\theta = 30^o$, o $\theta = 45^o$, + $\theta = 60^o$. The top of the roughness element is indicated by the horizontal solid line

NO BEADS	θ	U (cm/sec)	V (cm/sec)
	30^o	2.79	4.18
	45^o	6.24	5.29
	60^o	7.70	3.43
BEADS	θ	U (cm/sec)	V (cm/sec)
	30^o	3.34	2.78
	45^o	5.47	3.36
	60^o	5.83	2.10

Table 3.4: Velocity components in the $(\hat{x}, \hat{y})$ direction measured at $z = 0.3$ cm above the bottom at $y/b = 1/2$ in the pure current measurements

elevations, the $U_\perp$ - component becomes more important, and the velocity vector will start to rotate from being directed parallel to the ripple axis to being directed parallel to the incident flow at elevations where the V - component is negligible. It is observed in the figure, that the magnitude of the parallel and perpendicular components of the flow depends on the angle θ. By definition, $U_\perp \propto U \cos\theta$ and $U_\parallel \propto U \sin\theta$. The resulting effect is a decrease of $U_\perp$ and an increase of $U_\parallel$ when the angle θ increases.

In order to study the spatial dependence of the experimental results due to the finite width of the flume, the velocity measurements performed at the center of the flume, $y/b = 1/2$ were repeated at two other locations along the $\hat{y}$ - axis: $y/b = 3/8$ and $y/b = 5/8$.

In Figure 3-10 the spatial average profiles of the U, V, $U_\perp$ and $U_\parallel$ components of the velocity are presented for the case of $\theta = 45^o$. The different symbols correspond to the profiles measured at three different locations along the $\hat{y}$ - axis: $y = 3b/8, y = b/2$ and $y = 5b/8$. The profiles share the same characteristic: close to the bottom, for elevations below 4 cm, the velocity is virtually independent of the y - location. The spatial average velocity profile of U and $U_\perp$ obtained in the experiments without beads at $y = b/2$ and $\theta = 45^o$ are represented by the circles in Figure 3-11 (a) and (b), respectively. The figure show a well defined logarithmic region between $z = 1.5$ cm and $z = 6$ to 7 cm. The dotted line represents the logarithmic fitting obtained as explained in the next section.

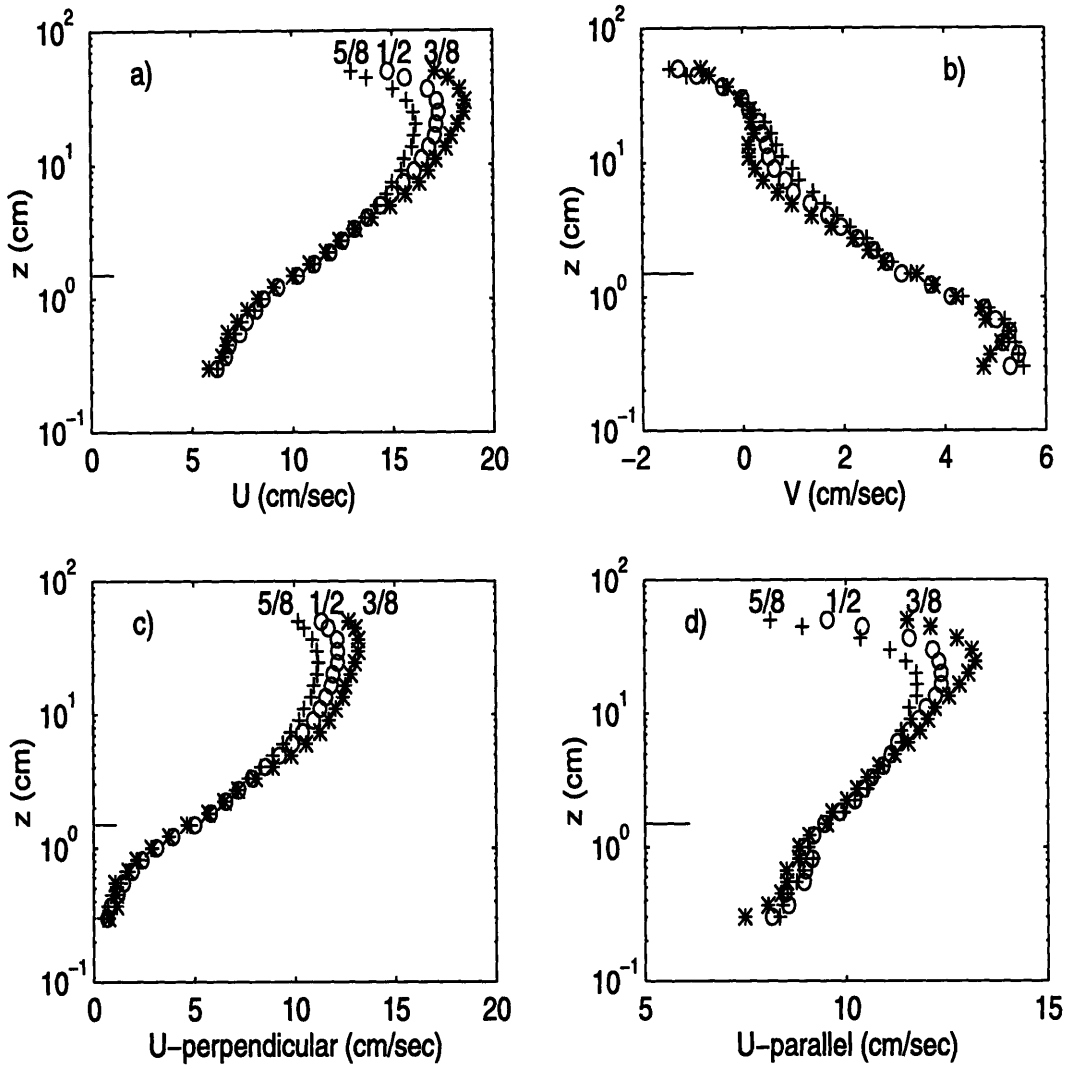

Figure 3-10: Spatial average velocity profiles of experiments as a function of y measured for $\theta = 45^o$ and NO BEADS. a) U, b) V, c) $U_\perp$ and d) $U_\parallel$ - component. The symbols correspond to + $y/b = 3/8$, o $y/b = 1/2$ and * $y/b = 5/8$. The top of the roughness element is indicated by the horizontal solid line.

For higher elevations the velocity profiles present a change in slope and at $z =$ 30 cm they exhibit a maximum and then they start to decrease. In the upper region of the flume the velocity depends on the y - location. Close to the right wall of the flume, $y = 5b/8$, the U-component of the velocity is smaller than the corresponding profile close to the left wall, $y = 3b/8$.

Since, the lower region of the flow is the one considered for the purpose of studying the mechanism of the generation of the lateral flow and for predicting the bottom resistance experienced by the flow, the behavior of the flow in the upper part of the water column is of minor importance.

3.2.2 Analysis of the Pure Current Velocity Profiles

Close to the bottom the spatial average velocity profiles present a well defined logarithmic region between 1.5 cm up to approximately 7 cm. Values of the shear velocity and bottom roughness obtained by fitting a logarithmic velocity profile in the region close to the bottom are listed in Table 3.5 (A) for the experiments without beads, and, in Table 3.5 (B) for the experiments with beads. The subscripts x and $\perp$ correspond to the $\hat{x}$ and $\hat{x}_\perp$ directions, respectively. The number of points used in the fitting was between 5 to 7. The theoretical level used for the experiments with no beads was the bottom of the flume and for the experiments with beads it was $0.35d$ below the top of the beads (Mathisen 1993, Jackson 1981), where $d = 0.64$ cm is the bead diameter.

The error of the shear velocity were estimated based on a 95% confidence level. Depending on the number of points used for the fitting and the value obtained for the correlation coefficient, R in Table 3.5, the resulting errors were of the order of 10% for u_{*x} and for $u_{*\perp}$. The corresponding errors obtained for the bottom roughness were of the order of 30% for z_{ox} and 20% for $z_{o\perp}$. The values of the shear velocity and bottom roughness obtained from the fitting of the parallel component of the velocity are not included in Table 3.5. The resulting correlation coefficients obtained for this component of the velocity were in general low and the error estimated for $z_{o\parallel} \pm 0.8 z_{o\parallel}$.

When the angle is changed from $\theta = 0^o$ to $\theta = 60^o$ the value of the roughness corresponding to the x-component of the velocity, z_{ox}, varies from 0.36 cm to 0.01 cm

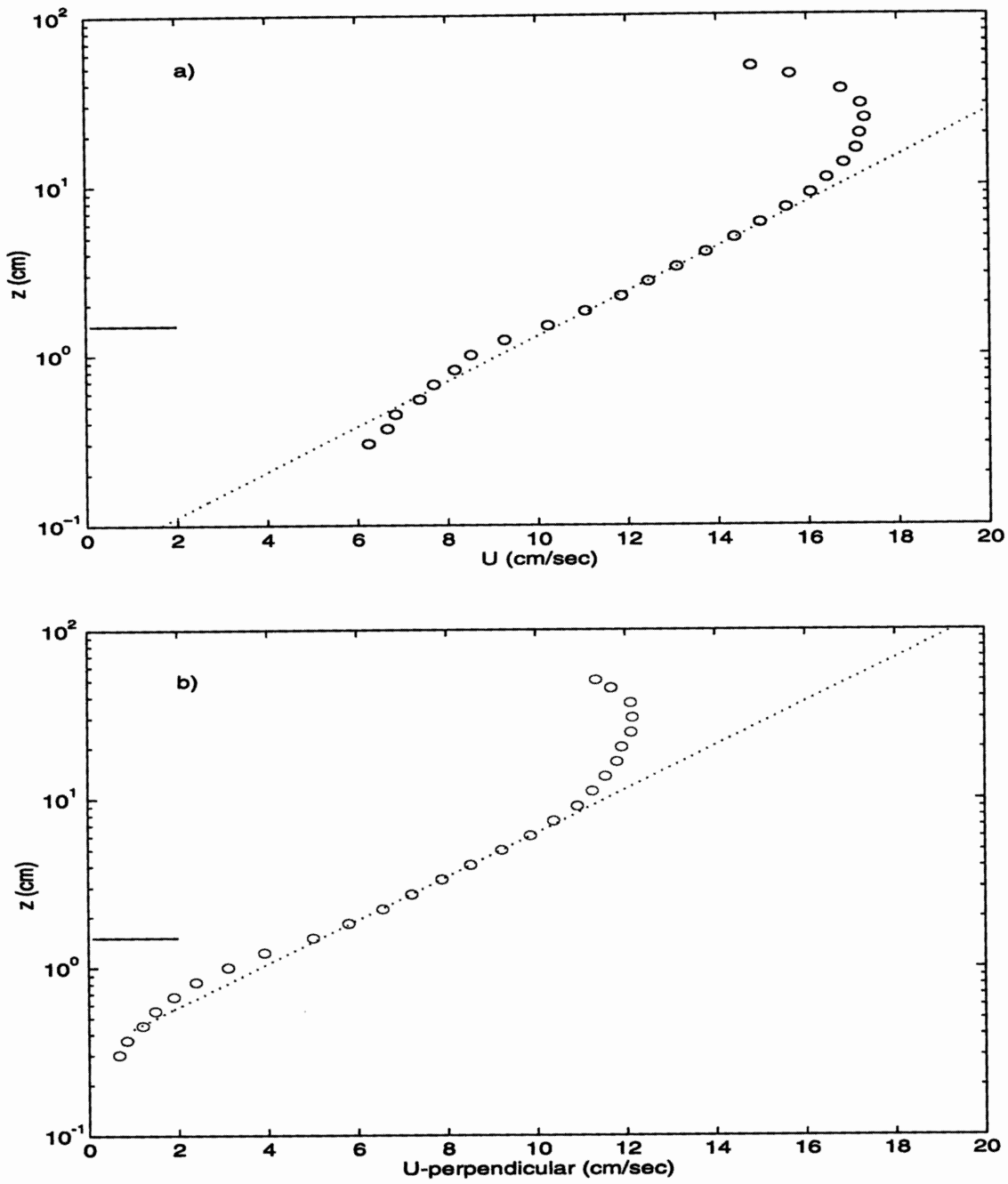

Figure 3-11: Logarithmic region of the spatial average velocity profile in the region $\eta < z < 7$ cm when $\theta = 45^o$, $y = b/2$ NO BEADS. o: experimental points. —:the logarithmic fitting. a) U: the velocity component in the $\hat{x}$ - direction, b) $U_\perp$ the velocity component in the $\hat{x}_\perp$ - direction

Table A) NO BEADS										
θ^o	y/b	R_x	u_{*x}	z_{ox}	$R_\perp$	$u_{*\perp}$	$z_{o\perp}$	u_{*d}	u'_*	C_d
0	1/2	0.9965	1.37	0.36	0.9965	1.37	0.36	1.33	0.35	0.76
30	3/8	0.9978	2.04	0.29	0.9991	2.07	0.48	2.02	0.58	1.12
30	1/2	0.9984	1.59	0.16	0.9989	1.70	0.34	1.63	0.57	0.71
30	5/8	0.9986	1.59	0.17	0.9993	1.63	0.34	1.56	0.57	0.68
45	3/8	0.9995	1.59	0.12	0.9994	1.62	0.45	1.56	0.64	1.00
45	1/2	0.9992	1.31	0.06	0.9998	1.35	0.32	1.26	0.65	0.63
45	5/8	0.9990	1.21	0.05	0.9992	1.22	0.27	1.13	0.66	0.52
60	3/8	0.9991	1.05	0.02	0.9999	1.09	0.43	1.02	0.69	0.90
60	1/2	0.9972	1.01	0.02	0.9967	0.96	0.37	0.88	0.67	0.76
60	5/8	0.9888	0.92	0.01	0.9967	0.84	0.28	0.74	0.69	0.48

Table B) BEADS										
θ^o	y/b	R_x	u_{*x}	z_{ox}	$R_\perp$	$u_{*\perp}$	$z_{o\perp}$	u_{*d}	u'_*	C_d
0	1/2	0.9977	1.11	0.17	0.9977	1.11	0.17	1.01	0.57	0.64
30	3/8	0.9974	1.48	0.12	0.9987	1.52	0.22	1.38	0.86	0.88
30	1/2	0.9987	1.42	0.12	0.9990	1.38	0.20	1.23	0.84	0.76
30	5/8	0.9943	1.28	0.10	0.9958	1.23	0.17	1.08	0.80	0.62
45	3/8	0.9995	1.31	0.08	0.9991	1.22	0.25	1.08	0.94	0.88
45	1/2	0.9981	1.19	0.06	0.9995	1.01	0.15	0.82	0.93	0.49
45	5/8	0.9998	1.16	0.05	0.9949	0.98	0.15	0.79	0.93	0.45
60	3/8	0.9959	1.08	0.03	0.9985	0.87	0.24	0.71	1.01	0.76
60	1/2	0.9980	1.03	0.03	0.9988	0.76	0.19	0.57	0.99	0.53
60	5/8	0.9985	0.90	0.02	0.9983	0.65	0.13	0.40	0.99	0.23

Table 3.5: Shear Velocities, Hydraulic Roughness and Drag Coefficients for the Pure Current Experiments: A) Experiments without beads B) Experiments with beads. The correlation coefficient, shear velocity in (cm/sec) and bottom roughness in (cm) obtained by fitting a logarithmic velocity profile to the spatial average velocity measured in the $\hat{x}$ - direction (indicated by the subscript x), and in the $\hat{x}_\perp$ - direction (indicated by the subscript $\perp$. The shear velocities u'_* (cm/sec) and u_{*d} (cm/sec) are obtained obtained according to Eqs. (3.19) and (3.24) respectively

for the experiments with no beads, and from 0.17 cm to 0.02 cm for the experiments with beads. In contrast, the values obtained for the roughness corresponding to the component of the velocity perpendicular to the ripple axis do not present a dependency on the angle. For the experiments with no beads, the resulting value of the perpendicular roughness obtained as the mean value of all the experiments is $z_{o\perp} = (0.36 \pm 0.07)$ cm and for the experiments with beads, $z_{o\perp} = (0.19 \pm 0.04)$ cm. The standard deviation represents a relative error of about 20% which is of the order of the accuracy estimated from the fittings. The smaller value of $z_{o\perp}$ obtained in the experiments with beads can be explained by the fact that the effective ripple height in these experiments is smaller than the ripple height in the experiments without the beads. In the experiments without beads $\eta = 1.5$ cm and the ratio $z_{o\perp}/\eta \approx 0.24$. In the experiments with beads the effective ripple height is $\eta = 1.5$ cm - $d = 0.9$ cm and the ratio $z_{o\perp}/\eta \approx 0.21$.

From the analysis of the spatial average velocity profiles presented above it is concluded that the bottom roughness experienced by the incident flow, z_{ox} depends on the angle θ. The roughness in the perpendicular direction: $z_{o\perp}$ can be considered to be independent of the angle and related to the ripple height with an approximate value of $z_{o\perp} \approx 0.23\eta$, yielding an equivalent Nikuradse bottom roughness of $k_b = 30\ z_{o\perp} \approx 7\eta$.

3.2.3 Determination of C_d.

The conclusion obtained from the analysis of the energy friction factor measured in the wave attenuation experiments was that the appropriate reference velocity to be used in the scaling of the drag force is the component of the velocity in the direction perpendicular to the ripple axis. This result is used in this section to estimate the drag coefficient from the measurements of the pure current velocity profiles.

The bottom resistance experienced by the flow consists of two contributions, the skin friction and the form drag caused by the ripples, (Smith and McLean, 1977). The bottom resistance related to the flow over two-dimensional roughness elements of height η and spacing λ is expressed in terms of a drag force $\vec{F}_d$ that is assumed to

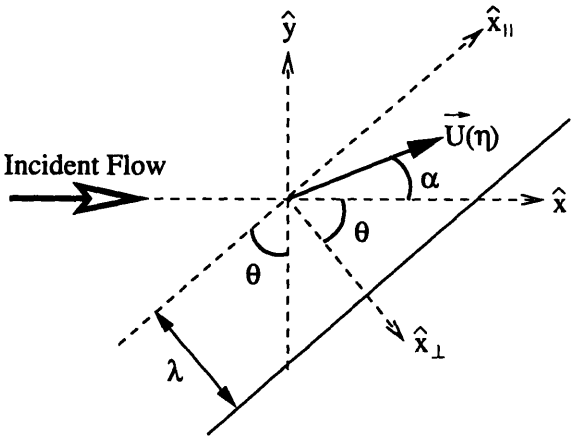

Figure 3-12: Schematic definition of the direction of the reference velocity $\vec{U}(z_r = \eta)$.

be given by:

$$\vec{F_d} = \frac{\rho}{2} C_d \, \eta \, U_{r\perp}^2 \, \hat{x}_\perp \tag{3.16}$$

where ρ is the fluid density and C_d is the drag coefficient. The reference velocity, $U_{r\perp}$, is assumed to be the flow velocity in the direction perpendicular to the ripple axis at the reference elevation $z_r = \eta$.

In this analysis the skin friction contribution is assumed to be the bed shear stress produced when the ripples are not present and is expressed in terms of a shear velocity u'_*:

$$\vec{\tau'} = \rho u_*^{'2} \hat{\alpha} \tag{3.17}$$

where $\hat{\alpha}$ defines the direction of the flow velocity at the reference elevation $z_r = \eta$, which is at an angle α with respect to the $\hat{x}$ - axis, as shown in Figure 3-12. The total flow resistance per unit length in the $x_\perp$ - direction is expressed as:

$$\lambda \tau_{b\perp} = F_d + \lambda' \tau'_\perp \tag{3.18}$$

where $\tau_{b\perp}$ is the total bottom shear stress in the perpendicular direction and λ' is the effective distance over which the skin friction acts. For the experiments with beads $\lambda' = \lambda - 2\,\eta$, and for the experiments without beads $\lambda' = \lambda$. Expressing the total bottom shear stress in the perpendicular direction in terms of a shear velocity $u_{*\perp}$,

and introducing Eqs. (3.16) and(3.17) into (3.18) :

$$\lambda\, u_{*\perp}^2 \;=\; \frac{1}{2}\, C_d\, \eta\, U_{r\perp}^2 \;+\; \lambda'\, u_*'^2\, cos(\theta+\alpha) \tag{3.19}$$

If the skin friction is assumed to be negligible with respect to the drag contribution, Eq. (3.19) becomes:

$$\lambda\, u_{*\perp}^2 \;=\; \frac{1}{2} C_d\, \eta\, U_{r\perp}^2 \tag{3.20}$$

Expressing the reference velocity in the perpendicular direction as:

$$U_{r\perp} \;=\; \frac{u_{*\perp}}{\kappa}\, \ln(\frac{\eta}{z_{o\perp}}) \tag{3.21}$$

an expression for the drag coefficient is obtained using Eq. (3.21) in Eq. (3.20):

$$C_d \;=\; \frac{2\lambda}{\eta}\, \frac{\kappa^2}{[\ln(\eta/z_{o\perp})]^2} \tag{3.22}$$

indicating that C_d depends on the ripple geometry, (λ, η) and on the roughness in the perpendicular direction ($z_{o\perp}$). The results obtained from the analysis of the spatial average velocity profiles in the perpendicular direction presented in Table 3.5 show that the bottom roughness $z_{o\perp}$ was independent of the angle. Therefore, a constant bottom roughness in the perpendicular direction is consistent with the assumption of a constant drag coefficient.

If the skin friction term is not negligible, Eq. (3.19) must be used to obtain the drag coefficient. In order to estimate the skin friction term it is assumed that the flow velocity at the reference elevation is known and that the flow is described by the law of the wall in the region between z_o', the bottom roughness due to skin friction, and $z_r = \eta$:

$$\vec{U}(z_r) = \frac{u_*'}{\kappa}\, \ln(\frac{z_r}{z_o'})\, \hat{\alpha} \tag{3.23}$$

The value of the bottom roughness due to skin friction is assumed to be given by $z_o' = \nu/9u_*'$ when the flow is smooth turbulent as expected for the experiments without beads. For the experiments with beads the flow is assumed to be rough

turbulent, therefore, $z'_o = d/30$.

Knowing the magnitude and direction of the flow velocity at η measured in the experiments, the value of u'_* can be obtained from Eq (3.23). With $u_{*\perp}$ estimated from the fittings the resulting values of C_d from Eq. (3.19) are listed in the last column of Table 3.5. For the experiments without beads $C_d = (0.8 \pm 0.2)$ and for the experiments with beads $C_d = (0.6 \pm 0.2)$. Within the uncertainty of the estimates the drag coefficient obtained in the experiments without beads is the same as the one obtained in the experiments with beads.

Having determined the value of C_d the drag term in Eq. (3.19) can be evaluated to obtain the shear velocity associated with the drag contribution to the total bottom shear stress as:

$$u^2_{*d} = \frac{1}{2} \frac{C_d \, \eta}{\lambda} U^2_{r\perp} \tag{3.24}$$

The values of the shear velocity corresponding to the skin friction shear velocity, u'_*, and the shear velocity associated with the drag contribution, u_{*d} are also listed in Table 3.5

The results show that the skin friction contribution becomes more important with respect to the drag contribution when θ increases from 0^o to 60^o. After evaluating the drag term it is obtained for the experiments with no beads that $u^2_d \approx u^2_{*\perp}$ for $\theta = 0^o$ and $u^2_{*d} \approx 0.8 \, u^2_{*\perp}$ for $\theta = 60^o$. For the experiments with beads $u^2_{*d} \approx 0.8 \, u^2_{*\perp}$ for $\theta = 0^o$ and $u^2_{*d} \approx 0.4 \, u^2_{*\perp}$ for $\theta = 60^o$.

The analysis of the experimental velocity profiles presented in this section indicates that the flow resistance experienced by a flow incident at an angle with respect to the ripple axis can be expressed in terms of a drag force. The drag coefficient obtained is independent of the angle of incidence and the drag force is scaled by the square of the reference velocity in the direction perpendicular to the ripple axis at the elevation of the ripple crest.

Chapter 4

Pure Current Model for Experimental Conditions

In Chapter 3 the experiments performed when the current is incident at an angle with respect to the ripple axis were described. The measurements showed that near the bottom the V - component of the velocity is of the same order than the U - component. In this chapter the concept of a drag force oriented perpendicular to the ripple axis is introduced in a simple model to described the observed near-bottom flow.

In Figure 4-1 the incident flow, u_o, is assumed to be in the $\hat{x}$ - direction. The angle between the ripple axis and the $\hat{y}$ - direction is θ. The bottom shear stress in the direction perpendicular to the ripple axis is balanced by the drag force. The component of the shear stress in the parallel direction to the ripple axis is initially unbalanced and is used to represent a driving force that will induce the fluid to move along the ripple axis.

Because the flume has a finite width the lateral flow does not have time to become fully developed. Therefore, the velocity consists on two components. One component is represented by the steady state, u_o, in the $\hat{x}$ - direction. The other component is the time-dependent velocity in the direction parallel to the ripple axis caused by the unbalanced component of the shear stress.

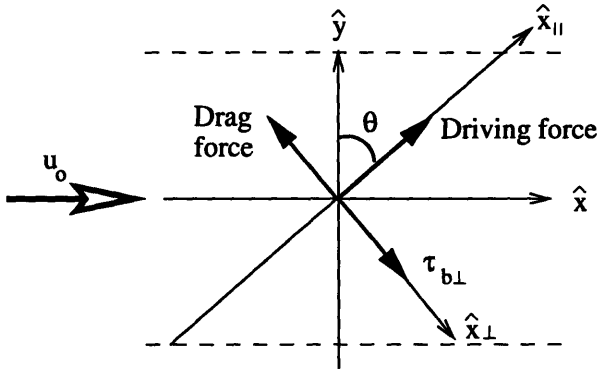

Figure 4-1: Definition of the Reference System The incident flow, u_o is in the $\hat{x}$ - direction. The perpendicular component of the bottom shear stress, $\tau_{ob\perp}$ is balanced with the Drag force. The Driving force is in the direction parallel to the ripple axis, $\hat{x}_{\|}$

4.1 Description of the model

The flow is assumed to be driven by a uniform pressure gradient. The pressure gradient is in the $\hat{x}$ - direction and is defined in terms of a shear velocity u_*:

$$-\frac{\partial p_o}{\partial x} = \rho \frac{u_*^2}{h} \tag{4.1}$$

where h is the water depth.

The flow is assumed to be uniform:

$$-\frac{\partial p_o}{\partial x} + \frac{\partial \tau_o}{\partial z} = 0 \tag{4.2}$$

where τ_o is the shear stress and is assumed to be:

$$\tau_o = \rho \nu_{ot} \frac{\partial u_o}{\partial z} \tag{4.3}$$

and, $\nu_{ot} = \kappa u_* z(1 - z/h)$ is the eddy viscosity. The flow is initially represented by

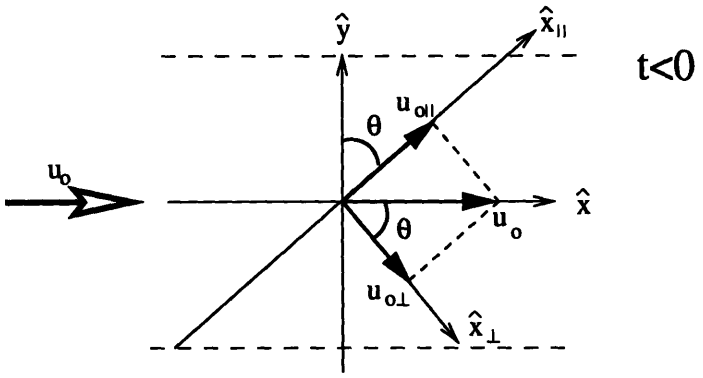

Figure 4-2: Sketch of initial conditions for model developement. For times $t < 0$ the flow is in equilibrium and is given by u_o. The component of the flow in the direction perpendicular to the ripple axis is: $u_{o\perp}$, and in the direction parallel to the ripple axis is $u_{o\parallel}$.

the usual logarithmic velocity profile:

$$u_o = \frac{u_*}{\kappa} \ln(\frac{z}{z_o}) \tag{4.4}$$

The shear stress at the bottom can be decomposed in a component perpendicular to the ripple axis, $\tau_{ob\perp}$, and in a component parallel to the ripple axis, $\tau_{ob\parallel}$. The perpendicular component is assumed to be balanced by the drag force. The parallel component is, in principle, unbalanced and is assumed to represent a driving force in the direction parallel to the ripple axis.

The time at which the driving force starts to act is defined as $t = 0$. For times $t < 0$, the flow is in equilibrium and can be written in the $(\hat{x}_\perp, \hat{x}_\parallel)$ axis, Figure 4-2:

$$u_o = u_{o\perp}\, \hat{x}_\perp + u_{o\parallel}\, \hat{x}_\parallel \tag{4.5}$$

Combining Eqs (4.4) and (4.5):

$$u_{o\perp} = \frac{u_*}{\kappa} \cos\theta \ln(\frac{z}{z_o}) \tag{4.6}$$

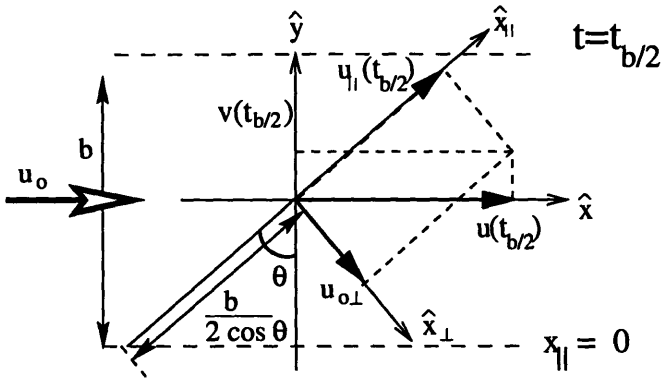

Figure 4-3: Sketch of transformation from time to space At time $t = t_{b/2}$ a fluid particle initially located at $x_{||} = 0$ reaches the center of the flume. The component of the velocity in the parallel direction to the ripple axis is $U_{||} = u_{o||} + u_{||}(t = t_{b/2})$

$$u_{o||} = \frac{u_*}{\kappa} \sin\theta \ln(\frac{z}{z_o}) \tag{4.7}$$

Let us consider a fluid particle placed at the side wall of the flume, $x_{||} = 0$. At $t = 0$ the driving force starts to act over the fluid particle, which is accelerated away from the wall in the direction parallel to the ripple axis. After a given time, $t = t_{b/2}$, the fluid particle originally located at $x_{||} = 0$ will be in the center of the flume. The velocity of the fluid particle at this location is is given by:

$$U_{\perp}(t_{b/2}) = u_{o\perp} \tag{4.8}$$

$$U_{||}(t_{b/2}) = u_{o||} + u_{||}(t_{b/2}) \tag{4.9}$$

where $u_{o||}$ is the time-independent part of $U_{||}$ given in Eq. (4.7), and $u_{||}(t_{b/2})$ is the time-dependent part of the velocity component in the parallel direction at $t = t_{b/2}$. As the forcing is assumed to be in the direction parallel to the ripple axis, the perpendicular component of the velocity in Eq. (4.8) remains constant in time and equal to $u_{o\perp}$ given by Eq. (4.6).

In this analysis the velocity of the flow at the center of the flume in Eqs. (4.8)

and (4.9) is expressed as a function of the time $t = t_{b/2}$. This time is defined as the time needed for the fluid particle that is initially located at $x_{\|} = 0$ to reach the center of the flume. The distance traveled by the particle between the side wall, $x_{\|} = 0$, and the center of the flume along the direction parallel to the ripple axis is shown in Figure 4-3, and is related to the time $t_{b/2}$ by:

$$\frac{b}{2\cos\theta} = \int_0^{t_{b/2}} u_{\|}(z=\eta,t)\, dt \tag{4.10}$$

where $u_{\|}(z=\eta,t)$ is the time dependent component of the velocity evaluated at the top of the ripple $z = \eta$.

The parallel component of the bottom shear stress given by:

$$\tau_{ob\|} = \rho\, u_*^2\, \sin\theta \tag{4.11}$$

is used to represent the driving force. This driving force is expressed as an effective pressure gradient acting over the fluid particles in the direction parallel to the ripple axis:

$$-\frac{\partial p_{driving}}{\partial x_{\|}} = \rho\, \frac{u_*^2}{h}\, \sin\,\theta\, f(z) \tag{4.12}$$

where $f(z)$ is the spatial distribution of the driving force which is assumed to be:

$$f(z) = \begin{cases} \frac{h}{\eta} & \text{for } z_o' < z < \eta \\ 0 & \text{for } \eta < z < h \end{cases} \tag{4.13}$$

where z_o' is the bottom roughness in the parallel direction and is given by the corresponding bottom roughness due to skin friction.

The driving force starts to act by accelerating the near-bottom flow. At the same time, the shear stress starts to increase and to compensate the effect of the driving force by diffusion of vorticity. The equation describing the time dependent parallel component of the velocity is written as:

$$\frac{\partial u_{\|}}{\partial t} = \frac{u_*^2}{h}\, \sin\theta\, f(z) + \frac{\partial \tau_{\|}/\rho}{\partial z} \tag{4.14}$$

where $\tau_{\|}$ is the shear stress representing the diffusion term and is expressed in terms of an eddy viscosity ν_t:

$$\tau_{\|}(z,t) \;=\; \rho\,\nu_t\,\frac{\partial u_{\|}(t)}{\partial z} \tag{4.15}$$

In Eq (4.14) the convective terms have been neglecting by assuming that the flume is wide compare to the water depth. To take into account the presence of the walls, the origin of time has been defined as $t = 0$, when the flow is at the side- wall: $x_{\|} = 0$ in Figure 4-3. For time $t < 0$ the flow is given by the steady solution u_o. By assuming that the perpendicular component of the velocity $u_{\perp}$ is independent of time, is equivalent to assuming that it does not depend on the y. This assumption can be considered correct in the region of the flow defined by: $z < 7$ cm and $3b/8 < y < 5b/8$ as is observed in the experiments shown in Figure 3-10 (c).

When time increases the gradient of the time-dependent component of the velocity increases, therefore the shear stress in Eq. (4.15) changes with time. To solve for $u_{\|}(t)$ it is necessary to specify the eddy viscosity ν_t. For this purpose it is assumed that the shear stress, $\tau_{\|}$, at the bottom is given by:

$$\tau_{b\|}(t) \;=\; \tau_{\|}(z'_o,t) \;=\; \alpha(t)\,\tau_{ob\|} \tag{4.16}$$

where $\alpha(t)$ is in principle unknown and is obtained as part of the solution. Using Eq. (4.11) in Eq. (4.16) we obtain:

$$\tau_{b\|}(t) \;=\; \rho\,u_{*\|}^2 \;=\; \rho\,\alpha(t)\,u_*^2\,\sin\theta \tag{4.17}$$

where $u_{*\|}$ is the shear velocity representing $\tau_{b\|}$, and can be written as:

$$u_{*\|} \;=\; \sqrt{\alpha(t)}\,\sqrt{\sin\theta}\,u_* \tag{4.18}$$

In the region $z'_o < z < \eta$ the eddy viscosity, ν_t, is assumed to be scaled by the shear velocity $u_{*\|}$, and in the region $\eta < z < h$, ν_t is assumed to be scaled by the shear velocity that represents the driving pressure gradient of the initial flow, u_*, in

Eq. (4.1). The spatial distribution of ν_t is assumed to be:

$$\nu_t = \begin{cases} \kappa u_* \sqrt{\alpha(t)} \sqrt{\sin\theta}\, z & \text{for } z_o' < z < \eta \\ \kappa u_* z (1 - \frac{z}{h}) & \text{for } \eta < z < h \end{cases} \tag{4.19}$$

The function $\alpha(t)$ defined in Eq. (4.17) represents the magnitude of the bottom shear stress, $\tau_{b\|}$. In order to simplify the solution, α is treated as a parameter ,which is obtained by evaluating Eq. (4.17) at time $t = t_{b/2}$, *i.e.* α is calculated based on the bottom shear stress at the center of the flume. This approximation is justified based on the time dependence observed in the solution of the bottom shear stress, $\tau_{b\|}$. The magnitude of $\tau_{b\|}$ initially presents a fast increase with time, and it reaches a fairly constant value when time gets close to $t_{b/2}$. The variation of $\tau_{b\|}$ with time indicates that the spatial average of $\tau_{b\|}$ over the half-width of the flume can be approximated by the value of $\tau_{b\|}(t_{b/2})$.

Summarizing Eqs (4.13) to (4.19), the equation describing the time dependent component of the velocity $u_\|$ is given by:

$$\frac{\partial u_\|}{\partial t} = \frac{u_*^2}{h} \sin\theta \frac{h}{\eta} + \frac{\partial}{\partial z}(\kappa \sqrt{\alpha} \sqrt{\sin\theta}\, u_*\, z \frac{\partial u_\|}{\partial z}) \tag{4.20}$$

for $z_o' < z < \eta$, and

$$\frac{\partial u_\|}{\partial t} = \frac{\partial}{\partial z}\left(\kappa\, u_*\, z\, (1 - z/h) \frac{\partial u_\|}{\partial z}\right) \tag{4.21}$$

for $\eta < z < h$.

To solve Eqs. (4.20) and (4.21) the initial condition is specified by assuming that the flow is initially described by the stationary solution of Eq. (4.4), therefore:

$$u_\|(t = 0) = 0 \tag{4.22}$$

At the bottom the non-slip condition is used:

$$u_\|(z_o') = 0 \tag{4.23}$$

At the free surface the shear stress is assumed to be equal to zero:

$$\left[\frac{\partial u_{\|}}{\partial z}\right]_h = 0 \tag{4.24}$$

Continuity of the velocity and shear stresses is required at $z = \eta$:

$$u_{\|}(\eta^-) = u_{\|}(\eta^+) \tag{4.25}$$

$$\left[\nu_t \frac{\partial u_{\|}}{\partial z}\right]_{\eta^-} = \left[\nu_t \frac{\partial u_{\|}}{\partial z}\right]_{\eta^+} \tag{4.26}$$

The solution of Eqs (4.20) to (4.26) was obtained at the time $t = t_{b/2}$ defined in Eq. (4.10).

Equations (4.20) to (4.26) were solved numerically by using a finite difference method. The equations were time stepped with a standard explicit Euler scheme. The details of the numerical solution are presented in Appendix B.

The equations involve the parameter α defined in Eq. (4.16), which is unknown. The problem was solved by iteration on α. Assuming an initial value of $\alpha = 1$, Eqs (4.20) to (4.26) were solved to obtain $u_{\|}(t = t_{b/2})$ and $\tau_{b\|}(t = t_{b/2})$. Using Eq. (4.16) a new value of the parameter $\alpha(t = t_{b/2})$ was obtained. This new value of α was used to solve again Eqs (4.20) to (4.26) . In this way a second estimate of $\tau_{b\|}(t = t_{b/2})$ and α was calculated. This process was repeated until convergence of α was achieved within three significant digits.

4.2 Model Solution and Comparison with the Experiments

To obtain the time-dependent component of the flow by using Eqs. (4.20) to (4.26)it is necessary to specify the driving force, that is u_* and the bottom roughness z_o' must be known. For the experiments with beads $z_o' = \mathrm{d}/30$ and for the experiments without beads, $z_o' = \nu/(9u_*\sqrt{\alpha}\sqrt{\sin\theta})$, corresponding to smooth turbulent flow.

The perpendicular component of the velocity can be written as:

$$u_{\perp} = \frac{u_{*\perp}}{\kappa} \ln(\frac{z}{z_{o\perp}}) \tag{4.27}$$

Comparing Eq. (4.27) and (4.6), the value of u_* can be obtained as a function of the shear velocity of the perpendicular component of the flow:

$$u_* = \frac{u_{*\perp}}{\cos\theta} \tag{4.28}$$

$$z_o = z_{o\perp} \tag{4.29}$$

Having the value of u_* the driving force in Eq. (4.13) is known and the $u_{\parallel}$ can be obtained by solving Eqs. (4.20) to (4.26) iterating on α as explained in the previous section.

After solving for the $u_{\parallel}$ at time $t = t_{b/2}$, the component of the velocity in the $\hat{x}$ and $\hat{y}$ - directions were obtained:

$$U(t_{b/2}) = U_{\parallel}(t_{b/2}) \sin\theta + u_{\perp} \cos\theta \tag{4.30}$$

$$V(t_{b/2}) = U_{\parallel}(t_{b/2}) \cos\theta - u_{\perp} \sin\theta \tag{4.31}$$

where $U_{\parallel}(t_{b/2}) = u_{o\parallel} + u_{\parallel}(t_{b/2})$ and $u_{o\parallel}$ and $u_{\perp}$ are given by Eqs. (4.6) to (4.7). The values used of $u_{*\perp}$ and $z_{o\perp}$ were those obtained by fitting a logarithmic profile to the measured perpendicular component of the velocity. These parameters were presented in Tables 3.5 (A) and (B) and are are summarized in Table 4.1. The calculated velocity profiles obtained by using Eqs. (4.30) and (4.31) are compared with the experiments in Figures 4-4 to 4-6 for the cases with beads, and in Figures 4-7 to 4-9 for the cases without beads. The solid line corresponds to the predicted velocity, and the circles to the spatial average velocity profiles measured in the experiments. For the case of the experiments with beads the theoretical bed was chosen at 0.35 times the bead diameter below the top of the beads. For each angle of incidence part (a) of the figure corresponds to the perpendicular component of the velocity. As the input parameters $u_{*\perp}$ and $z_{o\perp}$ were those obtained by fitting a logarithmic profile to

A) Beads	θ	$u_{*\perp}$ (cm/sec)	u_* (cm/sec)	$z_{o\perp}$ (cm)	$t_{b/2}$ (sec)	α
	30	1.38	1.59	0.20	21.84	0.38
	45	1.01	1.43	0.15	22.35	0.41
	60	0.76	1.52	0.19	23.55	0.44
B) No Beads	θ	$u_{*\perp}$ (cm/sec)	u_* (cm/sec)	$z_{o\perp}$ (cm)	$t_{b/2}$ (sec)	α
	30	1.70	1.96	0.34	18.49	0.21
	45	1.35	1.91	0.32	17.21	0.22
	60	0.96	1.92	0.37	18.63	0.23

Table 4.1: Input parameters to the model: $u_{*\perp}$ and $z_{o\perp}$ obtained by fitting a logarithmic velocity profile to the perpendicular component of the velocity (Tables 3.5) (A) and (B). A)Experiments with beads. B)Experiments without beads. The measurements were performed at $y = b/2$ for $\theta = 30^o, 45^o$ and 60^o.

the perpendicular component of the velocity, the theoretical and experimental points must be the same by definition. Parts (b), (c) and (d) of the figures correspond to the $U_{\parallel}$, U and V components of the velocity, respectively.

The results presented in the figures show that the model is able to describe the measured velocity. Although the predicted velocity overestimates the measurements the behavior of the theoretical profiles is in agreement with the experiments. The difference in the prediction and the measurements is more marked in the experiments without the beads. For this case the model was solved assuming that the flow was smooth turbulent.

The effect of the bottom roughness z_o' on the predicted profile in the experiments without the beads was studied. The triangular bars simulating the roughness elements were attached to the bottom of the flume by duct tape. Between two bars part of the duct tape was covering the glass bottom of the flume. As the duct tape presents a corrugation of approximately 1 mm, the model was applied to the experiments without beads by assuming that flow was rough turbulent and the bottom roughness was given by $z_o' = 1$ mm$/30 \approx 0.003$ cm. The resulting velocity profiles do not present any improvement with respect to those obtained under the assumption of smooth turbulent flow. The reason for this is that the resulting bottom roughness obtained by assuming smooth turbulent flow: $z_o' = \nu/(9u_*\sqrt{\alpha}\sqrt{\sin\theta}) \approx 0.001$ cm,

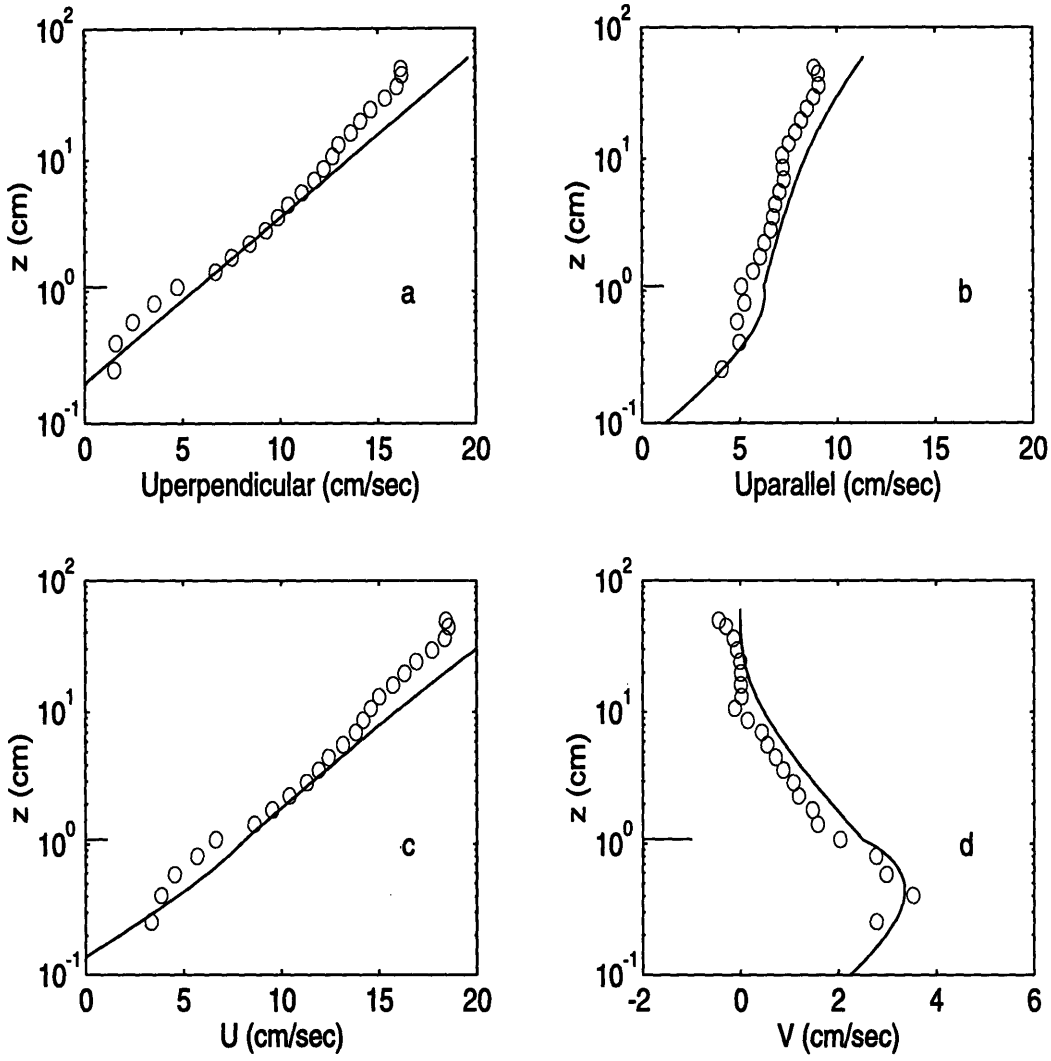

Figure 4-4: Pure current velocity profiles measured at the center of the flume, $y = b/2$, for the experiments with beads and $\theta = 30^o$ a) $U_\perp$ b) $U_\parallel$ c) U and d) V.

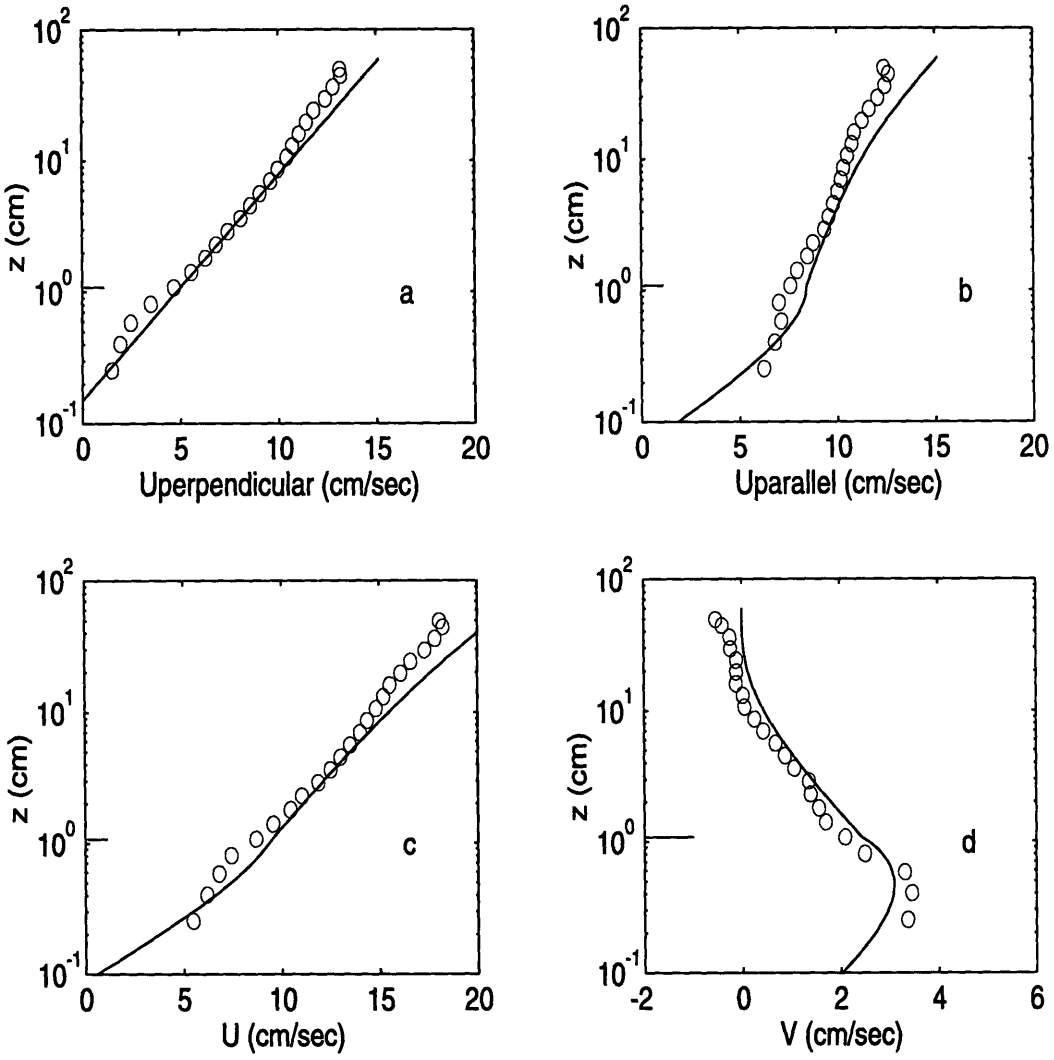

Figure 4-5: Pure current velocity profiles measured at the center of the flume, $y = b/2$, for the experiments with beads and $\theta = 45^o$ a) $U_\perp$ b) $U_\parallel$ c) U and d) V.

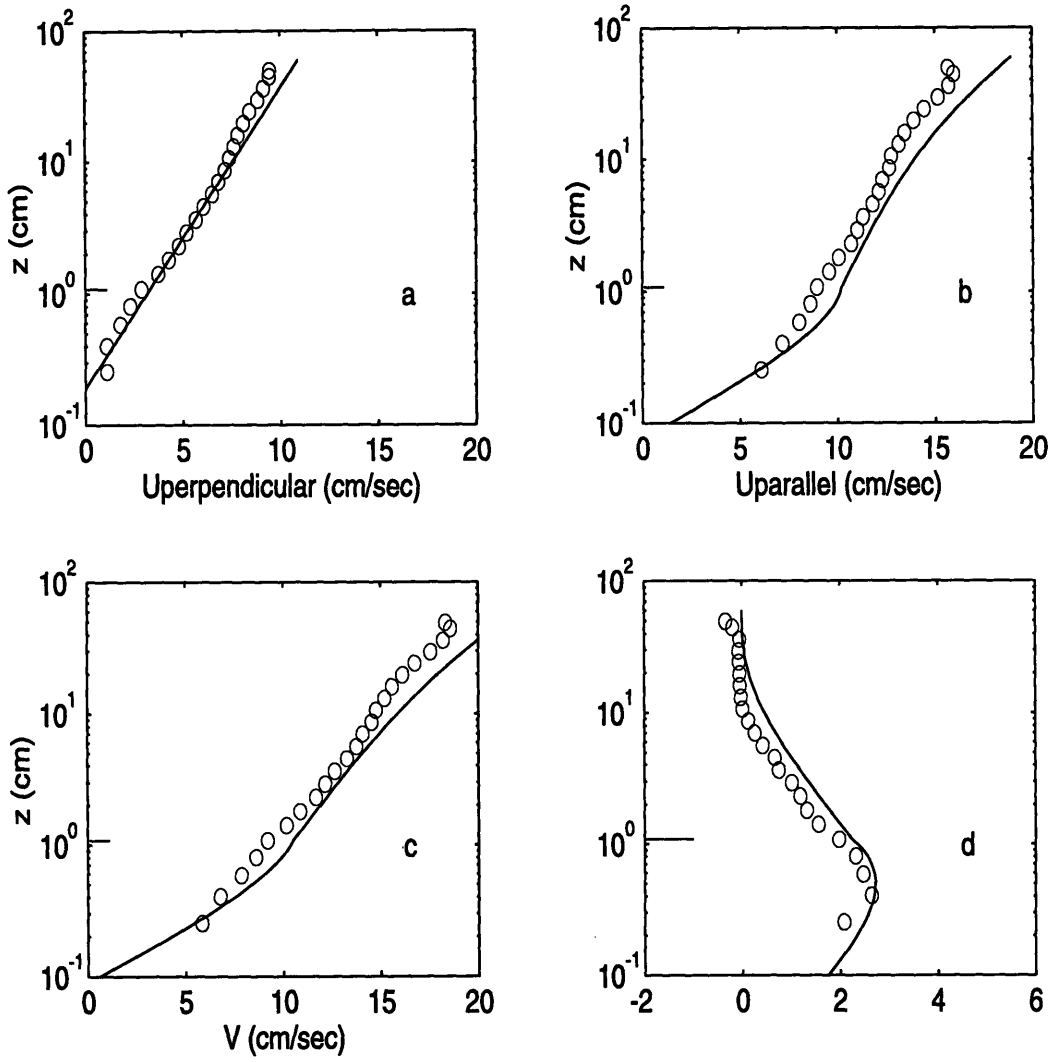

Figure 4-6: Pure current velocity profiles measured at the center of the flume, $y = b/2$, for the experiments with beads and $\theta = 60^o$ a) $U_\perp$ b) $U_\parallel$ c) U and d) V.

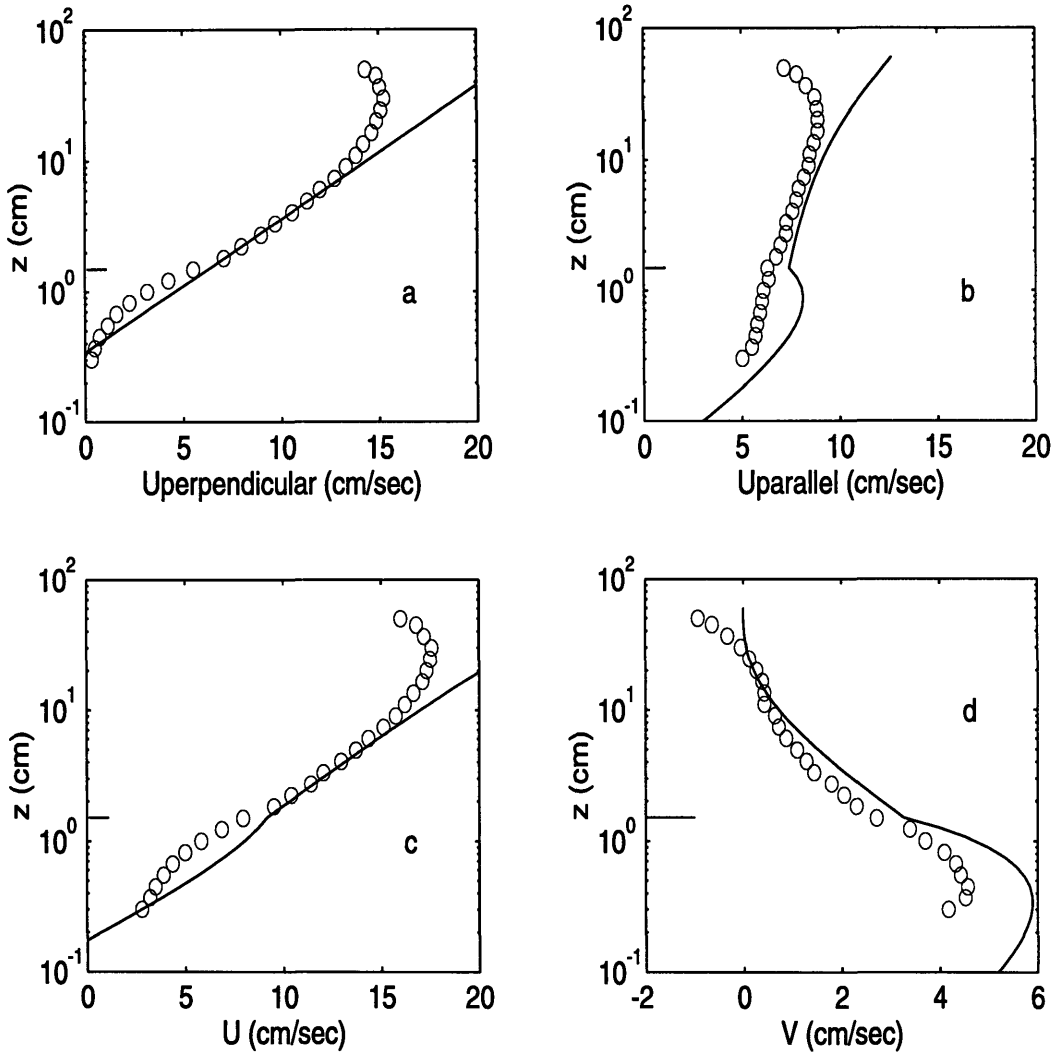

Figure 4-7: Pure current velocity profiles measured at the center of the flume, $y = b/2$, for the experiments without beads and $\theta = 30^o$ a) $U_\perp$ b) $U_\parallel$ c) U and d) V.

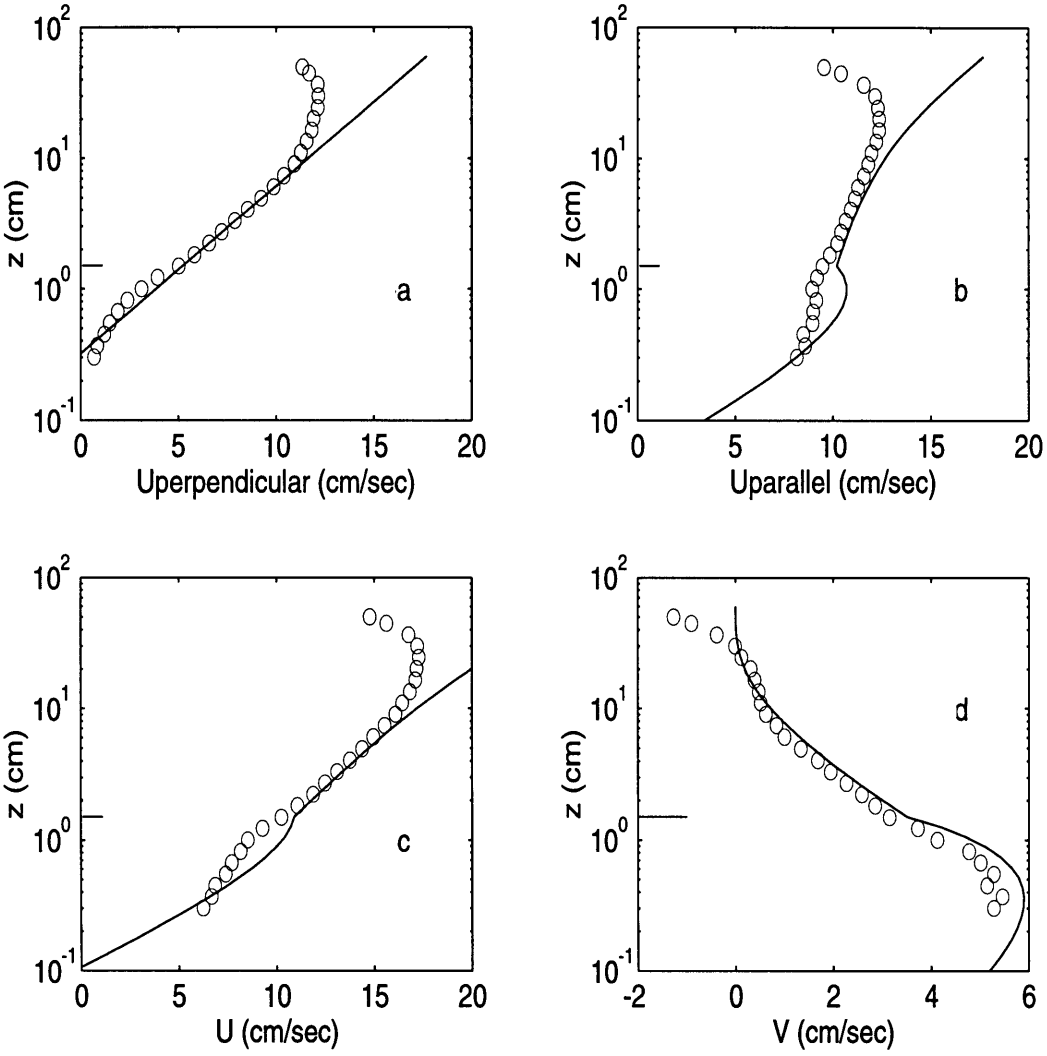

Figure 4-8: Pure current velocity profiles measured at the center of the flume, $y = b/2$, for the experiments without beads and $\theta = 45^o$ a) $U_\perp$ b) $U_\parallel$ c) U and d) V.

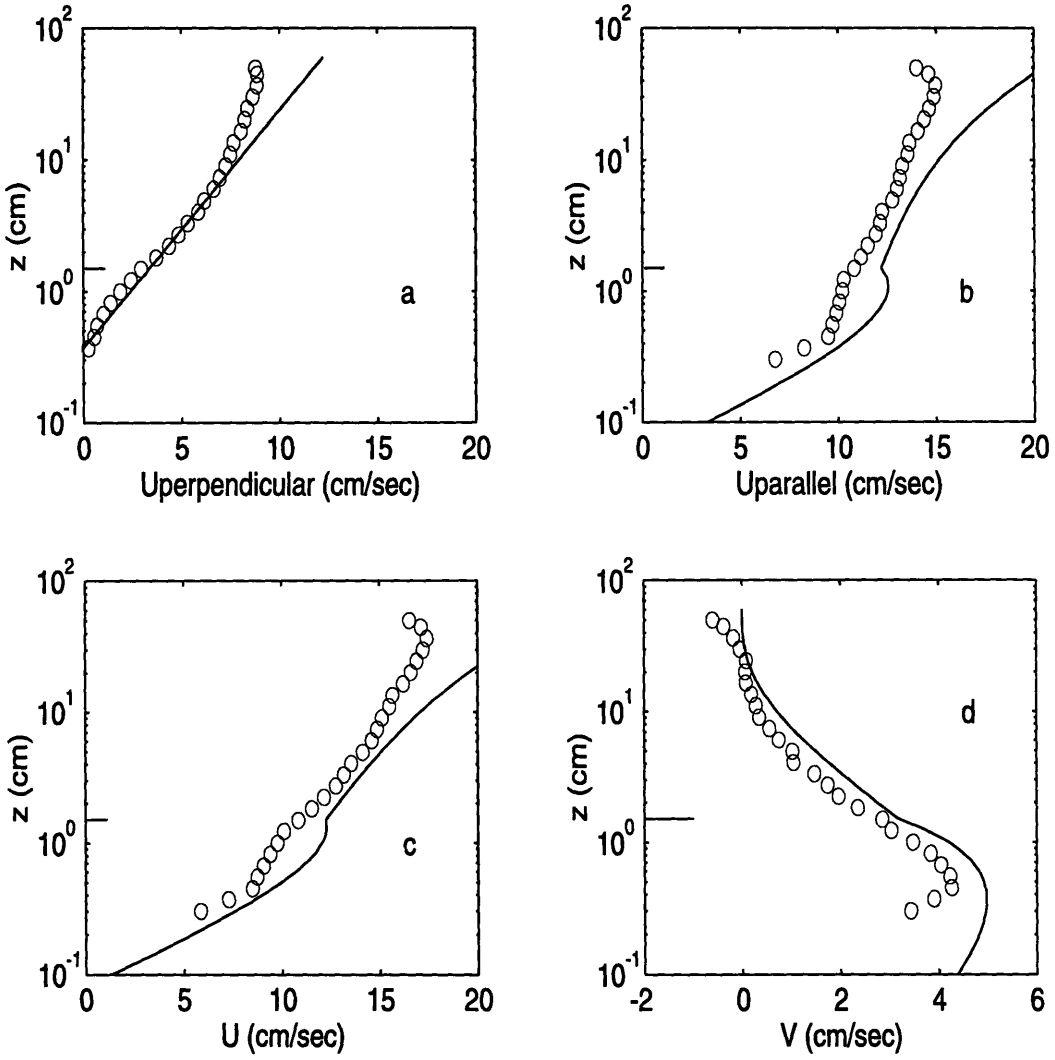

Figure 4-9: Pure current velocity profiles measured at the center of the flume, $y = b/2$, for the experiments without beads and $\theta = 60^o$ a) $U_\perp$ b) $U_\parallel$ c) U and d) V.

which is of the order of 1 mm/30.

The spatial distribution of the driving force defined in Eq. (4.13), implies that the forcing is concentrated in the region $z_o' < z < \eta$. As a consequence of this assumption, , the predicted V - component approaches zero a distance far from the bottom, implying that there is a net flow in in the $\hat{y}$ - direction. The lateral boundaries of the flume imposed the constrain that the depth-average of the V - component of the velocity must be equal to zero. This effect could be considered by introducing a uniform pressure gradient in the $(-\hat{y})$ - direction that drives a "return" flow: v_r. An estimate of the return flow was obtained using the predicted V component of the flow:

$$v_r = \frac{\int_{z_o'}^{h} V \, dz}{h} \tag{4.32}$$

The value obtained in this manner was $v_r \approx 0.3$ cm/sec. This value is small compared with the predicted V component close to the bottom. Therefore, it is expected that the predicted velocity profiles obtained after the incorporation of this pressure gradient will not be significantly different from the one presented in the Figures 4-4 to 4-9.

The spatial distribution of the eddy viscosity in Eq. (4.19) was assumed to be parabolic for $z > \eta$. The model was also solved by assuming that the eddy viscosity for $z > \eta$ was linear, *i.e* $\nu_t = \kappa u_* z$. It was found that the predicted velocity profiles obtained by using a linear ν_t was the same as the one obtained by assuming that ν_t is parabolic in the region $z > \eta$. This can be explained because the driving force , which is concentrated in the region $z_o' < z < \eta$, acts on the lower fluid during the travel time $t_{b/2}$ defined in Eq. (4.10). The fluid far from the bottom will experience the presence of this force only by diffusion of vorticity from the lower region of the flow. The travel time $t_{b/2}$ ($\approx$ 20 sec) is small compared to the time it takes vorticity originating at the bottom to diffuse over the entire depth of the flow. Therefore, for times $t < t_{b/2}$, vorticity is confined in the lower region and the flow close to the free surface will not experience the presence of the bottom. As for $z << h$, the parabolic eddy viscosity can be approximated by $\nu_t \approx \kappa u_* z$, the use of a linear eddy viscosity

will give the same solution at the short time considered.

It should be emphasized that, despite its approximate nature, the present model is able to describe quantitatively the results of the pure current experiments. In particular, it predicts successfully the shape of the spatial average transverse component of the flow close to the bottom for all three angles studied experimentally.

Chapter 5

Wave-Current model for Experimental Conditions

The simple model presented in Chapter 4 is extended to describe the near-bottom flow when waves and currents are superimposed. The combined flow is assumed to be initially in equilibrium and the Grant-Madsen model (1986) is used to describe the time average velocity. The perpendicular component of the resulting time average shear stress at the bottom is assumed to be balanced by the time average drag force. The component of the time average bottom shear stress in the direction parallel to the ripple axis is used to represent the driving force.

5.1 Description of the model

The first step is to specify the initial flow consisting on a periodic wave and a current in the $\hat{x}$-direction. The flow is assumed to be known and to be described by the linearized boundary layer equation:

$$\frac{\partial u_o}{\partial t} = -\frac{1}{\rho}\frac{\partial p}{\partial x} + \frac{\partial}{\partial z}\left(\nu_{ot}\frac{\partial u_o}{\partial z}\right) \tag{5.1}$$

where u_o is the flow velocity, p is the pressure and ν_{ot} is the turbulent eddy viscosity. Following the Grant-Madsen model (1979), the eddy viscosity is assumed to be time-

invariant an to be given by:

$$\nu_{ot} = \begin{cases} \kappa\, u_{*wc}\, z & \text{for} \quad z < \delta_{wc} \\ \kappa\, u_{*c}\, z & \text{for} \quad z > \delta_{wc} \end{cases} \tag{5.2}$$

where $\delta_{wc} = 2\,\kappa u_{*wc}/\omega$ is the wave boundary layer thickness, u_{*wc} is the shear velocity that represents the combined wave-current flow, and u_{*c} is the current shear velocity. The velocity and the pressure are written in terms of their mean and time-dependent components denoted by the subscripts "c" and "w" respectively:

$$\begin{aligned} u_o &= u_{oc} + u_w \\ p &= p_c + p_w \end{aligned} \tag{5.3}$$

Combining Eqs. (5.1), (5.2) and (5.3), two independent equations for the wave and the current are obtained. These equations are solved by requiring the boundary condition at the bottom:

$$u_{oc} = u_w = 0 \quad at \quad z = z_o \tag{5.4}$$

where z_o is the bottom roughness. The other boundary condition for the wave velocity is $u_w \rightarrow U_b$ for $z \rightarrow' \infty'$, where $U_b = u_b \cos\omega t$ is the near-bottom velocity predicted by potential theory.

The solution for the wave component of the flow inside the wave boundary layer is given by:

$$u_w = u_b\, \Re\left[\left(1 - \frac{ker\, 2\sqrt{\zeta} + i\, kei\, 2\sqrt{\zeta}}{ker\, 2\sqrt{\zeta_o} + i\, kei\, 2\sqrt{\zeta_o}}\right) e^{i\omega t}\right] \tag{5.5}$$

where *ker* and *kei* are the Kelvin functions of order zero, $\zeta = z\omega/(\kappa u_{*wc})$, ζ_o is the value of ζ at $z = z_o$, ω is the frequency, and u_b is the maximum near-bottom velocity.

For the mean component of the flow the solution:

$$u_{oc} = \begin{cases} \frac{u_{*c}^2}{\kappa u_{*wc}} \ln \frac{z}{z_o} & \text{for } z < \delta_{wc} \\ \\ \frac{u_{*c}}{\kappa} \ln \frac{z}{z_{oa}} & \text{for } z > \delta_{wc} \end{cases} \tag{5.6}$$

where z_{oa} is the apparent bottom roughness experienced by the current in the presence of the waves and is obtained by matching the current solution at $z = \delta_{wc}$:

$$z_o = \delta_{wc} \left(\frac{z_{oa}}{\delta_{wc}}\right)^{u_{*wc}/u_{*c}} \tag{5.7}$$

The flow solution given by Eqs (5.5) and (5.6), is expressed in terms of u_{*wc} that in principle is unknown. The value of u_{*wc} is determined by the closure assumption based on the maximum bottom shear stress:

$$\tau_b = \rho\, u_{*wc}^2 = \tau_{w_{max}} + \tau_c = \rho\, C_{\mu_o} u_{*w}^2 \tag{5.8}$$

in which $u_{*w} = \sqrt{\tau_{w_{max}}/\rho}$ is the shear velocity based on the maximum wave bottom shear stress obtained as:

$$\tau_{w_{max}} = \left| \rho \nu_{ot} \frac{\partial u_w}{\partial z} \right|_{z=z_o} \tag{5.9}$$

and, for co-directional waves and current,

$$C_{\mu_o} = 1 + \mu_o = 1 + \left(\frac{u_{*c}}{u_{*w}}\right)^2 \tag{5.10}$$

where $u_{*c} = \sqrt{\tau_c/\rho}$ is the current shear velocity. The maximum wave bottom shear stress is expressed in terms of a friction factor f_{wc}:

$$\tau_{w_{max}} = \rho\, u_{*w}^2 = \rho\, \frac{1}{2}\, f_{wc} u_b^2 \tag{5.11}$$

An implicit equation for the wave friction factor in the presence of a current is obtained

after combining Eqs. (5.9), (5.10) and (5.11):

$$\sqrt{f_{wc}} = \kappa \sqrt{C_{\mu_o} 2\zeta_o} \left| -\frac{ker' \, 2\sqrt{\zeta_o} + i \, kei' \, 2\sqrt{\zeta_o}}{ker \, 2\sqrt{\zeta_o} + i \, kei \, 2\sqrt{\zeta_o}} \right| \tag{5.12}$$

in which ker' and kei' are the derivatives of the Kelvin function of order zero.

Specifying for the waves the near-bottom velocity u_b and the frequency ω and for the current the shear velocity u_{*c} and the apparent roughness z_{oa}, the Grant-Madsen model is used to describe the initial mean flow u_{oc}. As for the pure current case, the time at which the driving force starts to act is defined as $t = 0$. For times $t < 0$ the mean component of the flow u_{oc} is given by Eqs. (5.6) , and can be written in the $(\hat{x}_\perp, \hat{x}_\parallel)$ coordinate system, Figure 4-1:

$$u_{oc}\hat{x} = u_{oc\perp} \, \hat{x}_\perp + u_{oc\parallel} \, \hat{x}_\parallel \tag{5.13}$$

Combining Eqs. (5.6) and (5.13):

$$u_{oc\perp} = \begin{cases} \frac{u_{*c}^2}{\kappa u_{*wc}} \cos\theta \, \ln \frac{z}{z_o} & \text{for} \quad z < \delta_{wc} \\ \\ \frac{u_{*c}}{\kappa} \cos\theta \, \ln \frac{z}{z_{oa}} & \text{for} \quad z > \delta_{wc} \end{cases} \tag{5.14}$$

$$u_{oc\parallel} = \begin{cases} \frac{u_{*c}^2}{\kappa u_{*wc}} \sin\theta \, \ln \frac{z}{z_o} & \text{for} \quad z < \delta_{wc} \\ \\ \frac{u_{*c}}{\kappa} \sin\theta \, \ln \frac{z}{z_{oa}} & \text{for} \quad z > \delta_{wc} \end{cases} \tag{5.15}$$

Following the procedure used in the pure current case, the unbalanced component of the time average bottom shear stress in the parallel direction to the ripple axis, $\tau_{c\parallel} = \rho \, u_{*c}^2 \sin\theta$, is used to represent the driving force. The driving force will induce a flow along the ripple axis and the parallel component of the velocity will increase with time and is written as:

$$U_{c\parallel}(t) = u_{oc\parallel} + u_{c\parallel}(t) \tag{5.16}$$

The equation describing the non-oscillatory time-dependent part of the parallel component of the velocity is, as for the pure current case, a diffusion equation with a forcing term:

$$\frac{\partial u_{c\parallel}}{\partial t} = \frac{u_{*c}^2}{h} \sin\theta \, f(z) + \frac{\partial}{\partial z}\left(\nu_t \frac{\partial u_{c\parallel}}{\partial z}\right) \tag{5.17}$$

where $f(z)$ represents the forcing term and is assumed to be uniformly distributed in the region below the crest of the ripples:

$$f(z) = \begin{cases} \frac{h}{\eta} & \text{for} \quad z_o' < z < \eta \\ 0 & \text{for} \quad \eta < z < h \end{cases} \tag{5.18}$$

in which z_o' is the bottom roughness in the parallel direction and is assumed to be due to skin friction. A three-layer eddy viscosity, ν_t, is used in Eq. (5.17), and is assumed to be:

$$\nu_t = \begin{cases} \kappa \, u_{*wc}' \, z & \text{for} \quad z_o' < z < \eta \\ \kappa \, u_{*wc} \, z & \text{for} \quad \eta < z < \delta_{wc} \\ \kappa \, u_{*c} \, z & \text{for} \quad \delta_{wc} < z < h \end{cases} \tag{5.19}$$

where $u_{*wc}' = \sqrt{|\tau_b'|/\rho}$ is the shear velocity based on the maximum bottom shear stress due to skin friction.

By assuming that the eddy viscosity in Eq. (5.19) is scaled by the shear velocity u_{*wc}' in the region $z_o' < z < \eta$ is equivalent to assuming the thickness of the wave boundary layer due to skin friction, δ_{wc}', extends up to $z = \eta$. In principle, this is not necessarily true, and is reasonable to expect that $\delta_{wc}' < \eta$. Therefore, the model is assuming that in the region $\delta_{wc}' < z < \eta$ the shear stress is still represented by u_{*wc}'.

The shear velocity u_{*wc}' is obtained as part of the solution by assuming that, at the bottom, the shear stress due to skin friction is given by the sum of the current bottom shear stress, $\vec{\tau_c}'$, and, the maximum wave bottom shear stress , $\vec{\tau_w}'$:

$$\vec{\tau_b}' = \vec{\tau_c}' + \vec{\tau_w}' \tag{5.20}$$

where the bottom current shear stress is in the $\hat{x}_{\|}$ - direction, and is expressed as:

$$\vec{\tau}_c' = \rho\, u_{*c}'^2\, \hat{x}_{\|} \tag{5.21}$$

and the maximum wave bottom shear stress is assumed to be in the $\hat{x}$ - direction and is expressed in terms of a skin friction factor f_{wc}':

$$\vec{\tau}_w' = \rho\, u_{*w}'^2\, \hat{x} = \frac{1}{2}\, \rho\, f_{wc}'\, u_b^2\, \hat{x} \tag{5.22}$$

Combining Eqs. (5.20), (5.21) and (5.22):

$$u_{*wc}'^2 = C_\mu'\, u_w'^2 \tag{5.23}$$

where C_μ' is,

$$C_\mu' = \sqrt{1 + 2\,\mu'\,\sin\theta + \mu'^2} \tag{5.24}$$

and

$$\mu' = (\frac{u_{*c}'}{u_{*w}'})^2 \tag{5.25}$$

The Grant-Madsen model is again applied to obtain an expression for the skin friction factor:

$$\sqrt{f_{wc}'} = \kappa \sqrt{C_{\mu'} 2\zeta_o'} \left| -\frac{ker'\, 2\sqrt{\zeta_o'} + i\, kei'\, 2\sqrt{\zeta_o'}}{ker\, 2\sqrt{\zeta_o'} + i\, kei\, 2\sqrt{\zeta_o'}} \right| \tag{5.26}$$

in which $\zeta_o' = z_o'\omega/(\kappa u_{*wc}')$.

The initial condition used to solve Eq. (5.17) is obtained by assuming that the current is initially described by the stationary solution in Eq. (5.6):

$$u_{c\|}(t=0) = 0 \tag{5.27}$$

The boundary conditions are specified by requiring continuity of the velocity at $z = z_o'$, $z = \eta$ and $z = \delta_{wc}$:

$$u_{c\|}(z_o') = 0$$

$$
\begin{aligned}
u_{c\|}(\eta^-) &= u_{c\|}(\eta^+) \\
u_{c\|}(\delta_{wc}^-) &= u_{c\|}(\delta_{wc}^+)
\end{aligned}
\tag{5.28}
$$

and continuity of the shear stress at $z = \eta$ and $z = \delta_{wc}$:

$$
\begin{aligned}
\left[\nu_t \frac{\partial u_{c\|}}{\partial z}\right]_{\eta^-} &= \left[\nu_t \frac{\partial u_{c\|}}{\partial z}\right]_{\eta^+} \\
\left[\nu_t \frac{\partial u_{c\|}}{\partial z}\right]_{\delta_{wc}^-} &= \left[\nu_t \frac{\partial u_{c\|}}{\partial z}\right]_{\delta_{wc}^+}
\end{aligned}
\tag{5.29}
$$

At the free surface the shear stress is assumed must be zero:

$$
\left[\frac{\partial u_{c\|}}{\partial z}\right]_h = 0 \tag{5.30}
$$

5.2 Model Solution

5.2.1 Determination of the initial flow u_{oc}

It is assumed that the near-bottom orbital velocity u_b and the frequency ω are known. The current can be specified in terms of the current shear velocity u_{*c} and the apparent roughness z_{oa}. These parameters are obtained by fitting a logarithmic velocity profile in the region $z > \delta_{wc}$ to the time average velocity in the perpendicular direction. Expressing the perpendicular component of the velocity for $z > \delta_{wc}$ as:

$$
u_{c\perp} = \frac{u_{*\perp}}{\kappa} \ln\left(\frac{z}{z_{oa\perp}}\right) \tag{5.31}
$$

comparison between Eqs. (5.14) and (5.31) give:

$$
\begin{aligned}
u_{*c} &= \frac{u_{*\perp}}{\cos\theta} \\
z_{oa} &= z_{oa\perp}
\end{aligned}
\tag{5.32}
$$

For a complete characterization of the initial flow it is necessary to calculate u_{*wc} to express the velocity in the region inside δ_{wc}. For this purpose, an initial value of the friction factor $f_{wc} = 0.2$ is used to obtain $u_{*w} = \sqrt{f_{wc}/2} u_b$ and the Grant-Madsen model is applied as follows:

i) $\mu_o = (u_{*c}/u_{*w})^2$

ii) $C_{\mu_o} = 1 + \mu_o$

iii) $u_{*wc} = \sqrt{C_{\mu_o}}\, u_{*w}$

iv) $\delta_{wc} = 2\,\kappa\, u_{*wc}/\omega$

v) $z_o = \delta_{wc}(\frac{z_{oa}}{\delta_{wc}})^{u_{*wc}/u_{*c}}$

vi) $f_{wc}(z_o)$ by solving Eq. (5.12)

vii) $u_{*w} = \sqrt{f_{wc}/2}\, u_b$

viii) The new estimate of u_{*w} obtained in vii) is used to calculate a new value of μ_o. The steps from i) to vii) are repeated until convergence in μ_o is achieved. The final values of u_{*wc} and z_o are used in Eqs (5.14) and (5.15) to express the initial mean flow in the perpendicular and parallel directions, respectively. The evaluation of the friction factor f_{wc} in step vi) was done by using an approximate explicit equation derived from Eq. (5.12) by Madsen (1994).

5.2.2 Determination of $u_{c\|}(t)$

The non-oscillatory time-dependent part of the parallel component of the velocity is described by Eqs. (5.17) to (5.19). As the eddy viscosity in the lower region of the flow $z < \eta$ depends on u'_{*wc} which is obtained as part of the solution an iterative procedure similar to the one described above is required. It is assumed initially that $u'_{*c} = 0$, *i.e* $\mu' = 0$, and z'_o is known. For the experiments with beads the value of $z'_o = d/30$ and for the experiments without the beads the bottom roughness due to skin friction is assumed to be the one corresponding to smooth turbulent flow, $z'_o = \nu/(9\, u'_{*wc})$. The solution of $u_{c\|}(t)$ is obtained as follows:

i) $C'_\mu = \sqrt{1 + 2\mu' \sin\theta + \mu'^2}$

ii) $f'_{wc}(z'_o)$ by solving Eq. (5.26)

iii) $u'_{*w} = \sqrt{f'_{wc}/2}\, u_b$

iv) $u'_{*wc} = \sqrt{C'_\mu}\, u'_{*w}$

v) Solve Eqs. (5.17), (5.18), (5.19) subject to the initial and boundary conditions specified in Eqs. (5.27) to (5.30) at the given time $t_{b/2}$ defined in Eq (4.10).

vi) Evaluate the current shear stress at the bottom, $\tau'_c = \rho\, \kappa\, u'_{*wc} z\, \partial u_{c\|}/\partial z$ at $z = z'_o$ and at $t = t_{b/2}$.

vii) Obtain $u'_{*c} = \sqrt{\tau'_c/\rho}$

viii) Obtain $\mu' = (u'_{*c}/u'_{*w})^2$ with the estimates of u'_{*w} and u'_{*c} calculated in steps iii) and vii) respectively. The steps i) to viii) are repeated until the value of μ' converges. The Eqs (5.17), (5.18), (5.19) and (5.27) to (5.30) were solved numerically by using a finite difference method and time stepped with a standard explicit Euler scheme as explained in Appendix B. The numerical scheme for waves and currents differs from the one used for the pure current case by the addition of the intermediate region between $\eta < z < \delta_{wc}$. To evaluate the friction factor f'_{wc} in step ii) the explicit equation for (5.26) derived by Madsen (1994) was used.

5.3 Comparison with the experiments

Measurements of the velocity profile were obtained when second order Stokes waves of T = 2.63 sec and an amplitude of $\approx$ 6 cm were superimposed to the current. The ripples were placed at 45^o with respect to the incident flow. The measurements were done only at the center of the flume, $y = b/2$, and at three locations along the $\hat{x}$ - axis: over the trough between two ripples and over both crests. These measurements were performed without beads and with beads. The profiles of the first-harmonic wave amplitude and phase obtained in the wave-current experiments are shown in Figures 5-1 and 5-2. Figure 5-1 corresponds to the experiments with beads and Figure 5-2 to the experiments without beads. The profile measured over the trough between two ripples is indicated by 'o', the profiles measured over the crests are indicated by '.'.

The first harmonic wave amplitude of the $U(1)$ - component of the flow is shown in part (a) of each figure. The profiles present similar characteristics to those measured

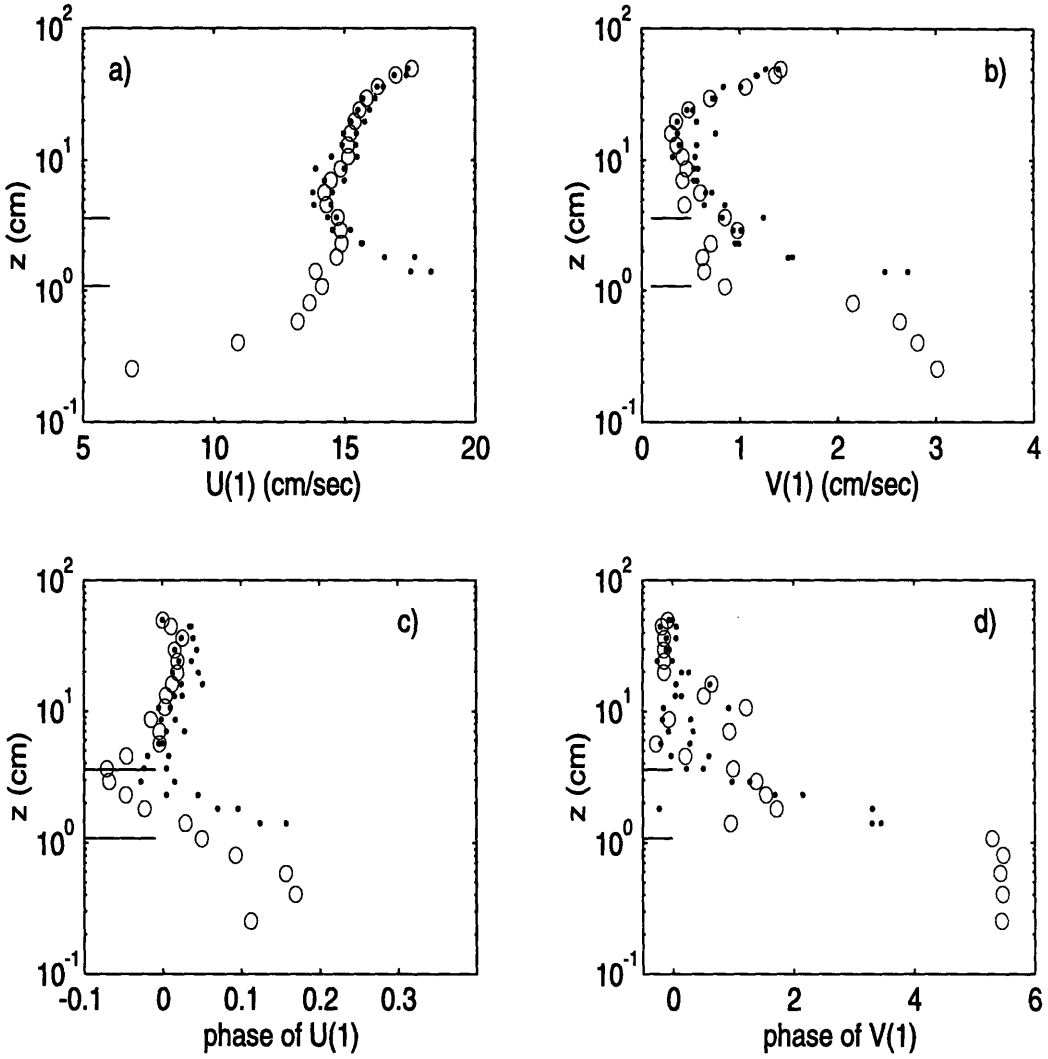

Figure 5-1: Wave amplitude and phase of the first harmonic obtained in the wave and current experiments with beads. The measurements were performed at the center of the flume, $y = b/2$, and $\theta = 45^o$. o: Profile over the trough .: Profile over the crests a) $U_{(1)}$ b) $V_{(1)}$ c) phase of $U_{(1)}$ (radians) d) phase of $V_{(1)}$ (radians). The phases are plotted relative to the phase of $U_{(1)}$ measured at $z = 50$ cm. The horizontal lines represent the ripple height and the wave boundary layer thickness

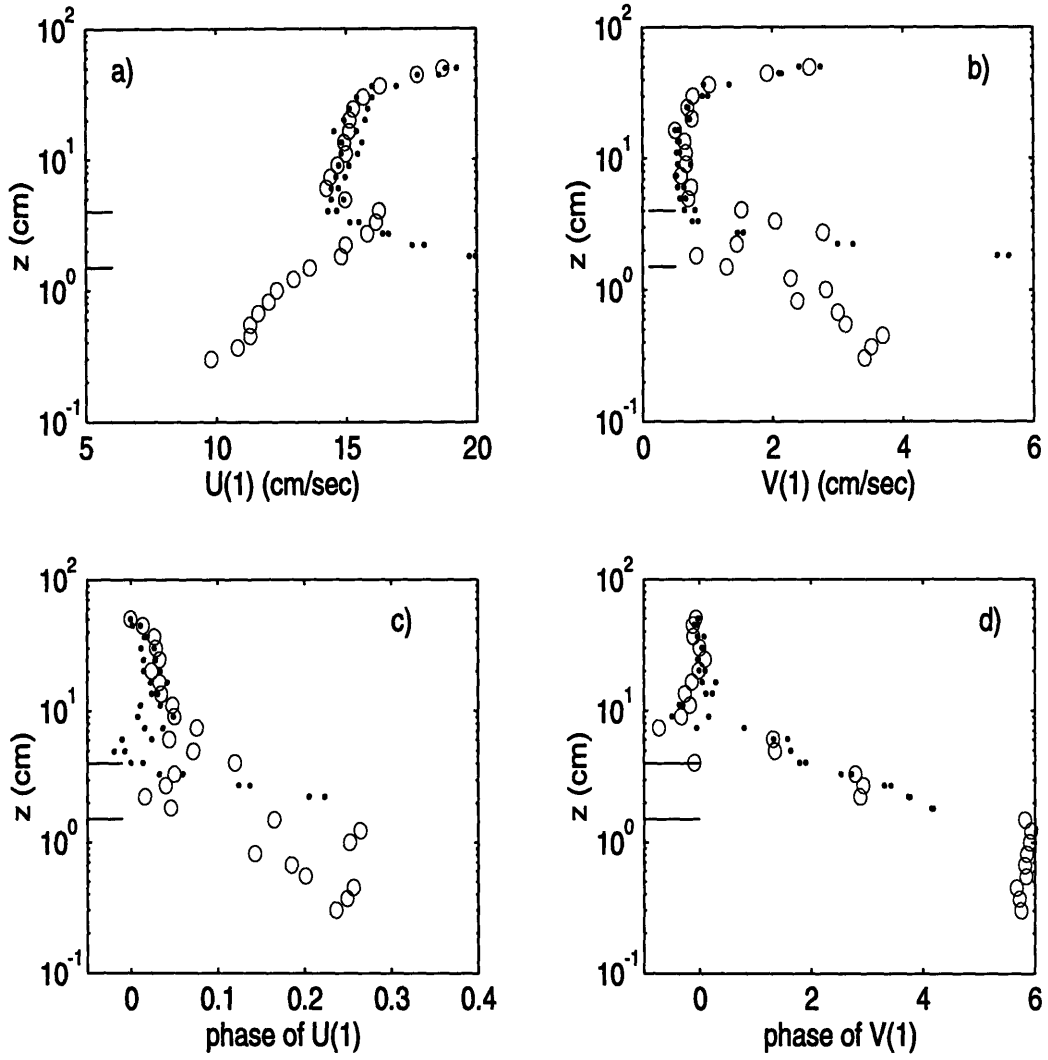

Figure 5-2: Wave amplitude and phase of the first harmonic in the wave and current experiments without beads. The measurements were performed at the center of the flume, $y = b/2$, and $\theta = 45^o$. o: Profile over the trough .: Profile over the crests a) $U_{(1)}$ b) $V_{(1)}$ c) phase of $U_{(1)}$ (radians) d) phase of $V_{(1)}$ (radians). The phases are plotted relative to the phase of $U_{(1)}$ measured at $z = 50$ cm. The horizontal lines represent the ripple height and the wave boundary layer thickness

in the pure wave experiments presented in Chapter 3. The effect of the individual bottom roughness elements is felt up to a height of $z \approx 4$ cm. The gradients in the $U(1)$ - component extends to an elevation of $z \approx 6$ cm suggesting that the thickness of the wave boundary layer is between 4 to 6 cm above the bottom.

Part (b) of each figure shows the first harmonic amplitude of the $V(1)$ - component. Close to the bottom it presents a value of approximately 3 to 4 cm/sec and it starts to decrease when z increases. For elevations larger than 4 cm it remains approximately constant until $z \approx 20$ cm where it starts to increase.

The time-average velocity profiles of the perpendicular component of the velocity obtained in the experiments with beads and without beads are shown in Figures 5-3 (a) and 5-4 (a). A change in the slope of the profile is observed at at a height of ≈ 4 cm above the bottom.

These observations suggest that the wave boundary layer is at an elevation of $z \approx 4$ cm measured from the bottom of the flume. The predicted wave boundary layer thickness $\delta_{wc} = 2\kappa u_{*wc}/\omega$ obtained after applying the Grant-Madsen model as explained in section 5.2.1 is of the order of 2.5 cm, *i.e.* considerably smaller than the value observed in the experiments. To take into account the enhanced boundary layer, it was decided to follow Mathisen and Madsen (1996) and modify the the Grant-Madsen model by replacing the predicted wave boundary layer thickness by the one observed in the experiments. For the experiments with beads the theoretical bed is defined at 0.35 times the bead diameter (d =0.64 cm) below the top of the beads. Therefore the wave boundary thickness used in these experiments was $\delta_{wc} = (4 - 0.65 * .64)$ cm . For the experiments without beads the wave boundary layer thickness used was $\delta_{wc} = 4$ cm.

Energy attenuation measurements were performed for the combined wave-current experiments with and without beads when $\theta = 45^o$. The amplitude of the incident wave obtained in the attenuation experiments were used to estimate the near-bottom orbital velocity. For the experiments with beads $u_b = 16.72$ cm/sec and for the experiments without beads $u_b = 16.64$ cm/sec. These estimates of u_b were used as input to the model.

	δ_{wc}(cm)	u_b(cm/sec)	u_{*c}(cm/sec)	z_{oa}(cm)	u_{*wc}(cm/sec)	u_{*w}(cm/sec)	f_{wc}	z_o(cm)
Beads	3.6	16.72	2.73	1.12	5.83	5.16	0.19	0.26
No Beads	4.0	16.64	2.97	2.32	7.84	7.26	0.38	0.95

Table 5.1: Input parameters to the Grant-Madsen model used to obtain the initial flow : u_b, $u_{*c} = u_{*c\perp}/\cos\theta$, $z_{oa} = z_{oa\perp}$, $\delta_{wc} \approx 4$ cm. Output parameters: u_{*wc}, u_{*w},f_{wc} and z_o

	u_b(cm/sec)	u_{*c}(cm/sec)	u_{*wc} (cm/sec)	f'_{wc}	u'_{*wc}(cm/sec)	u'_{*c}(cm/sec)	$t_{b/2}$(sec)
Beads	16.72	2.73	5.83	0.06	2.87	1.59	12.82
No Beads	16.64	2.97	7.84	0.03	2.19	1.35	13.70

Table 5.2: Input parameters to the extended model for waves and currents :u_b, u_{*c} and u_{*wc}. Output parameters: f'_{wc}, u'_{*wc}, u'_{*c}, $t_{b/2}$

The current specification used as input to the model, u_{*c} and z_{oa}, were obtained from Eq. (5.32) after fitting a logarithmic velocity profile to the measurements of the perpendicular component of the velocity in the region $4 < z < 9$ cm . The input and output parameters to the model are summarized in Table 5.1. The values obtained for u_{*wc} and z_o were then used in Eq. (5.14) and plotted together with the experiments in Figures 5-3 (a) and 5-4 (a). The predicted profile inside the wave boundary layer obtained by applying the Grant-Madsen model with the modified wave boundary layer agrees fairly well with experiments down to $z = \eta$ and is used to describe the initial flow.

Having defined the initial flow, $u_{c\parallel}(t_{b/2})$ is obtained following the procedure described in section 5.2.2. The input prescribed to run the model were u_b, z'_o, u_{*c} and u_{*wc}. They are summarized in Table 5.2. Knowing $u_{c\parallel}(t_{b/2})$, the component of the velocity in the $\hat{x}$ - direction and $\hat{y}$ - direction are obtained:

$$U(t_{b/2}) = U_{\parallel}(t_{b/2}) \sin\theta + u_{oc\perp} \cos\theta \tag{5.33}$$

$$V(t_{b/2}) = U_{\parallel}(t_{b/2}) \cos\theta - u_{oc\perp} \sin\theta \tag{5.34}$$

where $U_{\parallel}(t_{b/2}) = u_{oc\parallel} + u_{\parallel}(t_{b/2})$, $u_{oc\parallel}$ and $u_{oc\perp}$ are given in Eqs. (5.14) and (5.15),

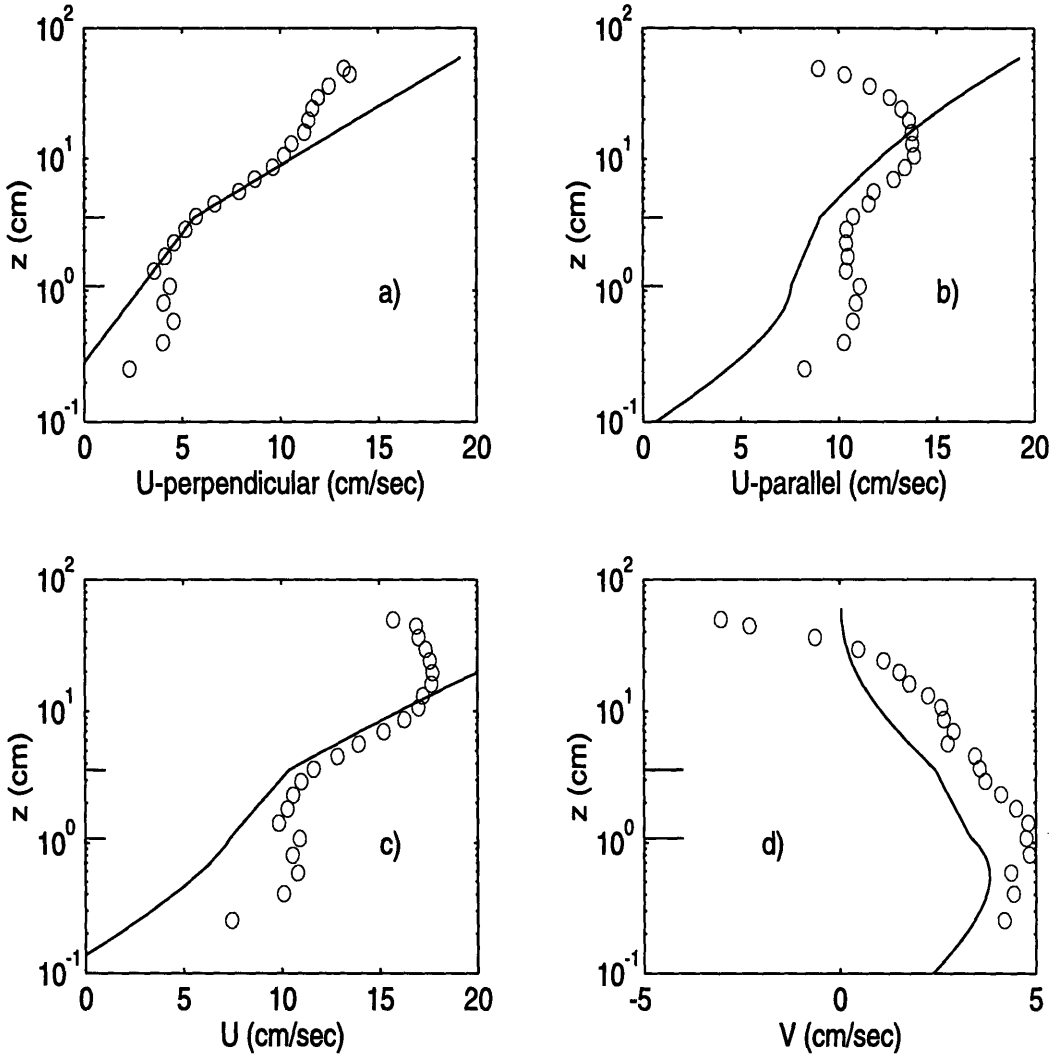

Figure 5-3: Time average velocity profiles measured at the center of the flume, $y = b/2$, in the wave and current experiments with beads for $\theta = 45^o$ a) $U_\perp$ b) $U_\parallel$ c) U and d) V.

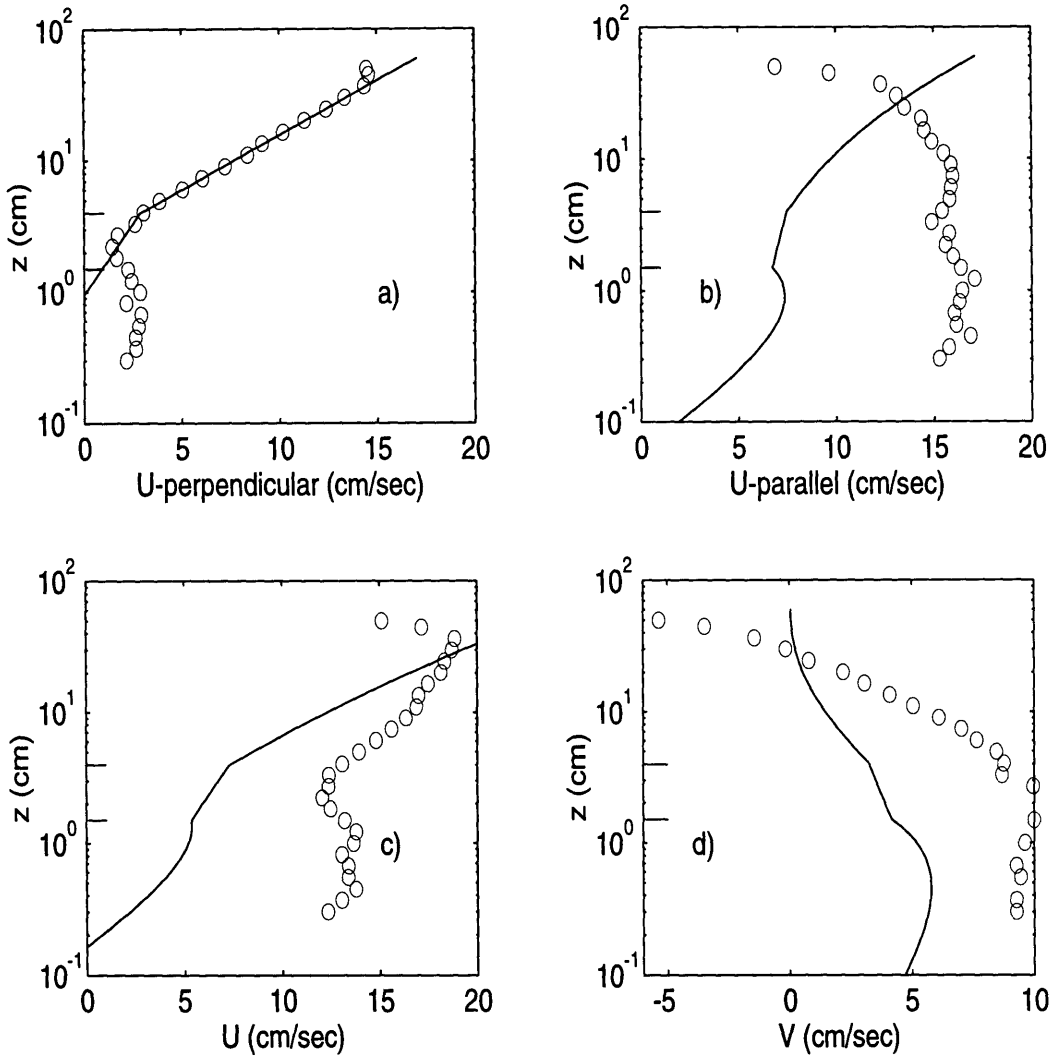

Figure 5-4: Time average velocity profiles measured at the center of the flume, $y = b/2$, in the wave and current experiments without beads for $\theta = 45^o$ a) $U_\perp$ b) $U_\parallel$ c) U and d) V.

respectively. The predicted $U_{\|}(t_{b/2})$, $U(t_{b/2})$ and $V(t_{b/2})$ are plotted together with the experimental results in Figures 5-3 (b), (c) and (d), respectively, for the experiment with beads, and in Figures 5-4 (b) ,(c) and (d), for the experiment without beads. The symbols represent the experiments and the solid line the predictions.

The predictions for the case of the experiments with beads presented in Figure 5-3 underestimate the measured profiles but qualitative agreement between theory and experiments is observed. The experiments show a change in the slope both at $z = \eta$ and at $z = \delta_{wc}$, a feature reproduced by the predicted velocity.

For the experiment without beads the predicted profiles are not in good agreement with the measurements. The experimental profile presented in Figure 5-4 (d) show a large value of the V - component of the flow of about 10 cm/sec in the region $z < 4$ cm. The proposed model is based on a force concentrated close to the bottom which drives the fluid along the ripple axis. The finite time $t < t_{b/2}$ is not enough to advect the flow in the region far from the bottom. The solution of the model is basically a correction of the initial flow in the region close to the bottom. Comparing the experimental profiles of the perpendicular and parallel components of the velocity it is clearly seen that $U_{\|}$ does not present the same characteristics as $U_{\perp}$ in the region $z > \delta_{wc}$. Eqs. (5.14) and (5.15) indicate that for the particular case of $\theta = 45^{o}$ the initial flow in the perpendicular and parallel direction are the same. Therefore a correction close to the bottom will not be able to reproduce the measured $U_{\|}$.

The extended model is able to describe the near-bottom flow observed in the experiments with beads only qualitatively but it fails in describing the experiments without the beads. We are not too concerned about the relatively poor performance of the model for this case, since it (as mentioned before) does not correspond to a physically realistic flow condition.

Chapter 6

Model for Wave-Current Flows Over Two-dimensional Wave-Generated Ripples

In this chapter the information provided by the experiments is used to develop a model able to describe the wave-current interaction problem in the field. The wave characteristics are assumed to be such that the bottom topography consists of well defined two-dimensional ripples and sediment transport is neglected. The current is incident at an angle ϕ_{wc} with respect to the waves as shown in Figure 6-1 The pure current experiments described in Chapter 3 have shown two important aspects of the near-bottom flow that results when the current is incident at an angle to the ripple crest. First, the flow close to the bottom is turned towards the ripple axis; second , the bottom roughness depends on the angle between the ripple axis and the incident flow. From the analysis of the velocity profiles in the direction perpendicular to the ripple axis it was concluded that the bottom roughness experienced by the flow in this direction is dominated by form drag and does not depend on the angle, whereas the bottom resistance experienced by the flow in the direction parallel to the ripple axis is associated with skin friction. Based on these conclusions, a wave-current boundary layer model is proposed and compared to laboratory and field experiments.

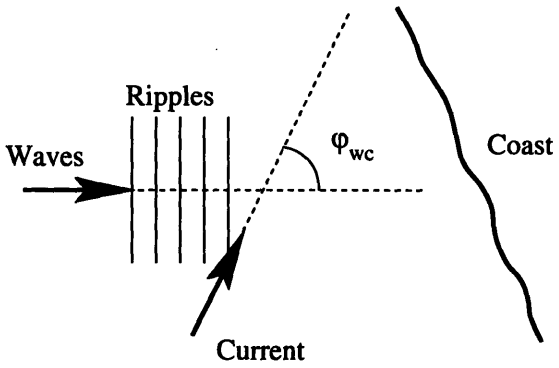

Figure 6-1: Schematic definition of the angle between the direction of the wave propagation and the current.

6.1 Model

The model is basically the wave-current boundary layer model proposed by Grant and Madsen (1979 and 1986) modified to incorporate the effects arising from the current being incident at an angle to the ripple axis. The coordinate system is defined based on the ripple axis and is shown in Figure 6-2, where $\hat{x}_\perp$ is the direction perpendicular to the ripple axis, and $\hat{x}_{||}$ is the direction parallel to the ripple axis. Since it is assumed that waves are responsible for the generation of the bedforms, the waves are in the $\hat{x}_\perp$ - direction and are specified by their equivalent near-bottom orbital velocity, u_b, and a period, $T = 2\pi/\omega$, as suggested by Madsen (1994). The current is driven by a uniform pressure gradient in the $\hat{s}$ - direction defined by the angle ϕ_s measured with respect to the $\hat{x}_\perp$ - direction. The magnitude and direction of the pressure gradient is in principle unknown and is found after solving the problem.

In the Grant-Madsen model, the wave-current interaction takes place inside a thin layer near the bottom defined as the wave boundary layer of thickness δ_{wc}. Above the wave boundary layer, the turbulence is only associated with the current. Assuming the scale of the bottom roughness to be small compared to the boundary layer thickness, the convective acceleration terms in the governing equation can be neglected and the

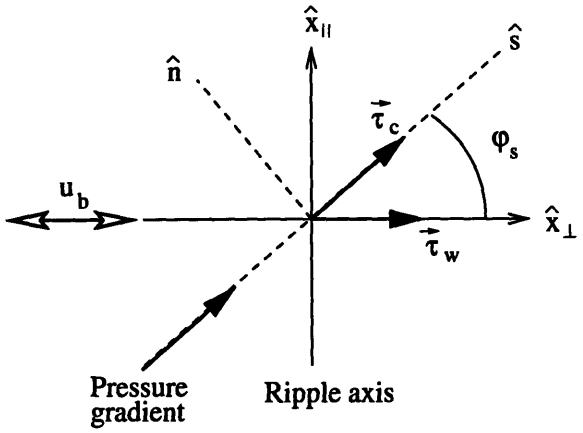

Figure 6-2: Coordinate system definition.

wave-current flow is described by the linearized boundary layer equation. The eddy viscosity is assumed to be time-independent allowing the equation to be separated into an equation that describes the wave motion and another that describes the current. The equation for the wave velocity, u_w, is given by:

$$\frac{\partial u_w}{\partial t} = -\frac{1}{\rho}\frac{\partial p_w}{\partial x_\perp} + \frac{\partial}{\partial z}\frac{\tau_w}{\rho} \tag{6.1}$$

where p_w and τ_w are the time-dependent components of the pressure and shear stress, respectively. Outside the wave boundary layer, the turbulence is associated only with the current, and the wave velocity is assumed to be described by potential theory. In this approximation, the forcing term in the wave equation can be related to the near-bottom velocity predicted by potential theory, $U_b = u_b \cos \omega t$, and Eq. (6.1) becomes:

$$\frac{\partial u_w}{\partial t} = \frac{\partial U_b}{\partial t} + \frac{\partial}{\partial z}\frac{\tau_w}{\rho} \tag{6.2}$$

The equation for the current is:

$$0 = -\frac{1}{\rho}\nabla p_c + \frac{\partial}{\partial z}\frac{\vec{\tau_c}}{\rho} \tag{6.3}$$

where p_c and $\vec{\tau_c}$ are the time-independent components of the pressure and the shear stress. Assuming that the current near the bottom is within the constant stress layer Eq. (6.3) becomes:

$$\frac{\vec{\tau_c}}{\rho} = u_{*s}^2 \, \hat{s} \tag{6.4}$$

where u_{*s} is the shear velocity based on the current bottom shear stress.

The results of the experiments described in Chapter 3 showed that the flow in the direction perpendicular to the ripple axis experienced a roughness different from that experienced by the flow in the parallel direction. Accordingly, the Grant-Madsen model for the flow within the wave boundary layer is modified by assuming that:

i) The perpendicular component of the current shear stress, $\tau_{c\perp} = \rho u_{*s}^2 \cos\phi_s$, interacts with the waves accounting for the presence of the bedforms. The roughness for the waves and the current in this direction are assumed to be given by a drag-form resistance and will be denoted by $z_{o\perp}$.

ii) The parallel component of the current shear stress, $\tau_{c\parallel} = \rho u_{*s}^2 \sin\phi_s$, interacts with the waves as if the bottom were plane. The roughness for the waves and for the current is assumed to be given by skin friction and will be denoted by z_o'.

As a result of the differences in roughness, the parallel component of the current velocity near the bottom will be larger than the perpendicular component, producing the current velocity to be turned towards the ripple axis with respect to the direction defined by the angle ϕ_s.

Inside the wave boundary layer the problem is solved by expressing the shear stress in terms of an eddy viscosity. The eddy viscosity is assumed to be scaled by the shear velocity based on the combined wave-current bottom shear stress. Because the wave-current bottom shear stress is different in each direction, the eddy viscosity representing the shear stress in the perpendicular direction will be different from the one representing the shear stress in the parallel direction. In the direction perpendicular to the ripple axis, the eddy viscosity is denoted by $\nu_{t\perp}$, and the wave and current shear stresses are given by:

$$\frac{\tau_w}{\rho} = \nu_{t\perp} \frac{\partial u_w}{\partial z} \tag{6.5}$$

$$\frac{\tau_{c\perp}}{\rho} = \nu_{t\perp} \frac{\partial u_{c\perp}}{\partial z} \tag{6.6}$$

In the direction parallel to the ripple axis the eddy viscosity is denoted by $\nu_{t\parallel}$ and the current shear stress is expressed as:

$$\frac{\tau_{c\parallel}}{\rho} = \nu_{t\parallel} \frac{\partial u_{c\parallel}}{\partial z} \tag{6.7}$$

The wave-current interaction problem is solved independently for the $\hat{x}_\perp$ and $\hat{x}_\parallel$ - directions. The solution for the current velocity obtained inside the wave boundary layer is then used to specify the boundary condition at δ_{wc}, which is needed to solve for the current velocity outside the wave boundary layer.

6.1.1 The solution inside the wave boundary layer:$z < \delta_{wc}$

Wave-Current interaction perpendicular to the ripple axis:$\hat{x}_\perp$ - direction

The flow in this direction is assumed to be rough turbulent and the bottom roughness $z_{o\perp}$ is assumed to be due to drag- form resistance. The eddy viscosity is assumed to be given by:

$$\nu_{t\perp} = \kappa u_{*wc}\, z \qquad \text{for } z_{o\perp} < z < \delta_{wc} \tag{6.8}$$

where u_{*wc} is the shear velocity based on the maximum bottom shear stress of the combined wave and current flow. Introducing Eqs. (6.8) and (6.5) into (6.2), the equation for the wave velocity:

$$\frac{\partial(u_w - U_b)}{\partial t} = \frac{\partial}{\partial z}\left[\kappa\, u_{*wc}\, z\, \frac{\partial\,(u_w - U_b)}{\partial z}\right] \tag{6.9}$$

and the equation for the current velocity in the perpendicular direction:

$$\kappa\, u_{*wc}\, z\, \frac{\partial u_{c\perp}}{\partial z} = u_{*s}^2 \cos\phi_s \tag{6.10}$$

Eqs. (6.9) and (6.10) with the boundary condition at the bottom:

$$\begin{aligned} u_{c\perp}(z_{o\perp}) &= 0 \\ u_w(z_{o\perp}) &= 0 \end{aligned} \tag{6.11}$$

correspond to the solution of the Grant-Madsen model for the case when the waves and currents are in the same direction. The thickness of the wave boundary layer is defined as $\delta_{wc} = 2\kappa u_{*wc}/\omega$. The wave velocity for $z < \delta_{wc}$ is expressed in terms of the Kelvin functions of order zero:

$$u_w = u_b \, \Re \left[\left(1 - \frac{ker\, 2\sqrt{\zeta} + i\, kei\, 2\sqrt{\zeta}}{ker\, 2\sqrt{\zeta_{o\perp}} + i\, kei\, 2\sqrt{\zeta_{o\perp}}} \right) e^{i\omega t} \right] \tag{6.12}$$

where $\zeta = z\omega/\kappa u_{*wc}$ and $\zeta_{o\perp}$ is the value of ζ at $z = z_{o\perp}$. The current velocity is given by

$$u_{c\perp} = \frac{u_{*s}^2 \cos\phi_s}{\kappa \, u_{*wc}} \ln \frac{z}{z_{o\perp}} \tag{6.13}$$

The solutions in Eqs. (6.12) and (6.13) are expressed in terms of u_{*wc}, which is the shear velocity based on the maximum wave-current bottom shear stress in the perpendicular direction, $\tau_{wc\perp_{max}}$, and is defined as:

$$\tau_{wc\perp_{max}} = \rho \, u_{*wc}^2 = \tau_{w_{max}} + \tau_{c\perp} \tag{6.14}$$

where $\tau_{w_{max}}$ is the maximum wave shear stress at the bottom:

$$\tau_{w_{max}} = \rho \, \kappa \, u_{*wc} \left[z \left| \frac{\partial u_w}{\partial z} \right| \right]_{z=z_{o\perp}} \tag{6.15}$$

Defining $u_{*w} = \sqrt{\tau_{w_{max}}/\rho}$ to be the shear velocity based on the maximum wave shear stress, Eq. (6.14) becomes:

$$u_{*wc} = \sqrt{u_{*w}^2 + u_{*s}^2 \cos\phi_s} = \sqrt{C_\mu} \, u_{*w} \tag{6.16}$$

where C_μ is:

$$C_\mu = 1 + \mu \cos\phi_s \tag{6.17}$$

and

$$\mu = (\frac{u_{*s}}{u_{*w}})^2 \tag{6.18}$$

The maximum wave bottom shear stress can be written as a function of a wave-current friction factor defined as:

$$\tau_{w_{max}} = \rho\, u_{*w}^2 = \rho\, \frac{f_{wc}}{2}\, u_b^2 \tag{6.19}$$

Combining Eqs (6.15) to (6.19) and using the series expansion of the Kelvin functions Madsen (1994) obtained explicit equations to approximate the wave friction factor: For $0.2 < C_\mu u_b/(30\, z_{o\perp}\omega) < 10^2$:

$$f_{wc} = C_\mu \exp\left(7.02 \left(\frac{C_\mu u_b}{30\, z_{o\perp}\omega}\right)^{-0.078} - 8.82\right) \tag{6.20}$$

and for $10^2 < C_\mu u_b/(30\, z_{o\perp}\omega) < 10^4$:

$$f_{wc} = C_\mu \exp\left(5.61 \left(\frac{C_\mu u_b}{30\, z_{o\perp}\omega}\right)^{-0.109} - 7.30\right) \tag{6.21}$$

Wave-current interaction parallel to the ripple axis: $\hat{x}_\parallel$ - direction

In the direction parallel to the ripple axis the bottom roughness experienced by the combined flow is assumed to be given by skin friction. If the flow is rough turbulent the bottom roughness in this direction is $z_o' = d/30$ where d is the diameter of the sediment. If the flow is smooth turbulent, the bottom roughness is $z_o' = \nu/(9u_{*wc}')$, where u_{*wc}' is the shear velocity based on the maximum wave-current bottom shear, $\tau_{wc_{max}}'$. The criterion used to decide whether the flow is rough or smooth turbulent is based on the value of the Reynolds number $Re_*' = k_b u_{*wc}'/\nu$, where $k_b = d$ is the equivalent Nikuradse bottom roughness. If $Re_*' > 3.3$ the flow is assumed to be rough turbulent, otherwise the flow is smooth turbulent. This criterion corresponds to choosing z_o' as the maximum value of $d/30$ and $\nu/(9\, u_{*wc}')$. The maximum wave-

current bottom shear stress, $\tau'_{wc_{max}}$, is defined as:

$$\tau'_{wc_{max}} = \rho\, u'^2_{*wc} = |\tau'_{w_{max}}\, \hat{x}_\perp + \tau_{c\|}\, \hat{x}_\|| \tag{6.22}$$

where $\tau'_{w_{max}}$ is the maximum wave bottom shear stress due to skin friction . The eddy viscosity in the parallel direction $\nu_{t\|}$ is assumed to be given by:

$$\nu_{t\|} = \begin{cases} \kappa u'_{*wc}\, z & \text{for } z'_o < z < \eta \\ \kappa u_{*wc}\, z & \text{for } \eta < z < \delta_{wc} \end{cases} \tag{6.23}$$

where u_{*wc} is the shear velocity based on the maximum wave-current bottom shear stress obtained from the wave-current interaction in the perpendicular direction.

It must be noted that there is, in principle, another length scale to be considered. It is the wave boundary layer thickness that represents the height to which turbulence originating from skin friction diffuses away from the bottom. This wave boundary layer is defined as $\delta'_{wc} = 2\kappa u'_{*wc}/\omega$. Scaling the $\nu_{t\|}$ with u'_{*wc} up to the level defined by the ripple height, is equivalent to assuming the thickness of the wave boundary layer due to skin friction, δ'_{wc}, extends up to $z = \eta$. In principle, this is not necessarily true. For the case when $\delta'_{wc} < \eta$, it is assumed that the shear stress is still represented by u'_{*wc} in the region between $\delta'_{wc} < z < \eta$.

In the region defined by $z'_o < z < \eta$, the wave velocity is denoted by u'_w. The equation that describe the wave velocity in this region of the flow, u'_w, is the same as Eq. (6.9) when u_{*wc}, U_b and u_w are substituted by u'_{*wc}, U'_b and u'_w, respectively. Accordingly, with the definition of $\nu_{t\|}$ in $z'_o < z < \eta$, U'_b is obtained by evaluating the solution for the wave velocity given in Eq. (6.12) at $z = \eta$:

$$U'_b = u'_b \cos(\omega t + \varphi_\eta) = u_b\, \Re\left[\left(1 - \frac{ker\, 2\sqrt{\zeta_\eta} + i\, kei\, 2\sqrt{\zeta_\eta}}{ker\, 2\sqrt{\zeta_{o\perp}} + i\, kei\, 2\sqrt{\zeta_{o\perp}}}\right) e^{i\omega t}\right] \tag{6.24}$$

where $\zeta_\eta = \eta\, \omega/\kappa u_{*wc}$, u'_b and φ_η are the amplitude and the phase of the velocity at $z = \eta$.

The equation for the current in $z'_o < z < \delta_{wc}$ is given by:

$$\nu_{t\|} \frac{\partial u_{c\|}}{\partial z} = u_{*s}^2 \sin\phi_s \tag{6.25}$$

The wave and the current equations are solved using the boundary conditions at the bottom given by:

$$\begin{aligned} u_{c\|}(z'_o) &= 0 \\ u'_w(z'_o) &= 0 \end{aligned} \tag{6.26}$$

The resulting wave and current solutions correspond to those obtained by applying the Grant-Madsen model for the particular case of a current perpendicular to the wave direction. The wave velocity is given by:

$$u'_w = u'_b \, \Re \left[\left(1 - \frac{ker\, 2\sqrt{\zeta'} + i\, kei\, 2\sqrt{\zeta'}}{ker\, 2\sqrt{\zeta'_o} + i\, kei\, 2\sqrt{\zeta'_o}} \right) e^{i\omega t} \right] \tag{6.27}$$

where $\zeta' = z\,\omega/\kappa u'_{*wc}$, ζ'_o is the value of ζ' at $z = z'_o$ and $u'_b = |U'_b|$. The current velocity is:

$$u_{c\|} = \begin{cases} \frac{u_{*s}^2 \sin\phi_s}{\kappa\, u'_{*wc}} \ln\frac{z}{z'_o} & \text{for} \quad z'_o < z < \eta \\ \\ \frac{u_{*s}^2 \sin\phi_s}{\kappa\, u_{*wc}} \ln\frac{z}{z'_{oa\|}} & \text{for} \quad \eta < z < \delta_{wc} \end{cases} \tag{6.28}$$

where $z'_{oa\|}$ is a constant of integration that is obtained by requiring continuity of the current solution at $z = \eta$:

$$z'_{oa\|} = \eta \left(\frac{z'_o}{\eta}\right)^{u_{*wc}/u'_{*wc}} \tag{6.29}$$

The wave and current velocity in Eqs. (6.27) and (6.28) are expressed in terms of the shear velocity, u'_{*wc}. As done for the wave-current interaction in the perpendicular direction, u'_{*wc} is obtained as a function of the maximum wave shear stress, $\tau'_{w_{max}}$, which is related to the wave shear velocity $u'_{*w} = \sqrt{\tau'_{w_{max}}/\rho}$. Using this definition

in Eq. (6.22):

$$u'^2_{*wc} = \sqrt{u'^4_{*w} + u^4_{*s} \sin^2 \phi_s} = C'_\mu \, u'^2_{*w} \tag{6.30}$$

where C'_μ is:

$$C'_\mu = \sqrt{1 + \mu'^2 \sin^2 \phi_s} \tag{6.31}$$

and

$$\mu' = (\frac{u_{*s}}{u'_{*w}})^2 \tag{6.32}$$

The maximum wave bottom shear stress is given by:

$$\tau'_{w_{max}} = \rho \left[\left| \nu_{t\|} \frac{\partial u'_w}{\partial z} \right| \right]_{z=z'_o} \tag{6.33}$$

and can be written as a function of a wave-current friction factor based on skin friction defined as:

$$\tau'_{wmax} = \rho \, u'^2_{*w} = \rho \frac{f'_{wc}}{2} \, u'^2_b \tag{6.34}$$

where f'_{wc} is expressed as in Eqs. (6.20) or (6.21) but replacing $z_{o\perp}$, u_b and C_μ by z'_o, u'_b and C'_μ, respectively.

6.1.2 The solution outside the wave boundary layer: $z > \delta_{wc}$

Outside the wave boundary layer the eddy viscosity is assumed to be:

$$\nu_t = \kappa \, u_{*s} \, z \tag{6.35}$$

and the current shear stress:

$$\frac{\vec{\tau}_c}{\rho} = \nu_t \frac{\partial \vec{u}_c}{\partial z} \tag{6.36}$$

The current velocity $\vec{u}_c$ in the $(\hat{s}, \hat{n})$- coordinate system shown in Figure 6-2:

$$\vec{u}_c = u_s \, \hat{s} + u_n \, \hat{n} \tag{6.37}$$

The solution for the current outside the wave boundary layer is obtained by combining

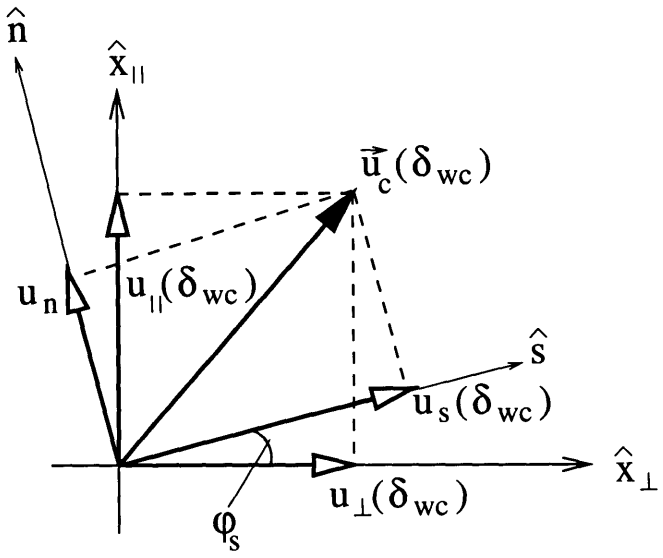

Figure 6-3: The current velocity at $z = \delta_{wc}$

Eqs. (6.37), (6.36), (6.35) and (6.4), and is given by:

$$\begin{aligned} u_s &= \frac{u_{*s}}{\kappa} \ln \frac{z}{z_{os}} \\ u_n &= constant \end{aligned} \tag{6.38}$$

The value of the constants z_{os} and u_n are obtained by requiring the current velocity to be continuous at $z = \delta_{wc}$. The solution for the current velocity in the region $z < \delta_{wc}$ was calculated in the previous section in terms of the perpendicular and parallel components. Relating $u_s(\delta_{wc})$ and u_n to $u_\perp(\delta_{wc})$ and $u_\parallel(\delta_{wc})$ we obtain with the aid of Figure 6-3:

$$\begin{aligned} u_s(\delta_{wc}) &= u_\perp \cos\phi_s + u_\parallel \sin\phi_s = \frac{u_{*s}}{\kappa} \ln \frac{\delta_{wc}}{z_{os}} \\ u_n &= -u_\perp \sin\phi_s + u_\parallel \cos\phi_s \end{aligned} \tag{6.39}$$

with the expression for z_{os}:

$$z_{os} = \delta_{wc}\, exp(-u_s(\delta_{wc})\, \kappa/u_{*s}) \tag{6.40}$$

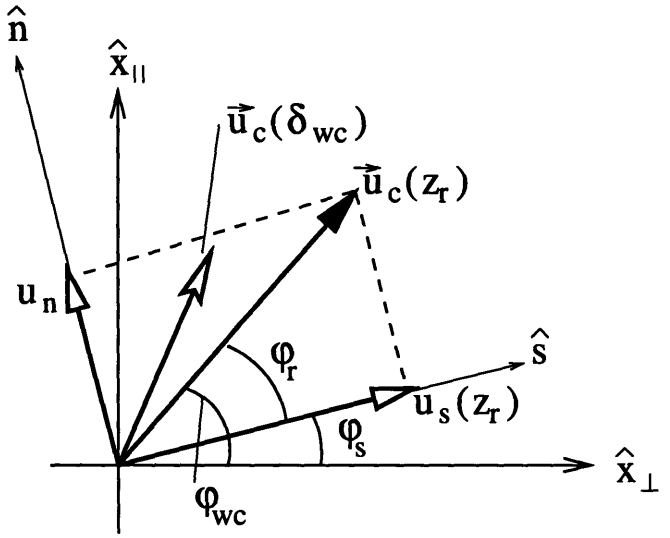

Figure 6-4: The current velocity and the angle ϕ_r at $z_r > \delta_{wc}$

Finally, the current at a given $z = z_r > \delta_{wc}$ is obtained in terms of $(u_s(z_r), u_n)$, as indicated in Figure 6-4:

$$u_c(z_r) \;=\; u_s(z_r)\,\cos\phi_r \;+\; u_n\,\sin\phi_r \tag{6.41}$$

where ϕ_r, the angle between the current at $z = z_r$ and the $\hat{s}$-direction, is given by:

$$\tan\phi_r \;=\; \frac{u_n}{u_s(z_r)} \tag{6.42}$$

As u_n is constant, using the expression for u_s from Eq. (6.38) in Eq. (6.41), the current velocity at a given height can be written as a *'logarithmic'* velocity profile:

$$u_c(z_r) \;=\; \frac{u_{*cr}}{\kappa}\,\ln(\frac{z_r}{z_{oar}}) \tag{6.43}$$

where u_{*cr} and z_{oar} are the current shear velocity and the apparent roughness, and are given by:

$$u_{*cr} \;=\; u_{*s}\,\cos\phi_r \tag{6.44}$$

$$z_{oar} = z_{os}\, exp(-\frac{u_n \kappa}{u_{*s}} \tan\phi_r) \tag{6.45}$$

Eqs. (6.44) and (6.45) show that the local shear velocity and the apparent roughness defined in this manner depend on the height since ϕ_r varies with height. Therefore, the current velocity in Eq. (6.43) can be described only locally by a logarithmic profile.

6.2 Application of the model

To solve the wave-current problem it is assumed that the wave conditions defined by u_b and ω are known. The bottom roughness corresponding to the wave generated ripples, $z_{o\perp}$, is given, or can be determined from empirical relations of ripple geometry . For example, the ripple height, η, and the ripple wavelength, λ, can be estimated knowing the bottom excursion amplitude $A_b = u_b/\omega$, and the sediment diameter d through the ripple classification proposed by Wiberg and Harris (1994). With the knowledge of the ripple geometry the movable bed roughness equation can be used to obtain $z_{o\perp}$. Grant and Madsen (1982) proposed that when sediment transport is negligible the movable bed roughness is expressed as: $k_b \approx 28\ \eta\ (\eta/\lambda)$. Wikramanayake (1993) obtained an expression for the movable bed roughness given by $k_b = 4\,\eta$. Information about the ripple height, η, is also necessary to evaluate the reference velocity, u_b', to be used for the the wave-current problem in the $\hat{x}_{\|}$ - direction, as well as the sediment diameter, d, to estimate z_o'. The current can be specified in two possible ways. One is by giving a reference velocity $u_c(z = z_r)$ and a direction ϕ_{wc} measured at a given elevation, $z = z_r$, above the bottom, where ϕ_{wc} is the angle between the waves and the current as shown in Figure 6-4, *i.e* $\phi_{wc} = \phi_s + \phi_r$. The second way, is the specification of the current through the current shear stress, $\vec{\tau}_c$.

An iteration method is proposed to solve the problem. In the following section the model is compared to laboratory and field experiments. Since in these experiments the information provided for the current is a reference velocity and the angle ϕ_{wc}, the iteration method proposed is based on the knowledge of $u_c(z_r)$ and ϕ_{wc}.

The number of unknowns in the problem can be reduced to four: 1) u_{*wc}, 2) u'_{*wc}, 3) u_{*s} and 4) ϕ_r. The solution of the problem is divided in two parts. In the first part, which is called "Iteration on $u_c(z_r)$", the solution for the waves, *i.e*, u_{*wc} and u'_{*wc} and the shear velocity u_{*s} are calculated. In the second part, the angle ϕ_r is obtained. This part is called "Iteration on ϕ_r".

It is assumed initially that $\phi_r = 0$, *i.e*, $\phi_s = \phi_{wc}$ and u_{*s} is obtained based on the given value of the reference velocity $u_c(z_r)$ as: $u_{*s} = u_c(z_r)\kappa / \ln(z_r/z_{os})$, where z_{os} is an estimate of the apparent roughness which is assumed to be $z_{os} = 10\ \eta/30$, *i.e* larger than $z_{o\perp} = 4\ \eta/30$.

With these assumptions the problem is solved following the steps enumerated below:

6.2.1 Iteration on $u_c(z_r)$

In this part ϕ_s is given and remains constant throughout the iteration. The goal is to obtain u_{*wc} and u'_{*wc}, which are needed to evaluate the parameters to calculate $u_c(z_r)$. The value of $u_c(z_r)$ obtained is compared to the given reference velocity. The process of iteration starts by assuming $\mu = \mu' = 0$:

Solve the wave-current interaction in $\hat{x}_\perp$ - direction:

Knowing u_b, ω and $z_{o\perp}$ obtain u_{*wc}.

i) $C_\mu = 1 + \mu \cos\phi_s$

ii) $f_{wc} = f_{wc}(C_\mu u_b/(z_{o\perp}\omega))$ using Eq. (6.20) or (6.21)

iii) $u_{*w} = \sqrt{f_{wc}/2}\ u_b$

iv) $u_{*wc} = \sqrt{C_\mu}\ u_{*w}$

v) $\delta_{wc} = 2\ \kappa u_{*wc}/\omega$

vi) $u'_b = |u_w(z=\eta)|$ using Eq. (6.12)

Solve the wave-current interaction in the $\hat{x}_\parallel$ - direction:

Knowing u'_b, ω and z'_o obtain u'_{*wc}.

vii) $C_{\mu'} = \sqrt{1 + \mu'^2 \sin^2\phi_s}$

viii) $f'_{wc} = f'_{wc}(C_{\mu'}\ u'_b/(z'_o\omega))$ using Eq. (6.20) or (6.21)

ix) $u'_{*w} = \sqrt{f'_{wc}/2}\, u'_b$

x) $u'_{*wc} = \sqrt{C'_\mu}\, u'_{*w}$

Obtain the current velocity at $z = \delta_{wc}$:

xi) $z'_{oa\|} = \eta\, (z'_o/\eta)^{u_{*wc}/u'_{*wc}}$

xii) $u_\|(\delta_{wc}) = (u^2_{*s} \sin\phi_s)/(\kappa u_{*wc}) \ln(\delta_{wc}/z'_{oa\|})$

xiii) $u_\perp(\delta_{wc}) = (u^2_{*s} \cos\phi_s)/(\kappa u_{*wc}) \ln(\delta_{wc}/z_{o\perp})$

Obtain u_n and z_{os}:

xiv) $u_s(\delta_{wc}) = u_\perp(\delta_{wc}) \cos\phi_s + u_\|(\delta_{wc}) \sin\phi_s$

xv) $u_n = -u_\perp(\delta_{wc}) \sin\phi_s + u_\|(\delta_{wc}) \cos\phi_s$

xvi) $z_{os} = \delta_{wc}\, exp[-u_s(\delta_{wc})\kappa/u_{*s}]$

Obtain the current velocity at $z = z_r$:

xvii) $u_s(z_r) = u_{*s} \ln(z_r/z_{os})/\kappa$

xviii) $u_c(z_r) = \sqrt{u^2_s(z_r) + u^2_n}$

Obtain a new estimate of u_{*s}:

xix) In this part of the solution the comparison between the calculated and given reference velocity is made. If $u_c(z_r)$ calculated in step xviii) is different from the given current velocity $u_{c_{given}}(z_r)$, then a new estimate of u_{*s} is obtained from:

$u_{*s_{new}} = \sqrt{u^2_{c_{given}} - u^2_n}\, \kappa / \ln(z_r/z_{os})$

xx) The value of $u_{*s_{new}}$ is used to obtain new estimates of $\mu = (u_{*s_{new}}/u_{*w})^2$ and $\mu' = (u_{*s_{new}}/u'_{*w})^2$ and return to i).

The steps i) to xx) are repeated with the new values of μ and μ' obtained in xx) until convergence on $u_c(z_r)$ is obtained. At this point the problem has been solved under the assumption that $\phi_s = \phi_{wc}$, *i.e*, ϕ_r =0.

6.2.2 Iteration on ϕ_r

After solving steps i) to xx) the parameters needed to calculate the angle ϕ_r are known, so a new estimate of ϕ_r is obtained as:

xxi) $\phi_{r_{new}} = \tan^{-1}(u_n/u_s(z_r))$

If the value of $\phi_{r_{new}}$ is different from the old value of ϕ_r then ϕ_s is recalculated as:

xxii) $\phi_{s_{new}} = \phi_{wc} - \phi_{r_{new}}$.

The updated ϕ_s is used in part 6.2.1 of the solution. The steps i) to xx) are repeated until $u_c(z_r)$ converges, and ϕ_r is calculated another time in part 6.2.2. The process ends when both values of $u_c(z_r)$, and ϕ_r converge.

In part 6.2.1 of the iteration scheme it was considered that the solution has converged if $u_c(z_r)$ differs from the previous estimate only in the third significant digit. It must be noted that this criterion of convergence is applied to the examples that are considered in the following section, where the specified reference velocity are of the order of $\approx$ 2 to 40 cm/sec.

In part 6.2.2 the criterion of convergence is based on the accuracy of the determination of the angle $\phi_{wc} \pm 5^o$.

In steps vii) to x) the energy friction factor due to skin friction f'_{wc} depends on z'_o. For the cases of smooth turbulent flow, the explicit equation of f'_{wc} in Eq. (6.21) was not applied because $C'_\mu u'_b/(30\ z'_o/\omega)$ was out of the range of validity of the approximation. In this case the implicit equation of f'_{wc} obtained after combining Eqs. (6.27), (6.33) and (6.34) was solved to obtain u'_{*wc}.

6.2.3 Implications of the Model's Predictions

In general, experiments performed in the field consist on measuring the flow velocity in the region close to the bottom. The waves are specified by a representative near-bottom orbital velocity and period, u_b and T, respectively. The current velocity, $u_c(z)$, and the angle between the waves and the current, $\phi_{wc}(z)$, are measured at say four elevations above the bottom. The current is assumed to be logarithmic and the current shear velocity and apparent roughness, u_{*c} and z_{oa}, are obtained by fitting a logarithmic velocity profile to the measurements. If the resulting correlation coefficient is low, or if there is an angular inconsistency throughout the profile , *i.e*, the variability of the angle ϕ_{wc} measured at the different elevation is too large , the data is rejected.

The model predictions of the current velocity in Eq. (6.43) and the angle ϕ_r in

Case	A	B	C	D
u_{*s}	0.5	0.5	1	1
ϕ_s	30	60	30	60
u_n	2.08	2.03	7.52	6.59
z_{os}	1.10	0.16	0.33	0.02
$u_{c_{100}}$	6.05	8.27	16.15	22.45
$u_{*cr_{10}}$	0.40	0.47	0.75	0.92
$u_{*cr_{100}}$	0.47	0.48	0.89	0.96
$z_{oar_{10}}$	0.31	0.09	0.02	0.006
$z_{oar_{100}}$	0.58	0.11	0.07	0.008
$\phi_{r_{10}}$	36.5	21.6	41.4	22.8
$\phi_{r_{100}}$	20.1	14.3	27.7	17.1
R	0.9997	1.0000	0.9997	1.000
u_{*cr_f}	0.44	0.48	0.83	0.94
z_{oar_f}	0.45	0.10	0.04	0.008

Table 6.1: Predicted local current shear velocity, u_{*cr}, apparent roughness , z_{oar}, and angle, ϕ_r, vs. the height above the bottom. The velocities are in (cm/sec), the roughness in (cm) and the angles in (^{o})

Eq. (6.42) imply that u_c might not be exactly logarithmic and that ϕ_{wc} might not be constant. To investigate the implications of the present model for the conventional analysis of field data on near-bottom currents in the presence of waves we consider a wave specified by a representative near-bottom orbital velocity u_b = 15.3 cm/sec and period T=11.2 sec. The bottom topography is characterized by wave-generated ripples of height η = 1.72 cm and the bottom roughness in the perpendicular direction is taken as $z_{o\perp} = 4\eta/30$.The current is specified by the magnitude and direction of the pressure gradient, u_{*s} and ϕ_s, respectively. The model is applied assuming u_{*s} = 0.5 and 1 cm/sec, and $\phi_s = 30^o$ and 60^o. The results obtained after solving the problem under the assumption of smooth turbulent flow are summarized in Table 6.1. The shear velocity and the apparent roughness depend on the height through the angle ϕ_r defined in Eq. (6.42). As an illustration, the shear velocity, u_{*cr}, the apparent roughness, z_{oar}, and the angle, ϕ_r, are evaluated at two different heights above the bottom: z_r = 10 and 100 cm. These values are listed in the table where the subscripts 10 and 100 denote the height z_r at which these values are calculated.

The current shear velocity, the apparent roughness, and the direction of the current show a dependence on the height above the bottom. The predicted profile of $u_c(z)$ in each of the four cases considered, was fitted by a logarithmic profile in the region between 10 cm $< z <$100 cm. Four points were used in the fitting. The resulting shear velocity and roughness obtained from the fitting , u_{*cr_f} and z_{oar_f}, are presented in the last two rows of the table. The corresponding correlation coefficients were $R \approx$ 1.0, indicating that the predicted velocity in the region considered can be regarded as logarithmic. For cases A) and C) the shear velocity calculated at the two elevations differ about 15%, and the difference of the bottom roughness calculated at the two elevations is within a factor of approximately 2 and 3, respectively. This difference is not very important considering that the apparent roughness appears in the expression of the current velocity as an argument in the logarithmic function.

The difference of the angle ϕ_r evaluated at the two elevations , $\Delta\phi_r$, is 16^o, 7^o, 14^o and 6^o, for cases A) to D), respectively. The angle between the wave and the current is $\phi_{wc} = \phi_s + \phi_r$ (Figure 6-4). In the example A) a difference $\Delta\phi_r$ of $\approx 15^o$ indicates a difference $\Delta\phi_{wc}$ of $\approx 15^o$. This difference is bigger than the error in general estimated of $\pm 5^o$ in the determination of ϕ_{wc} in field experiments. This result implies that an angular inconsistency obtained by the instrumentation does not necessarily mean an error in the measurement .

In order to have a better picture of how the predicted current velocity $\vec{u_c}$ depends on the magnitude and direction of the driving pressure gradient, u_{*s} and ϕ_s, Eqs. (6.13) and (6.14) are used in Eq. (6.39) to obtain an expression of u_n as a function of the angle ϕ_s:

$$u_n = \epsilon \frac{u_{*s}}{\kappa} \ln\left(\frac{z_{o\perp}}{z'_{oa\parallel}}\right) \frac{\sin 2\,\phi_s}{2} \tag{6.46}$$

where $\epsilon = u_{*s}/u_{*wc}$, and $z'_{oa\parallel} = \eta\,(z'_o/\eta)^{u_{*wc}/u'_{*wc}}$. Similarly, Eqs. (6.13) and (6.14) are used in Eq. (6.39) to express z_{os} as:

$$z_{os} = \delta_{wc} \left[\frac{z_{o\perp}}{\delta_{wc}} \left(\frac{z'_{oa\parallel}}{z_{o\perp}}\right)^{\sin^2\phi_s}\right]^{\epsilon} \tag{6.47}$$

Eqs. (6.46) and (6.47) show that u_n and z_{os} depend explicitly on $\sin 2\phi_s$ and $\sin^2 \phi_s$, respectively, and they have an implicit dependency on ϕ_s, μ and μ' through the terms u_{*wc} and u'_{*wc}. Let us consider the case in which $\mu \approx \mu' << 1$ then $C_\mu \approx C'_\mu \approx 1$. For this particular wave-dominant case, the shear velocities u_{*wc} and u'_{*wc} are only a function of $z_{o\perp}$, z'_o, u_b and T . In Figure 6-5 a) u_n is plotted as a function of ϕ_s. The parameters ϵ, u_{*s}, $z_{o\perp}$ and $z'_{oa\|}$ used to build the figure correspond to those in example A) presented in Table 6.1.

The normal velocity u_n presents a maximum value of $\epsilon\ (u_{*s}/\kappa)\ \ln(z_{o\perp}/z'_{oa\|})$ at $\phi_s = 45^o$. Because $u_n \propto \sin 2\phi_s$ it is symmetric with respect to an axis passing through $\phi_s = 45^o$. This result implies that examples A) and B) in Table 6.1 correspond to the wave dominated case , $u_n(30^o) \approx u_n(60^o)$.

In Figure 6-5 b) z_{os} depends on ϕ_s as expected. For $\phi_s = 0^o$ z_{os} is maximum and $z_{os} = \delta_{wc}\ (z_{o\perp}/\delta_{wc})^{u_{*s}/u_{*wc}}$, and for $\phi_s = 90^o$, $z_{os} = \delta_{wc}\ (z'_{oa\|}/\delta_{wc})^{u_{*s}/u_{*wc}}$. Using Eq. (6.38) the velocity in the $\hat{s}$-direction can be obtained at the reference elevation z_r = 100 cm as $u_s(z_r) = (u_{*s}/\kappa)\ \ln(z_r/z_{os})$, and the magnitude of the current velocity at z_r is calculated as $u_c(z_r) = \sqrt{u_n^2 + u_s(z_r)^2}$ and plotted in Figure 6-5 c). The dependence of $u_c(z_r)$ on ϕ_s is mostly influenced by the way in which z_{os} depends on ϕ_s.

The ratio between the normal velocity and the current velocity evaluated at z_r = 100 cm , $u_n/u_c(z_r)$ is plotted vs. ϕ_s in Figure 6-5 d). For $\phi_s = 30^o$ the ratio is $u_n/u_c(z_r) = 0.34$, and for $\phi_s = 60^o$ the ratio is $u_n/u_c(z_r) = 0.25$. For a wave dominated environment the ratio $u_n/u_c(z_r)$ depends only on u_{*w} and u'_{*w} which are function of $z_{o\perp}$, z'_o , u_b and T. Therefore, for the parameters considered in the example A): u_b = 15.3 cm/sec, T = 11.2 sec, η = 1.72 cm, the model predicts a component of the velocity in the direction perpendicular to the driving pressure gradient of the order of $u_n \approx 0.3\ u_c$(100 cm) for $\phi_s = 30^o$ to 60^o.

The angle ϕ_r, which represents the direction of the current velocity with respect to the $\hat{s}$ -direction is obtained using Eq. (6.42) at z_r = 10 cm and at z_r = 100 cm above the bottom and is plotted in Figure 6-6 as a function of ϕ_s. The figure shows that the difference between the angle ϕ_r evaluated at the two elevations, i.e $\Delta\phi_{wc}$,

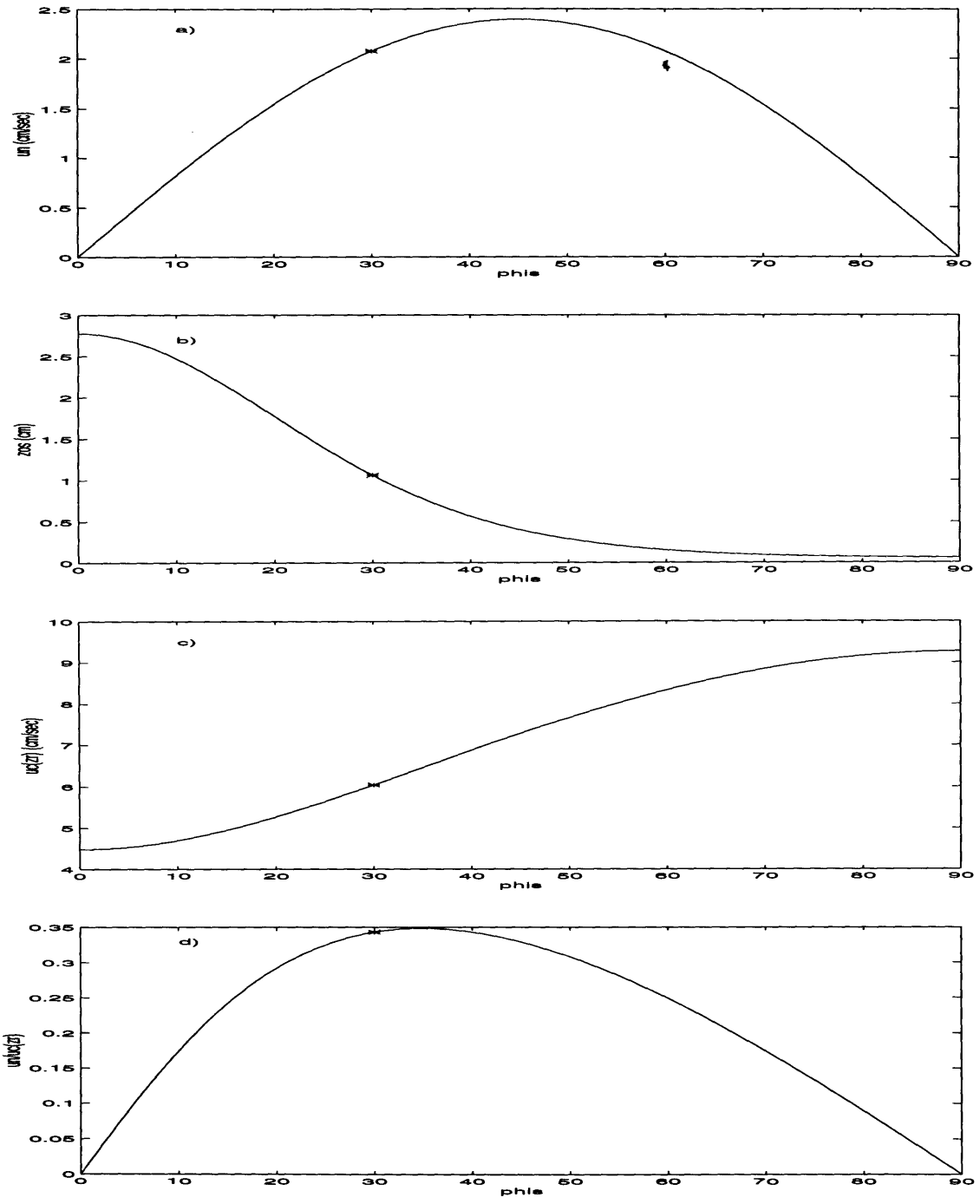

Figure 6-5: Magnitude of the predicted $u_c(z_r)$ vs. ϕ_s at $z_r = 100$ m. a) u_n (Eq. (6.46)). b) z_{os} (Eq. (6.47)) . c) $u_c(z_r)$. d) $u_n/u_c(z_r)$ .The '*' corresponds to case A) presented in Table 6.1

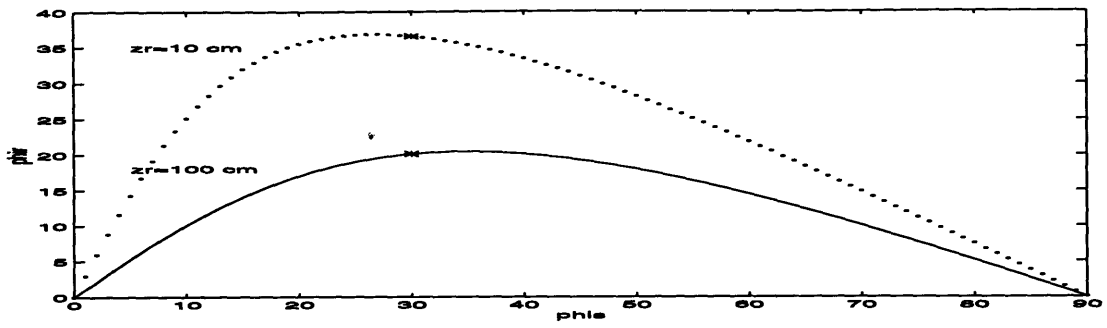

Figure 6-6: Angle ϕ_r at ...: z_r = 10 cm and at - z_r = 100 cm vs. ϕ_s. The '*' corresponds to the case A) presented in Table 6.1.

presents a maximum of $\Delta\phi_{wc} \approx 18^o$ when $\phi_s \approx 20^o$. For the given wave conditions and ripple geometry of example A) the variability of the angle between the waves and current within 1 m above the bottom is expected to be $\Delta\phi_{wc} \approx 15^o$ for $\phi_s = 30^o$ and $\Delta\phi_{wc} \approx 7^o$ for $\phi_s = 60^o$.

6.3 Comparison with experiments

The model described in the previous section is applied to the laboratory measurements performed by Ranasoma and Sleath (1994) and to the field experiments performed by Drake and Cacchione (1992) , Trowbridge and Agrawal (1995) and the field data analyzed by Sorenson (1995).

6.3.1 Laboratory Experiments Ranasoma and Sleath (1994)

When the angle between the waves and the current is $\phi_{wc} = 90^o$, the proposed model predicts that there is no wave-current interaction in the direction perpendicular to the ripple axis. The interaction takes place in the direction parallel to the ripple axis through the maximum wave-current skin friction bottom shear stress, $\tau'_{wc_{max}}$ in Eq. (6.22). To test this assumption the model predictions are compared to the laboratory experiments performed by Ranasoma and Sleath (1994).

The oscillatory flow in these experiments was generated by oscillating a tray in the

direction perpendicular to the steady flow. The ripples were produced by covering the tray with sand of a mean diameter $d = 0.04$ cm and oscillating the tray, without the current superimposed, with a given amplitude a and period T. After the ripples were formed, they were stabilized by spreading a thin layer of cement over them. Two sets of ripple bedforms were used in the experiments. The ripples of bed 1 were produced when the amplitude and period of oscillation were $a = 7.8$ cm and $T = 2.45$ sec, and they were characterized by a height $\eta = 1.84$ cm and a wavelength of $\lambda = 10$ cm. The ripples of bed 2 were originated by oscillating the tray with $a = 4$ cm and $T = 1.25$ sec, and their resulting geometry was $\eta = 0.91$ cm and $\lambda = 5$ cm. Velocity measurements were made at 11 equally spaced points from ripple trough to trough. The spatial average velocity of the mean current was represented by the theoretical expression proposed by Sleath (1991). In Sleath's model the eddy viscosity is represented by the sum of two terms. The one associated with the waves is assumed to be constant and the one associated with the current is assumed to depend linearly on the height above the bottom. As a result of these assumptions, the solution for the current velocity is given by:

$$u = \frac{u_{*RS}}{\kappa} \ln\left(\frac{z + z_s}{z_a}\right) \tag{6.48}$$

with the constant z_s given by:

$$z_s = 0.0063\ k_s \frac{U_o}{u_{*RS}}\ \left(\frac{a}{k_s}\right)^{1/2} \tag{6.49}$$

where U_o is the amplitude of the tray velocity, k_s is the equivalent bottom roughness and is assumed to be $k_s = 4\eta$, and u_{*RS} is the shear velocity based on the bottom current shear stress.

The parameter z_a is defined as $z_a = z_s + k_s/30$ if the flow is assumed to be rough turbulent. If the flow is smooth turbulent, z_a is obtained by assuming that the velocity in Eq (6.48) must be equal to the velocity inside the viscous sublayer at the matching level of these two regions, given by the thickness of the viscous sublayer: $\delta_\nu = 11.6\nu/\overline{u_{*rms}}$. In this definition the shear velocity u_{*rms} represents the mean turbulence intensity averaged over half a wave cycle. The expression for z_a is given

by:

$$z_a = \left(z_s + \frac{105 z_{os}}{C}\right) \exp\left(\frac{-4.64}{C}\right) \tag{6.50}$$

where

$$z_{os} = \nu/(9.05 u_{*RS}) \tag{6.51}$$

and

$$C = \left(1 + \left(0.017 \left(\frac{U_o}{u_{*RS}}\right)^2 \left(\frac{a}{k_s}\right)^{-1/4}\right)^2\right)^{1/4} \tag{6.52}$$

Several experiments are reported by Ranasoma and Sleath for both bedform geometries. In Table 2 of their paper the test conditions: T and a, are listed, as well as the value of u_{*RS} obtained by a least squares fit to the measured velocity. The model proposed in this chapter is applied to 6 of the experiments presented in the paper. Except for the case of the test 109, for which the experimental velocity profile is shown in figure 4 of the paper, the rest of the examples used in the comparison were randomly chosen.

The period T and the amplitude of the tray velocity $U_o = a\ 2\ \pi/T$ are used to specify the waves. The bottom roughness in the perpendicular direction is estimated based on the ripple geometry information as $z_{o\perp} = 4\ \eta/30$. The roughness used to solve the wave-current problem in the $\hat{x}_{||}$ - direction is $z'_o = d/30$, *i.e*, the flow is assumed to be rough turbulent in this direction because $u'_{*wc}\ d/\nu > 3.3$.

In order to apply the model the current reference velocity is obtained by using the theoretical expression in Eq (6.48) evaluated at $z_r = 10$ cm. For this purpose, the parameter z_a has to be calculated. Two possible expressions are given for z_a depending on the flow being smooth or rough turbulent. Based on the information presented in the paper, it is inferred that the criterion used by the authors to decide whether the flow is smooth or rough turbulent is based on the Reynolds number scaled by 2 times the sand diameter, *i.e.*, $Re = 2\ d\ u_{*RS}/\nu$. The range of Re for which the flow is considered to be smooth turbulent seems to be $Re < 7$ or a slightly larger number.

The input parameters to the model are summarized in Table 6.2. In the last

Test	a (cm)	T (sec)	U_o (cm/sec)	$u_c(z_r)$ (cm/sec)	η (cm)	u_{*cr} (cm/sec)	z_{oar} (cm)	u_{*RS} (cm/sec)	Re
109	4.0	1.8	14.2	5.3	0.91	0.46	0.10	0.53	3.8
114	4.0	2.5	10.3	13.7	0.91	0.78	0.01	0.88	6.1
115	4.0	1.3	20.1	21.6	0.91	1.32	0.01	1.47	11.4
18	7.8	1.8	27.5	4.7	1.84	0.55	0.34	0.69	6.4
22	7.8	2.4	20.5	16.1	1.84	1.08	0.03	1.32	11.5
+23	7.8	2.4	20.3	13.8	1.84	0.97	0.04	2.05	18.9
23				32.7		1.74	0.05		

Table 6.2: Model predictions and comparison with Ranasoma and Sleath (1994). u_{*cr} and z_{oar} are the current shear velocity predicted by the model. u_{*RS} is the current shear velocity obtained in the experiments and $Re = 2du_{*RS}/\nu$

column of the table $Re = 2\ d\ u_{*RS}/\nu$ is presented. Assuming that the criterion of flow condition classification used in the Ranasoma and Sleath's paper is $Re < 7$, then only Test 109, 18 and 22 correspond to the case of smooth turbulent flow. Tests number 114 and 22 have a $Re \approx 11$, *i.e.*, they have $d\ u_{*RS}/\nu \approx 6.5$ close to the limit of the smooth turbulent flow classification (Schlichting, 1968). For these tests the reference velocity was calculated assuming that the flow was smooth turbulent and z_a was obtained by using Eqs. (6.50) to (6.52).

In Figure 6-7 (a) the experimental velocity profile for the test 109 of Ranasoma and Sleath (1994) is represented by 'o'. The solid line corresponds to the predicted velocity obtained after applying the present model. The dotted line is the theoretical expression proposed by Sleath, Eq. (6.48). For this particular test, the present model is able to predict the measurements.

The other examples listed in Table 6.2 were compared with the predicted velocity by using the theoretical expression given by Eq. (6.48). The comparison between test 114, 115, 18 and 22 are shown in Figure 6-7 (b) to (e), respectively. The predicted profiles are in agreement with the velocity obtained using Eq. (6.48).

The last 2 rows of the Table 6.2 correspond to the experiment 23. The value of $Re = 19$ in Test 23 is high enough to consider the flow to be out of the smooth turbulent region. In the row marked with a '+' the reference velocity $u_c(z_r) = 32.7$ cm/sec

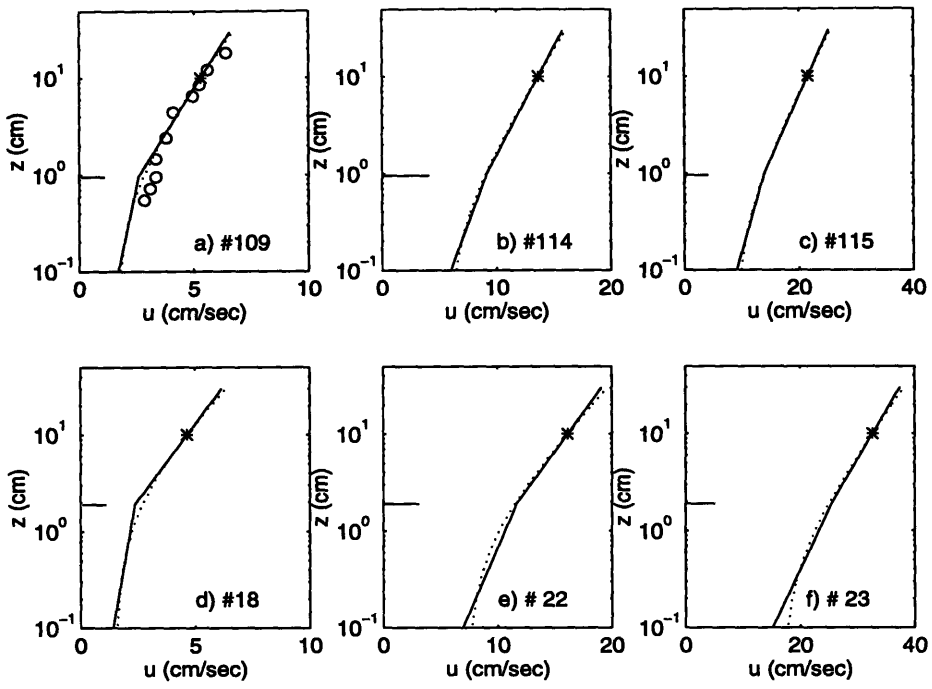

Figure 6-7: Model predictions and comparison with the experimental work of Ranasoma and Sleath (1994).*: reference velocity o:experimental points ....:predicted velocity given in Eq (6.48) –:present model prediction.

was obtained assuming that the flow was smooth turbulent. Using this reference velocity in the present model, the predicted shear velocity u_{*cr} is in agreement with the measured shear velocity, u_{*RS}. The agreement is also observed in the profile plotted in Figure 6-7 (f).

The model was also applied to Test 23 using the reference velocity obtained under the assumption of rough turbulent flow, $u_c(z_r) = 13.8$ cm/sec. In this case the velocity profile predicted by the present model does not agree with the velocity described by Eq. (6.48). The corresponding plot is not presented, but the disagreement is reflected in the predicted shear velocity u_{*cr} listed in the last row of the table. The values of the reference velocity obtained for Test 23 by using Sleath's equations under the assumption of smooth turbulent flow is $u_c(z_r)$=32.7 cm/sec, and the one obtained under the assumption of rough turbulent flow is $u_c(z_r) = 13.8$ cm/sec. The difference between the predicted references velocities is surprisingly large. The reference velocity was calculated for other tests presented in the paper for which the Reynolds number

was close to the inferred transition region. The difference in the predicted reference velocity under the assumption of smooth turbulent flow was unexpectedly larger than the one obtained under the assumption of rough turbulent flow.

Due to the uncertainty in the criterion used to define whether the flow is smooth or rough turbulent, it is concluded that the only truly valid comparison is the one corresponding to test 109 for which the experimental velocity profile is presented in the publication of Ranasoma and Sleath. The agreement between the experiment 109 and the prediction supports the assumptions made in the model for the particular case of a current perpendicular to the wave direction.

6.3.2 Field Data from Duck.

Sorenson (1995), analyzed the data acquired by four electromagnetic current meters placed on a tetrapod located on a 20 m isobath off Duck, North Carolina. The shore-normal and shore-parallel velocity components were measured at four elevations, between 5 cm and 100 cm above the bottom. The measured time series were analyzed to obtain the current velocity, u_c, and direction, ϕ_c, as well as the representative near-bottom orbital velocity, u_b, the representative wave frequency, ω, and wave direction, ϕ_w. Using ϕ_c and ϕ_w, the acute angle between the waves and current ϕ_{wc} was obtained. The bedform geometry was estimated based on the mean sediment diameter, $d = 0.018$ cm, and the wave characteristics u_b and ω by applying the model of ripple geometry proposed by Wiberg and Harris (1994). The bursts presented in Sorenson (1995) number 115 to 125, and 127 are used in this section to compare with the predictions of the model. The inputs to the model are the period T, the near-bottom orbital velocity u_b, the ripple height η, the bottom roughness in the perpendicular direction, $z_{o\perp} = 4\,\eta/30$, the sediment diameter d, the current reference velocity at $z_r = 100$ cm, u_{cr}, and the angle between the wave and the current ϕ_{wc}. These parameters are listed in the first five columns of Table 6.3. The wave-current interaction problem was solved following the procedure described in the previous section. The predicted angle ϕ_s, the current shear velocity based on the current shear stress u_{*s}, the current shear velocity velocity u_{*cr} (Eq. (6.44)) and apparent rough-

Burst	T (sec)	u_b (cm/sec)	$u_c(z_r)$ (cm/sec)	η (cm)	ϕ_{wc}	ϕ_s	u_{*s} (cm/sec)	u_{*cr} (cm/sec)	z_{oar} (cm)	U_{*c} (cm/sec)	Z_{oa} (cm)
+115	13.3	14.6	12.2	1.42	68.4	48.0	0.70	0.66	0.06	0.83	0.29
+116	13.0	17.3	2.6	0.99	9.0	5.7	0.30	0.30	3.18	0.25	1.68
+117	12.2	18.3	4.2	1.02	59.0	45.3	0.35	0.34	0.78	0.43	2.11
+118	11.8	16.6	11.4	1.40	54.8	31.0	0.80	0.73	0.19	0.90	0.78
*119	11.3	15.0	13.4	1.74	28.5	10.0	1.17	1.11	0.79	1.08	0.78
120	11.2	15.3	22.8	1.72	37.4	12.3	1.69	1.53	0.26	1.48	0.23
121	9.5	17.1	36.6	1.82	77.9	61.0	1.49	1.43	0.003	2.23	0.15
+122	10.7	18.5	37.6	1.39	76.0	57.8	1.57	1.49	0.004	1.90	0.04
123	9.8	16.0	25.6	1.89	85.7	79.5	1.06	1.06	0.006	1.11	0.01
124	9.4	14.4	9.4	2.06	65.0	44.8	0.61	0.57	0.13	0.63	0.31
125	9.2	13.9	3.7	2.09	80.4	75.1	0.27	0.27	0.44	0.26	0.16
127	9.7	12.4	8.5	2.11	7.8	2.8	0.86	0.86	1.74	0.46	0.07

Table 6.3: Model predictions and comparison with the field data from Duck,Sorenson (1995)

ness z_{oar} (Eq. (6.45)) are listed in Table 6.3. The last two columns presented in the Table correspond to the values of the current shear velocity, U_{*c}, and , the apparent roughness, Z_{oa} obtained by fitting a logarithmic velocity profile to the measurements of the magnitude of u_c.

After solving the problem for the cases of bursts 115, 116, 117, 118 and 122, it was found that the wave boundary layer thickness $\delta'_{wc} > \eta$. This contradicts the assumption involved in the definition of the eddy viscosity in the $\hat{x}_{||}$ - direction, Eq. (6.23). These examples are marked with a '+' in Table 6.3 and their predicted $\delta'_{wc} \approx 1.1\eta$ to 1.6η. For these cases the model can be modified by assuming that the eddy viscosity $\nu_{t||}$ is given by:

$$\nu_{t||} = \begin{cases} \kappa u'_{*wc}\, z & \text{for } z'_o < z < \delta'_{wc} \\ \kappa u_{*wc}\, z & \text{for } \delta'_{wc} < z < \delta_{wc} \end{cases} \tag{6.53}$$

Because the values of δ'_{wc} are slightly larger than η it is expected that the predictions of u_{*cr} and z_{oar} obtained by applying the model with $\nu_{t||}$ given by Eq. (6.53) will not be significantly different from those values presented in Table 6.3.

For the burst 119, marked with '*' in the table, no convergence in ϕ_r was obtained

by applying the iteration method described in the previous section if $\phi_r = 0$ was used as an initial guess. However a converged solution could be obtained if the value $\phi_{wc} = 33^o$ was used as an input, instead of the measured value $\phi_{wc} = 28.5^o$. This converged solution predicts that $\phi_r = 20.7^o$. The problem then was solved another time using the measured value $\phi_{wc} = 28.5^o$ as an input, but now with the value of $\phi_r = 20.7^o$ obtained in the previous calculation as an initial guess. In this case, the iterative method converged to a solution with the value $\phi_r = 18.50^o$.

This example illustrates that a good initial guess is sometimes required for the iteration method to converge properly. In this example, it was possible to obtain a converged solution only by first obtaining a better initial guess by running the iteration program with a modified input variable. This implies that there are cases where a solution exists but cannot be found at the first pass through the iteration method.

As an independent check, solutions were found using a standard multidimensional Newton-Raphson subroutine (Press *et al*, 1992) that solves an arbitrary system of N nonlinear equations with N unknowns. The solution obtained with this subroutine was found to be in perfect agreement with the one obtained by the proposed iteration method.

In Figure 6-8 (a), the predicted and experimental shear velocities are compared graphically. The predicted values of the shear velocity, u_{*cr}, are indicated by '*' and the measured, U_{*c}, by 'o'. The dotted lines represent the error interval based on the standard deviation of U_{*c}. The predicted shear velocities, u_{*cr} , show good agreement with the experimental shear velocity except for the cases of the bursts 121 and 122 where the theoretical shear velocity is smaller by a factor of ≈ 0.7 relative to the experimental values. The predicted apparent roughness, z_{oar}, is compared with the experimental apparent roughness, Z_{oa}, in a semilog-plot in Figure 6-8 (b). The predicted values are indicated by '*' and the experimental by 'o'. The dotted lines represent the error interval based on the standard deviation of $\ln Z_{oa}$. The agreement observed in the roughness is not as good as the one observed in the shear velocities. The predicted apparent roughness is smaller by $\approx$ an order of magnitude

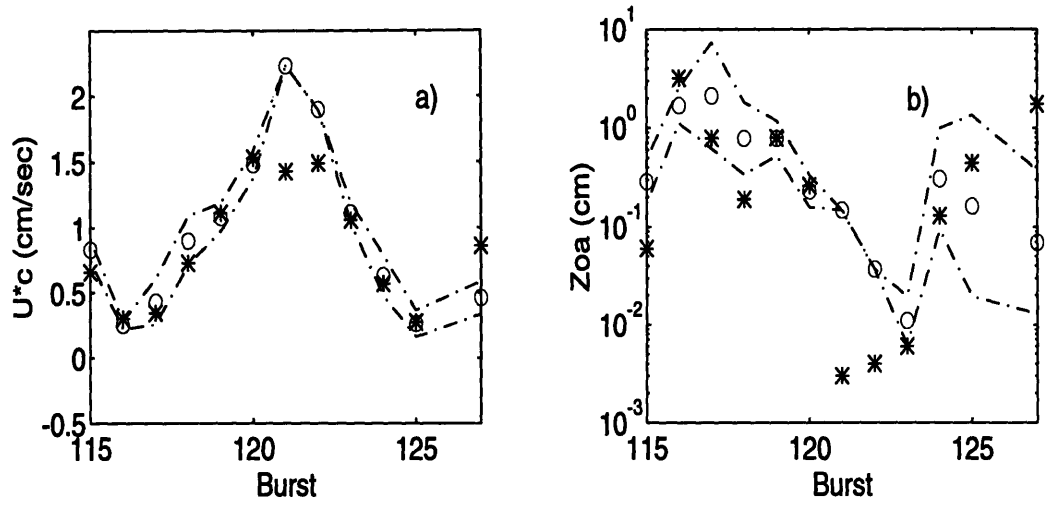

Figure 6-8: Model prediction and comparison with the field data of Duck. a) Current shear velocity b) apparent bottom roughness

for the cases of the bursts 115 and 122, and, by two order of magnitude for the case of burst 121. The predicted roughness for the burst 127 is bigger than the measured by two orders of magnitude. The disagreement between the predicted and measured apparent roughness becomes relatively smaller since z_{oa} is the argument of the logarithmic function.

Clearly, there is some disagreement between the predicted and the experimental shear velocity and apparent roughness. However, the proposed model still provides a qualitative description of the effect of the angle between the wave and the currents on the near-bottom flow.

Let us consider the cases of burst 120 and 123. These two bursts have similar characteristics. Their waves are represented by a period of $T \approx 10$ to 11 sec and their near-bottom orbital velocity by $u_b \approx 15$ to 16 cm/sec. The current reference velocity is $u_c(z_r) \approx 23$ to 26 cm/sec, and the ripple height $\eta \approx 1.7$ to 1.9 cm. The main difference between these two cases is the angle between the wave and the current: $\phi_{wc} = 37^o$ and 80^o, respectively. The experimental current shear velocity and apparent roughness listed in Table 6.1 is $U_{*c} = 1.5$ cm/sec and $Z_{oa} = 0.2$ cm for burst

120 for which $\phi_{wc} = 37^o$. For burst 123, $U_{*c} = 1.1$ cm/sec and $Z_{oa} = 0.01$ cm. This experiment has a $\phi_{wc} = 80^o$. A decrease in the current shear velocity and the apparent roughness observed in burst 123 with respect to burst 120 can be explained by the difference in angle between the waves and the current.

The conventional Grant-Madsen model (1986) was applied to bursts 120 and 123, using the same inputs as the one used in the model described in this chapter: u_b, T, $u_c(z_r)$ and the single-valued bottom roughness obtained as $z_{o\perp} = 4\eta/30$. The predicted current shear velocity and apparent roughness obtained for burst 120 were $u_{*c_{GM}} = 1.99$ cm/sec and $z_{oa_{GM}} = 1.02$ cm, and for burst 123, the predicted values were $u_{*c_{GM}} = 2.15$ cm/sec and $z_{oa_{GM}} = 0.81$ cm. The results obtained by using the Grant-Madsen model overpredict the experimental shear velocity and apparent roughness. In addition, the estimated apparent roughness are of the same order in both experiments and no angle dependence is predicted. These results are expected because the parameters used in the model to solve the problem for the two examples are of the same order, and, because the angle dependence in the formulation is given by a $\mu \cos\phi_{wc}$ in the C_μ term. On the other hand, the predicted roughness obtained by applying the proposed model are $z_{oar} = 0.26$ cm for Burst 120, and $z_{oar} = 0.006$ cm for Burst 123. The proposed model is able to reproduce the angle dependence observed in the experiments.

The ability of the proposed model to reproduce the angle dependence of the apparent roughness is based on the addition of a near-bottom velocity component parallel to the ripple axis.

6.3.3 Field Experiments Drake and Cacchione (1992)

The model was also tested against the field experiments performed by Drake and Cacchione (1992) on the inner shelf in northern California. Velocity measurements were obtained with two -axes electromagnetic current sensors at three heights within 1 m above the bottom. During the period of the experiments the bottom topography consisted of two set of ripples. The larger set of ripples, had an average wavelength of $\lambda = 26$ cm, and an average height of $\eta = 3.5$ cm. The second set of ripples

Test	T (sec)	u_b (cm/sec)	$u_c(z_r)$ (cm/sec	η (cm)	ϕ_{wc}	ϕ_s	u_{*s} (cm/sec)	u_{*cr} (cm/sec)	z_{oar} (cm)	U_{*c} (cm/sec)	Z_{oa} (cm)
2	12.4	13.1	8.2	3.5	85.0	79.6	0.47	0.46	0.09	0.69	0.98
1	11.9	11.5	7.7	3.5	72.0	55.0	0.47	0.45	0.11	0.71	1.41
4	12.8	13.8	9.3	3.5	68.0	46.3	0.59	0.55	0.12	0.83	1.17
13	11.9	11.4	7.5	3.5	58.0	34.6	0.54	0.50	0.24	0.66	1.12
12	13.2	10.0	8.0	3.5	55.0	29.9	0.58	0.52	0.23	0.71	1.16
9	11.6	10.7	8.3	3.5	48.0	23.4	0.65	0.59	0.38	0.77	1.50

Table 6.4: Model predictions and comparison with Drake and Cacchione (1992). The roughness in the parallel direction is $z_o' = \nu/(9u_{*wc}')$

were developed within the troughs of the larger ripples. They were characterized by a wavelength of approximately 8 to 12 cm and a height of 1 cm. The sediment diameter was d= 0.025 cm and suspended sand concentration was found to be negligible.

The model was applied to 6 (randomly chosen) of the 23 experiments reported by Drake and Cacchione. Assuming that the dissipation due to form drag is associated with the largest ripples, the roughness in the perpendicular direction was obtained as $z_{o\perp} \approx \eta\ (\eta/\lambda) \approx 0.43$ cm, which is approximately the value obtained by using $z_{o\perp} = 4\eta/30 = 0.47$ cm. The input used are u_b, T, $z_{o\perp} = 0.43$ cm, the current velocity $u_c(z_r)$ specified at $z_r = 1$ m, the angle between the waves and the current ϕ_{wc}, and the ripple height $\eta = 3.5$ cm. These parameters are shown in the first 5 columns of Table 6.4. The estimated values of the angle ϕ_s, the shear velocity based on the current shear stress u_{*s}, the current shear velocity u_{*cr} and the apparent roughness z_{oar} obtained by applying the model are presented in Table 6.4. The last two columns of this table correspond to the experimental current shear velocity U_{*c} and apparent roughness Z_{oa} obtained by fitting a logarithmic profile through the three measurements. The predicted shear velocity $u_{*cr} \approx 0.5$ cm/sec is lower than the one observed experimentally which is of the order of $U_{*c} \approx 0.7$ cm/sec. The predicted apparent roughness z_{oa} also underestimates the value of Z_{oa} by approximately an order of magnitude.

The model is not able to predict these set of experiments quantitatively. Qualitatively, the predicted apparent roughness show the angle dependence observed in the experiments, the smaller roughness corresponds to the larger ϕ_{wc}. From the descrip-

Test	T (sec)	u_b (cm/sec)	$u_c(z_r)$ (cm/sec	η (cm)	ϕ_{wc}	ϕ_s	u_{*s} (cm/sec)	u_{*cr} (cm/sec)	z_{oar} (cm)	U_{*c} (cm/sec)	Z_{oa} (cm)
2	12.4	13.1	8.2	3.5	85.0	84.1	0.77	0.77	1.47	0.69	0.98
1	11.9	11.5	7.7	3.5	72.0	69.2	0.72	0.72	1.42	0.71	1.41
4	12.8	13.8	9.3	3.5	68.0	64.2	0.89	0.89	1.51	0.83	1.17
13	11.9	11.4	7.5	3.5	58.0	53.7	0.73	0.72	1.61	0.66	1.12
12	13.2	10.0	8.0	3.5	55.0	50.0	0.75	0.74	1.42	0.71	1.16
9	11.6	10.7	8.3	3.5	48.0	42.9	0.79	0.79	1.55	0.77	1.50

Table 6.5: Model predictions and comparison with Drake and Cacchione (1992) using $z_o' = 4/30$ cm scaled with the height of the small set of ripples

tion presented in the paper the origin of the small ripples located between the troughs of the larger ripples is not clear. The Shields parameter based on the maximum wave shear stress and the mean sand diameter was estimated to be smaller than the critical Shields parameter for sediment motion. This result indicates that the largest ripples might not have been active. In addition a photograph of the bottom topography, Figure 2 in the paper, shows that the small ripples were not aligned with the crests of the larger ripples. The presence of the small ripples represent an increase in the bottom roughness experienced by the flow component in the direction parallel to the crests of the larger set of ripples . It was decided to apply the model with the same input parameters as those used to obtain the results presented in Table 6.4, but with the bottom roughness for the flow in the parallel direction assumed to be scaled by the height of the small ripples, $z_o' = 4\,\eta_{small}/30 = 4/30$ cm rather than the sediment grain size. In Table 6.5 the results obtained by increasing the roughness in the parallel direction show a marked improvement in the predictions. The current shear stress is $u_{*cr} \approx 0.75$ cm/sec, and the apparent roughness $z_{oar} \approx 1.5$ cm. These values are of the same order as those obtained in the experiments. Comparing the results presented in Tables 6.4 and 6.5, it is observed that the angle ϕ_s is bigger and closer to the angle ϕ_{wc} for the case of larger z_o'. This is a consequence of a reduction in the parallel component of the velocity due to a larger roughness in that direction.

6.3.4 Field Experiments Trowbridge and Agrawal (1995)

The field experiments performed by Trowbridge and Agrawal (1995) at Duck, North Carolina were used to test the model. The results of two experiments , called Glimpse 1 and Glimpse 2, are reported in their paper. Problems with the instrumentation did not allow the measurements of the two components of the velocity during Glimpse 2, therefore only Glimpse 1 is consider to test the model. The velocity was measured at 4 elevations within 15 cm above the bottom with a laser Doppler velocimeter. During the period of the measurements corresponding to Glimpse 1 it was observed that wave-generated ripples with a wavelength $\lambda \approx 10$ cm were formed with the crests placed perpendicular to the direction of wave propagation. The bottom consisted of sand grains of diameter $d = 0.02$ cm.

The angle between the waves and the current was $\phi_{wc} = 70^o$, the waves were specified by a representative near-bottom orbital velocity $u_b = 15.8$ cm/sec and period $T = 9.1$ sec. The measurements of the wave amplitude and phase profiles were analyzed based on the Grant-Madsen model (1986) to obtain the the wave-current shear velocity, $u_{*wc} = 2.31$ cm/sec, and the bottom roughness , $z_{o\perp} = 0.044$ cm. From the analysis of the current velocity outside the wave boundary layer the current shear velocity was estimated $U_{*c} = 0.99$ cm/sec, and the resulting apparent roughness was $Z_{oa} = 0.56$ cm. These values are listed in the last 2 columns of Table 6.6.

To test the present model it was assumed that the bottom roughness was the one estimated by Trowbridge and Agrawal, $z_{o\perp} = 0.044$ c. The ripple height was calculated using the movable bottom roughness equation proposed by Grant and Madsen (1982): $\eta = 0.7$ cm. The waves were specified by u_b and T and the current reference velocity was assumed to be the velocity measured at the highest elevation z_r = 14.5 cm, $u_c(z_r) = 7.7$ cm/sec. The predicted current shear velocity and apparent roughness, u_{*cr} and z_{oar}, obtained after applying the model are listed in Table 6.6 . The predicted current shear velocity $u_{*cr} = 0.6$ cm/sec is smaller than the measured value $U_{*c} = 0.99$ cm/sec. Similarly, the predicted bottom roughness $z_{oar} = 0.08$ cm underpredicts the experimental value $Z_{oa} = 0.5$ cm. Although the model is not

T (sec)	u_b (cm/sec)	$u_c(z_r)$ (cm/sec	η (cm)	ϕ_{wc}	ϕ_s	u_{*s} (cm/sec)	u_{*cr} (cm/sec)	z_{oar} (cm)	U_{*c} (cm/sec)	Z_{oa} (cm)
9.1	15.8	7.7	0.7	70	51.9	0.62	0.59	0.08	0.99	0.5

Table 6.6: Model predictions and comparison with Trowbridge and Agrawal (1995)

able to reproduce the observations presented by Trowbridge and Agrawal (1995), the agreement obtained between the result of the model and the available experimental set of data is encouraging. Based on the results obtained from the data presented by Sorenson (1995) good agreement beween the predicted and experimental shear velocity was obtained in 9 cases out of 12 of the experiments analyzed. The most remarkable feature of the model is its ability to reproduce the angle dependence of the bottom roughness observed in the experiments.

Chapter 7

Conclusions

The purpose of this thesis has been to understand the nature of the near-bottom flow produced under the combined effect of waves and current for the most general situation where the current is incident at an angle to the waves. Because of the constraints of the experimental setup, this problem was investigated experimentally in a situation where both waves and currents are incident at the same angle to two-dimensional artificial bottom roughness elements that simulate the wave-generated ripples. The wave-current experiments performed deviate from the real situation in the field where only the current is incident at an angle and the waves are perpendicular to the ripples. Despite this limitation, the experimental results have yielded major physical insights into the characteristics of the near-bottom flow that results from the ripples being oriented with their axis at an angle to the incident flow. These results provided the basis for the development of a general model capable of predicting this flow quantitatively in the limited set of field experiments available.

7.1 Summary of Experimental Results

7.1.1 Pure Wave Experiments

Velocity measurements were performed for ripples placed at a 45^o angle to the incident wave. This first series of experiment led to the following conclusions:

1) The velocity measurements presented in Chapter 3 show that there is a remarkable difference between the profiles that describe the wave amplitude and the phase of the components of the flow in the direction perpendicular and parallel to the ripple axis. In the direction perpendicular to the ripple axis, a large wave boundary layer thickness was observed in the profiles. This enhanced wave boundary layer indicates larger turbulence intensities, and therefore a larger bottom roughness. On the other hand, the flow in the direction parallel to the ripple axis exhibits a much thinner wave boundary layer indicating that the bottom roughness experienced by the flow in this direction is smaller than the one experienced by the component of the flow in the direction perpendicular to the ripple axis.

2) Pure wave energy dissipation measurements were performed when the waves were propagating over the rippled bed for $\theta = 0^o, 30^o, 45^o$ and 60^o. The energy friction factor f_e was estimated from the wave characteristics. The analysis of the results indicates that f_e is proportional to $\cos^3\theta$ which suggest the value of the drag coefficient C_d to be independent of θ if the drag force is scaled by the square of the reference velocity in the direction perpendicular to the ripple axis, $U_{r\perp}$.

7.1.2 Pure Current Experiments

Velocity measurements were performed when the ripples were placed at $\theta = 0^o, 30^o, 45^o$ and 60^o. The main results obtained in the pure current experiments can be summarized as follows:

1) The measurements presented in Chapter 3 indicate the presence of a component of the velocity in the transverse ($\hat{y}$) direction. At the bottom, the value of the transverse (V) component of the flow is of the same order as the longitudinal (U) component. Further from the bottom, the V - component decreases and the U - component increases. This observation show that the flow close to the bottom is turned towards the direction parallel to the ripple axis.

2) The spatial average profiles show a well-defined logarithmic region within a distance of approximately 7 cm above the bottom. The logarithmic region of the flow was analyzed by fitting a logarithmic velocity profile by the least square method.

The shear velocity and bottom roughness were estimated. The results show that the bottom roughness experienced by the component of the flow in the longitudinal direction, z_{ox}, dep ends strongly on the angle of incidence θ, and is redu than one order of magnitude when θ increases from 0^o to 60^o. In contrast, the bottom roughness obtained from the analysis of the component of the flow in the direction perpendicular to the ripple axis, $z_{o\perp}$, is independent of the angle θ.

3) The flow resistance experienced by the flow incident at an angle to the ripple axis was expressed in terms of a drag force. The drag coefficient obtained is independent of the angle of incidence if the drag force is scaled by the square of the reference velocity in the direction perpendicular to the ripple axis at the elevation of the ripple crest.

7.2 Simple models describing the experiments

In Chapter 4 the concept of a drag force oriented perpendicular to the ripple axis is introduced in the formulation of a simple model to describe the near-bottom flow observed in the pure current experiments.

In the model the bottom shear stress in the direction perpendicular to the ripple axis is balanced by the drag force. The component of the shear stress in the parallel direction to the ripple axis is initially unbalanced and is used to represent a driving force that will induce the fluid to move along the ripple axis. The predicted velocity profiles for the transverse velocity obtained with the simple model show good agreement with the observations.

In Chapter 5 the model was extended to incorporate the presence of waves in the direction of the current corresponding to the experimental conditions. The model was able to predict only qualitatively the transverse velocity structure in experiments performed with beads covering the bottom between roughness elements, but it failed in predicting the wave-current experiments without beads.

7.3 Model for waves and currents propagating in different direction

In Chapter 6 the Grant-Madsen model (1979 and 1986) was modified to incorporate the results observed in the experiments described in the thesis.

The proposed model assumes that the wave-current interaction depends on the direction. The velocity measurements obtained in the experiments have shown that the bottom roughness experienced by the component of the flow in the direction perpendicular to the ripple axis is different than the one experienced by the component of the flow in the direction parallel to the ripple axis.

Based on this observation, the Grant-Madsen model was modified by assuming that the current component in the direction perpendicular to the ripple axis, *i.e*, in the direction of the wave propagation, interacts with the waves accounting for the presence of a wave-generated bedform. Therefore, the flow resistance is mainly due to drag form. In the direction parallel to the ripple axis, the current interacts with the waves as if the bottom were plane and the flow resistance is associated with skin friction.

Due to the differences in the roughness, the component of the current velocity parallel to the ripple axis is relatively larger than the perpendicular component, producing the current velocity to turn towards the ripple axis as the bottom is approached.

As a result of the model formulation , the current velocity outside the wave boundary layer consists on two components. The component in the direction of the driving pressure gradient behaves logarithmically. The other component, u_n, is in the direction perpendicular to the driving pressure gradient and is independent on the height above the bottom. By adding the constant component, the current velocity behaves quasilogarithmically, and the angle between the current and the direction of the wave propagation ,ϕ_{wc}, depends on the height above the bottom. An illustrative example was presented in section 6.2.3 where the waves were represented by a near orbital velocity $u_b = 15.3$ cm/sec ,a period $T = 11.2$ sec and the ripple height was $eta = 1.72$

cm. For these particular conditions and under the assumption of a wave dominated environment the normal component of the velocity is expected to be $u_n \approx 0.3\ u_c(z_r =$ 1 m) when the angle between the waves and the driving pressure gradient, ϕ_s, is between 30^o to 60^o.

The direction of the current outside the wave boundary layer depends on the height. Within 1 m above the bottom the variability of the angle between the waves and the current, $\Delta\phi_{wc}$, was estimated for the case of a wave dominated environment. It was obtained that $\Delta\phi_{wc} \approx 15^o$ to 7^o when the angle ϕ_s varies from 30^o to 60^o. The maximum variability was found to be of the order of $\Delta\phi_{wc} \approx 18^o$ when $\phi_s \approx 20^o$. This variability is bigger than the error in general estimated of $\pm 5^o$ in the determination of ϕ_{wc} in field experiments. This result implies that an angular inconsistency obtained by the instrumentation does not necessarily mean an error in the measurement . Another consequence of the presence of a normal component of the velocity, u_n, is that the angle between the waves and the current, ϕ_{wc}, is different from the angle between the waves and the direction of the driving pressure gradient , ϕ_s.

The laboratory experiments of Ranasoma and Sleath (1994) were used to test the model in the limiting case of wave and currents at a right angle. The velocity profile predicted by the model show an excellent agreement with their Test 109. This result supports the assumption that for the limiting case of waves and current at a right angle there is no wave-current interaction in the direction perpendicular to the ripple axis.

Available experimental field data presented by Sorenson (1995) was used to test the model. Twelve experiments were analyzed in which the angle between the waves and the current, ϕ_{wc}, varied between 80^o to 10^o approximately. It was further shown that the present model was superior to the conventional application of the Grant-Madsen model with a single-valued bottom roughness in representing Sorensons's data. The ability of the present model to reproduce the angle dependence is based on the addition of the near-bottom velocity component parallel to the ripple axis.

The proposed model was also compared to the field data obtained by Drake and Cacchione (1992) and Trowbridge and Agrawall (1995). Overall, the predictions ob-

tained from the model are encouraging. Laboratory or extensive well designed field experiments are, however, required to further test the proposed model before it can be applied with complete confidence for the prediction of near-bottom turbulent flows of combined waves and currents over a wave-rippled movable bed.

Appendix A

Additional Velocity Maesurements

In Chapter 3 the velocity measurements performed in the experiments without beads when the current was incident at an angle $\theta = 45^o$ were presented and compared to the velocity profile measured at the center of the flume obtained when $\theta = 30^o$ and 45^o. The pure current experiments with beads and no beads that were performed and not described in Chapter 3 are presented graphically in this appendix.

The pure wave amplitude and phase profiles were described in Chapter 3 for the experiments without beads. In this appendix the pure wave velocity measurements are presented graphically.

PURE CURRENT

Detailed Velocity Profiles Between Two Crests:

Figure A-1: **Experiments WITH BEADS**..... $\theta = 45^o$

Figure A-2: **Experiments WITHOUT BEADS**.. $\theta = 30^o$

Figure A-3: **Experiments WITH BEADS**..... $\theta = 30^o$

Figure A-4: **Experiments WITHOUT BEADS**.. $\theta = 60^o$

Figure A-5: **Experiments WITH BEADS**..... $\theta = 60^o$

Spatial Average Profiles

Figure A-6: **Experiments WITH BEADS**..... $y = b/2$ vs. θ

Figure A-7: **Experiments WITH BEADS**..... $\theta = 45^o$ vs. y/b

Figure A-8: **Experiments WITH BEADS**..... $\theta = 30^o$ vs. y/b

PURE WAVE $\theta = 45^o$:

Spatial Average Profiles

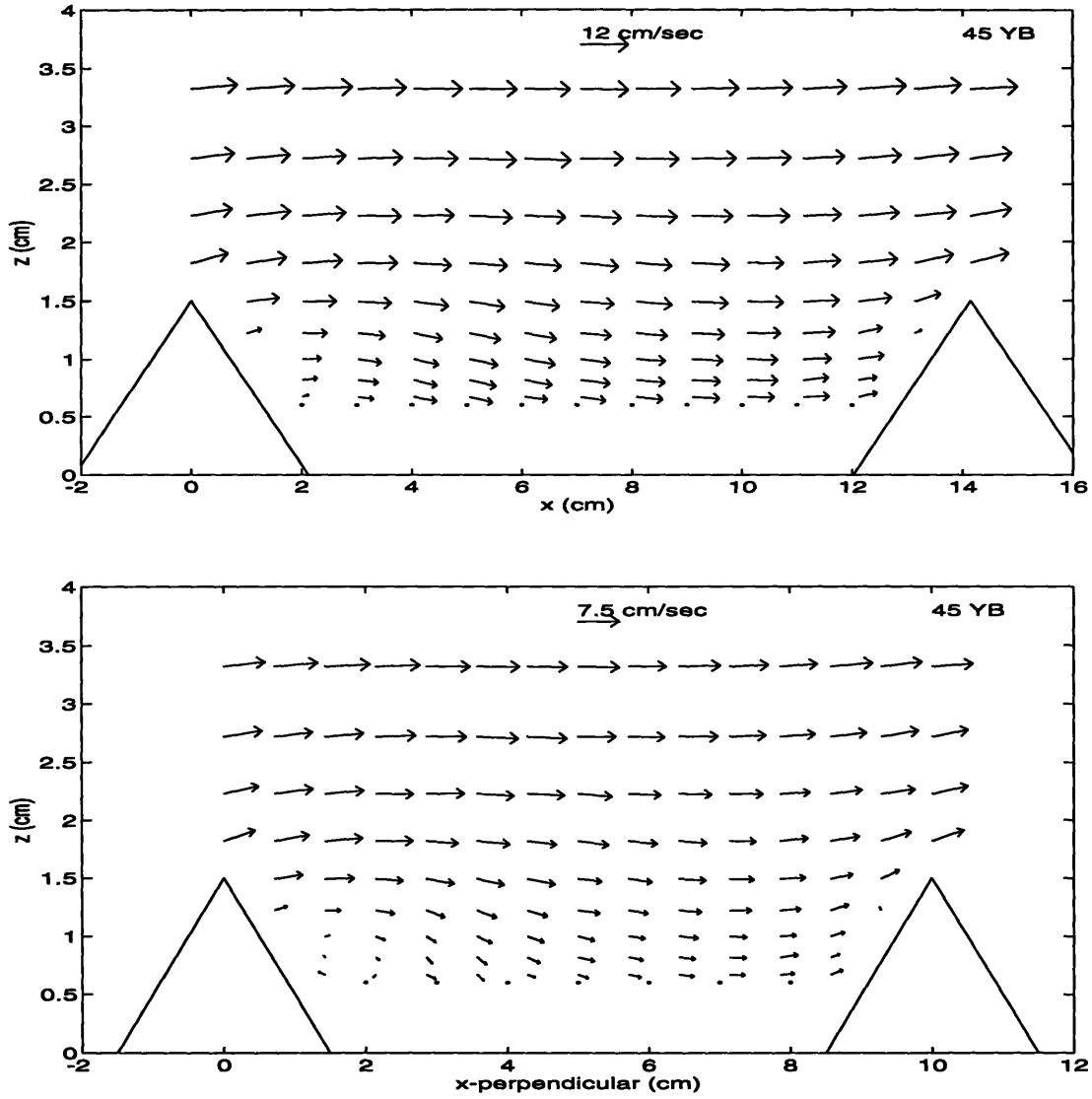

Figure A-1: Detailed Velocity Field between two ripple crests in the Experiments WITH BEADS for $\theta = 45^o$. Vector plot of the (U, W) velocity components (top). Vector plot of the $(U_\perp, W)$ velocity components (bottom). The dotted line represents the top of the beads ($d = 0.\ 64$ cm)

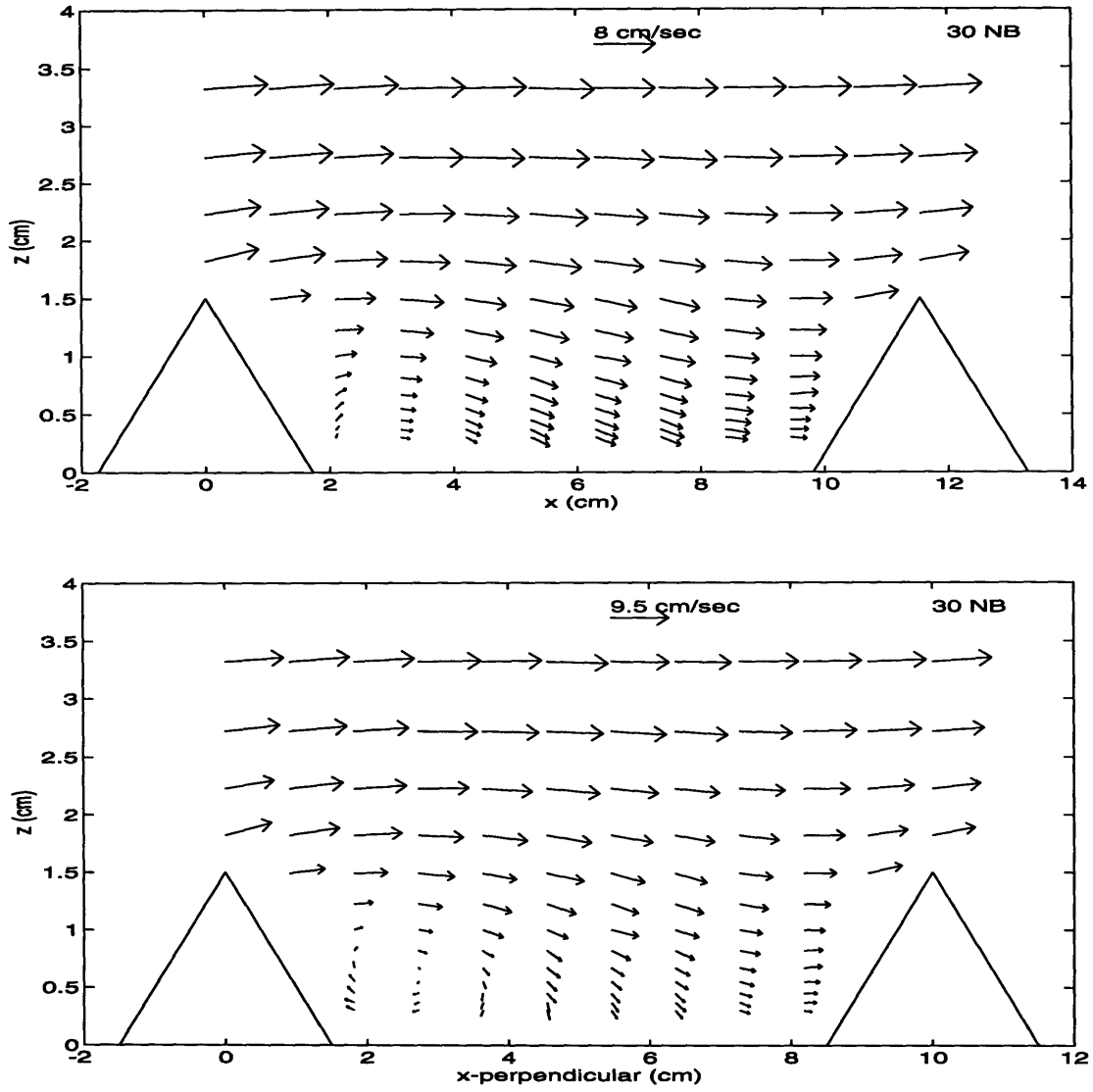

Figure A-2: Detailed Velocity Field between two ripple crests in the Experiments WITHOUT BEADS for $\theta = 30^o$. a) Vector plot of the (U, W) velocity components (top). Vector plot of the $(U_\perp, W)$ velocity components (bottom).

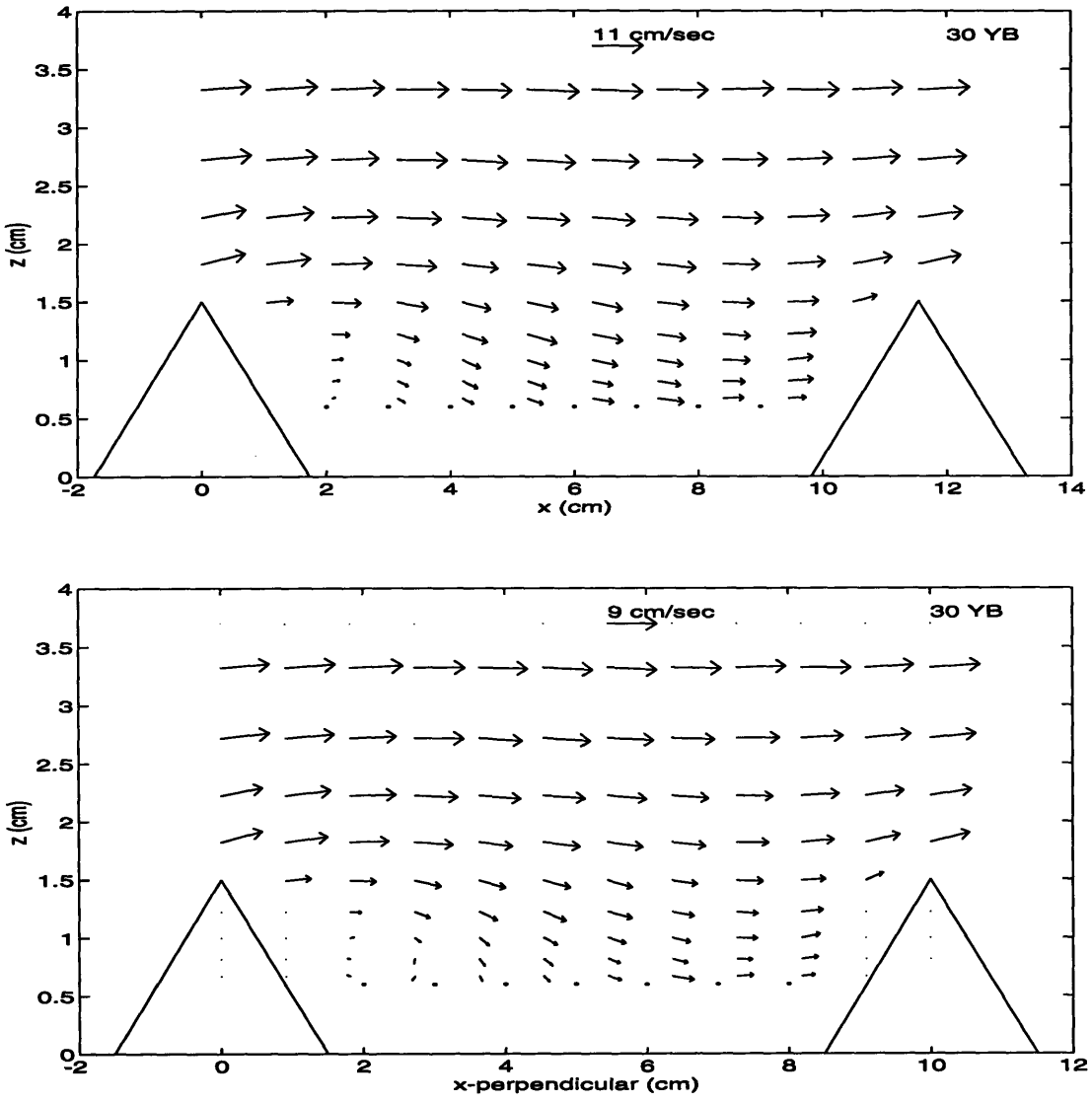

Figure A-3: Detailed Velocity Field between two ripple crests in the Experiments WITH BEADS for $\theta = 30^{o}$. a) Vector plot of the (U, W) velocity components (top). Vector plot of the $(U_{\perp}, W)$ velocity components (bottom). The dotted line represents the top of the beads ($d = 0.\ 64$ cm)

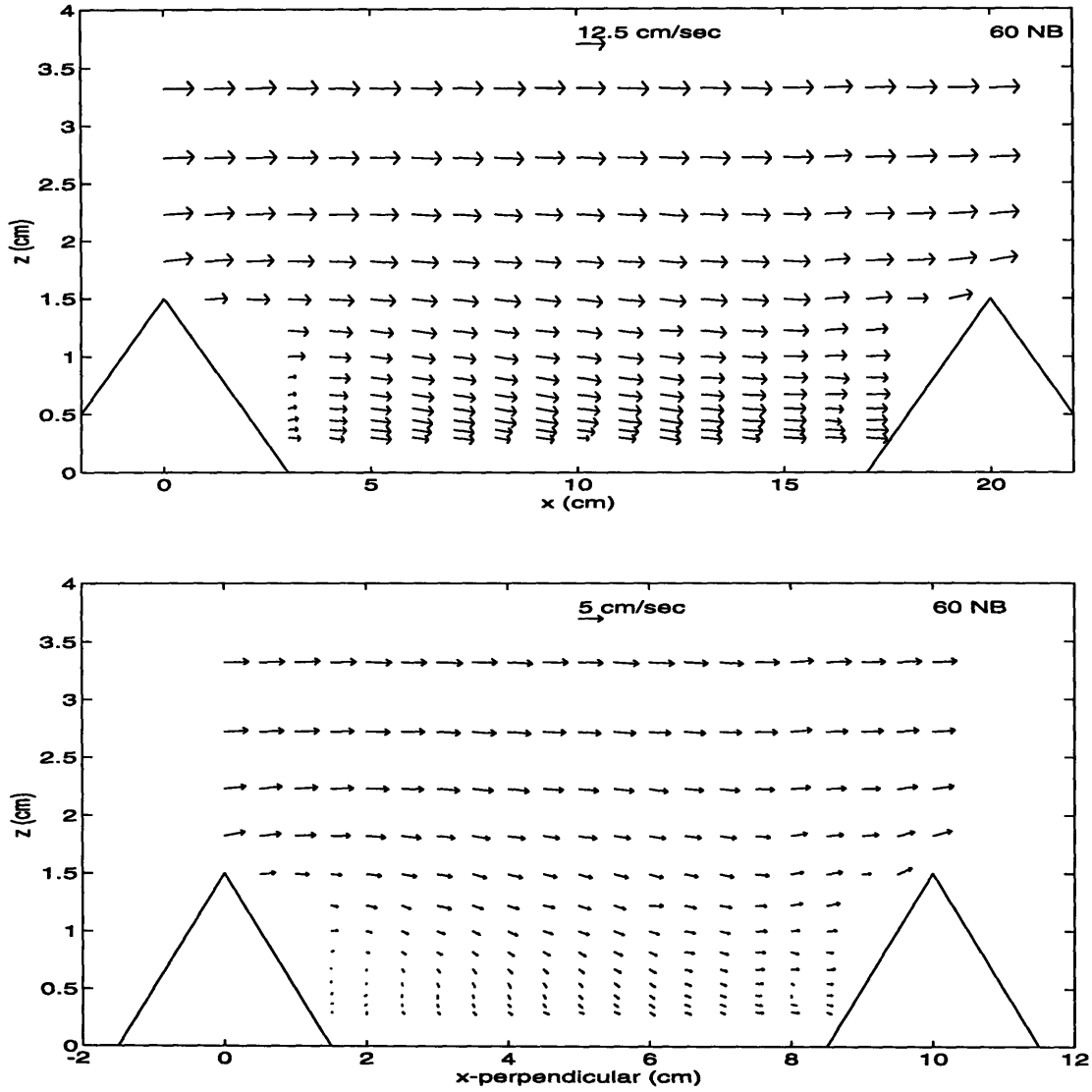

Figure A-4: Detailed Velocity Field between two ripple crests in the Experiments WITHOUT BEADS for $\theta = 60°$. a) Vector plot of the (U, W) velocity components (top). Vector plot of the $(U_\perp, W)$ velocity components (bottom).

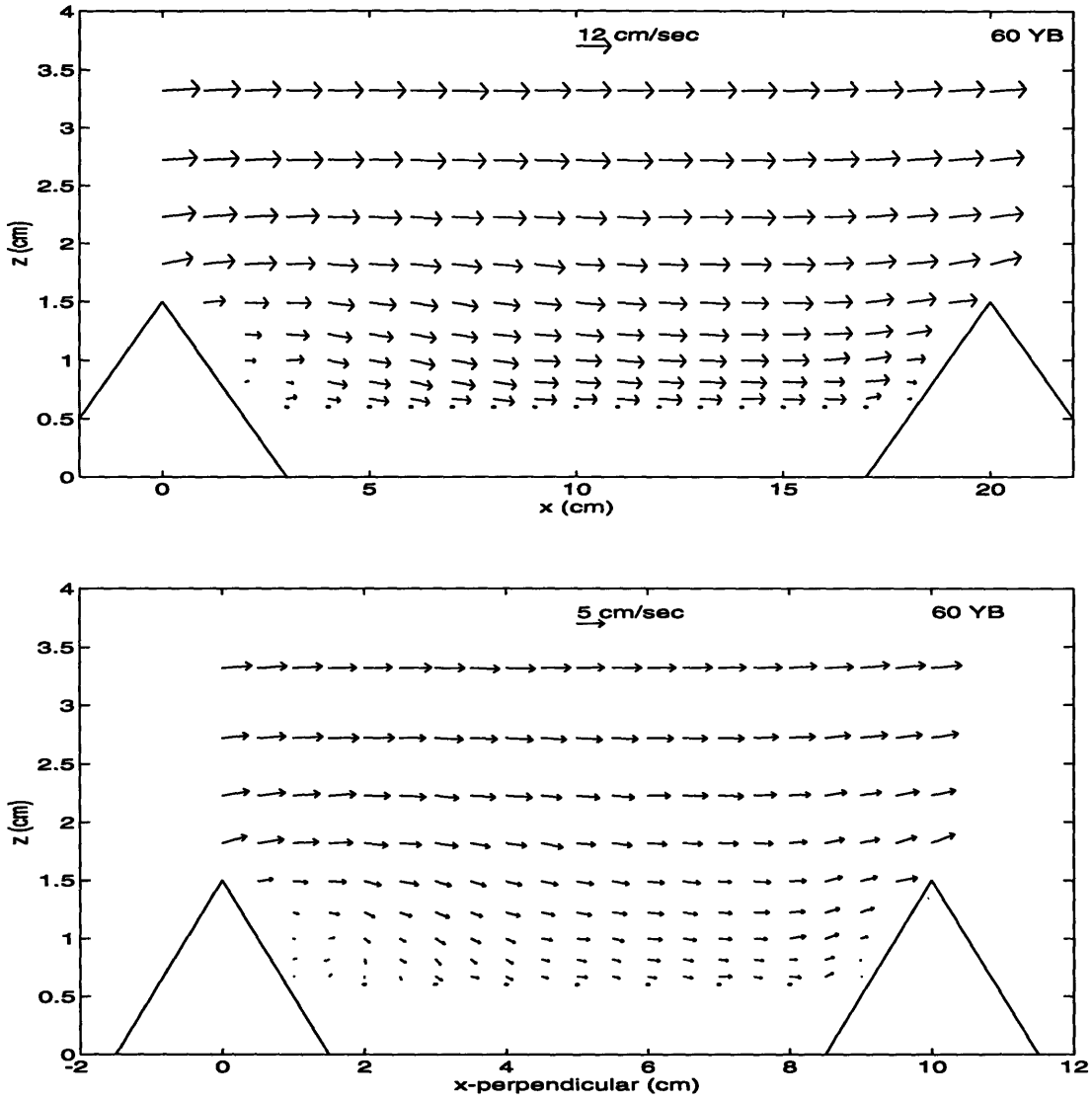

Figure A-5: Detailed Velocity Field between two ripple crests in the Experiments WITH BEADS for $\theta = 60^o$. a) Vector plot of the (U, W) velocity components (Top). Vector plot of the $(U_\perp, W)$ velocity components (bottom). The dotted line represents the top of the beads ($d = 0.\ 64$ cm)

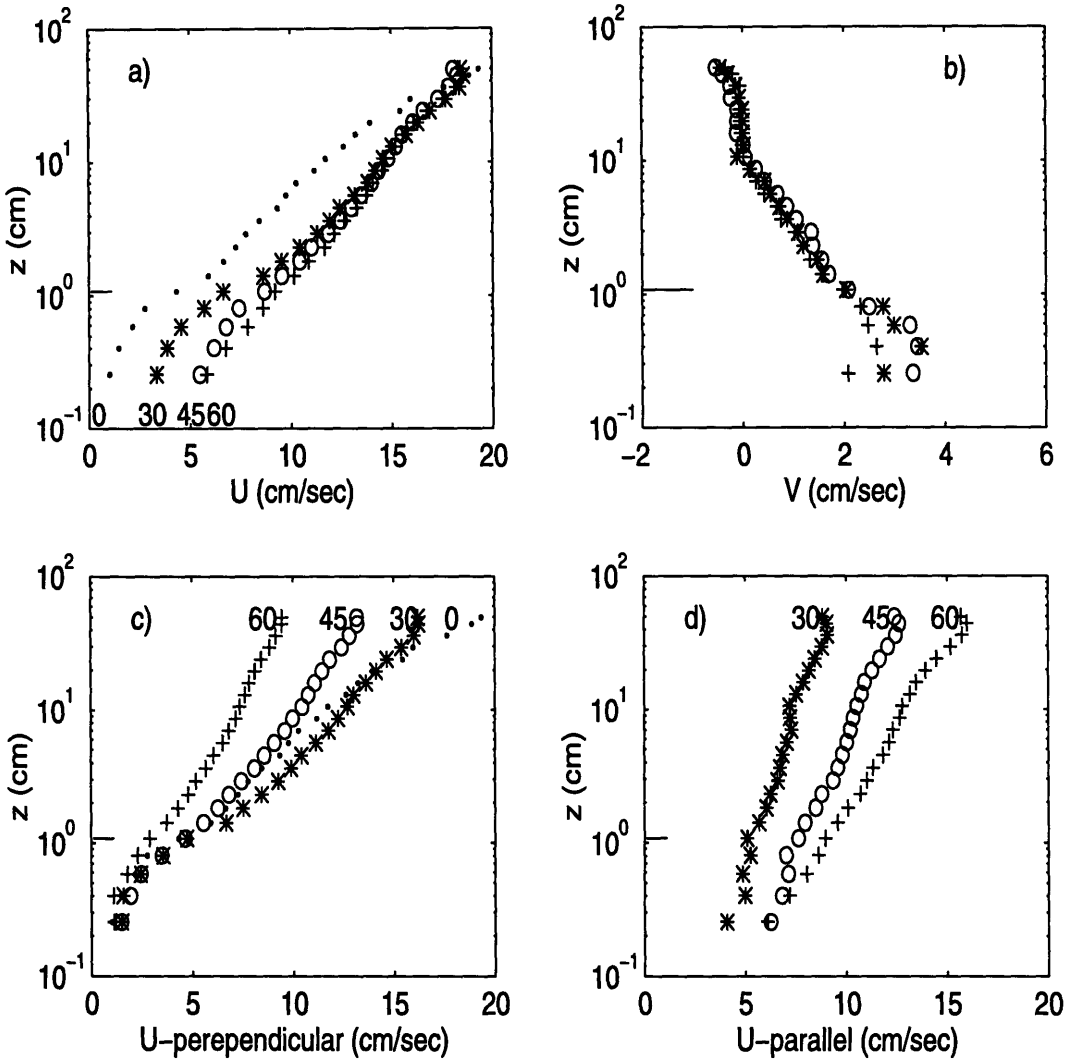

Figure A-6: Spatial average velocity profiles of the experiments WITH BEADS at the center of the flume, $y/b = 1/2$, as a function of the angle θ. a) U, b) V, c) $U_\perp$ and d) $U_\parallel$ - component. The symbols correspond to the different ripple configurations used: ... $\theta = 0^o$, * $\theta = 30^o$, o $\theta = 45^o$, + $\theta = 60^o$. The top of the roughness element is indicated by the horizontal solid line

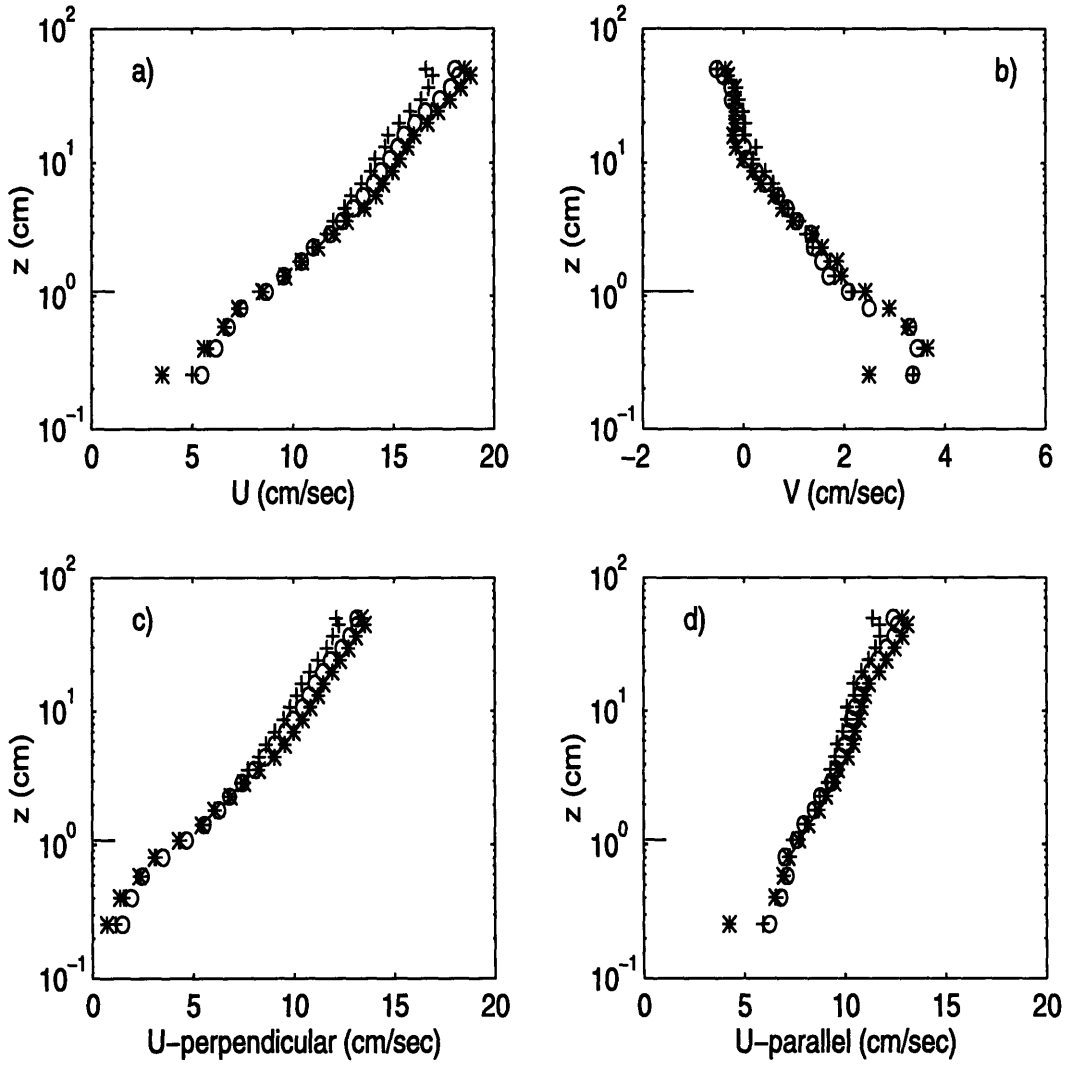

Figure A-7: Spatial average velocity profiles of experiments WITH BEADS as a function of y measured for $\theta = 45^o$. a) U, b) V, c) $U_\perp$ and d) $U_\parallel$ - component. The symbols correspond to + $y/b = 3/8$, o $y/b = 1/2$ and * $y/b = 5/8$. The top of the roughness element is indicated by the horizontal solid line.

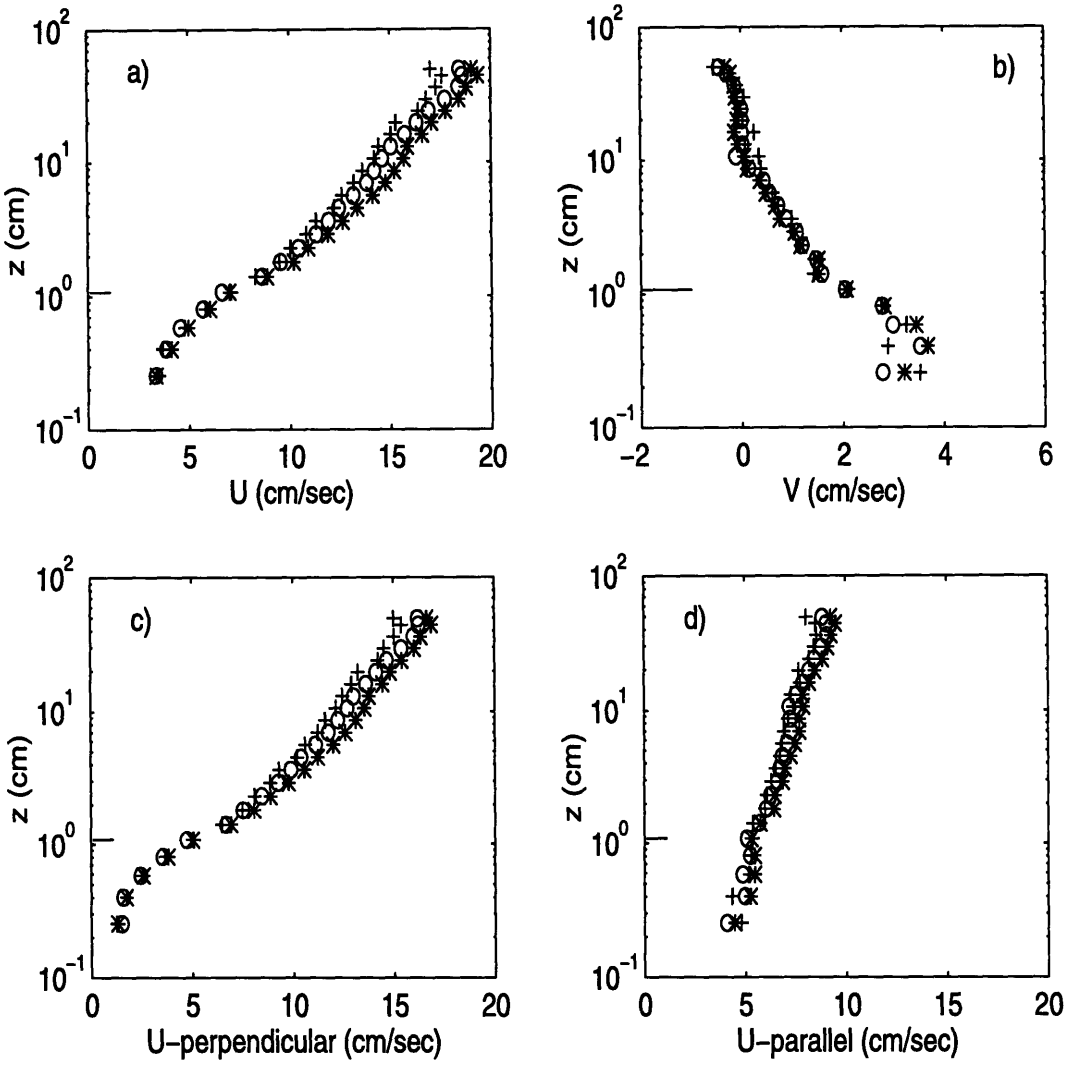

Figure A-8: Spatial average velocity profiles of experiments WITH BEADS as a function of y measured for $\theta = 30^o$. a) U, b) V, c) $U_\perp$ and d) $U_\parallel$ - component. The symbols correspond to + $y/b = 3/8$, o $y/b = 1/2$ and * $y/b = 5/8$. The top of the roughness element is indicated by the horizontal solid line.

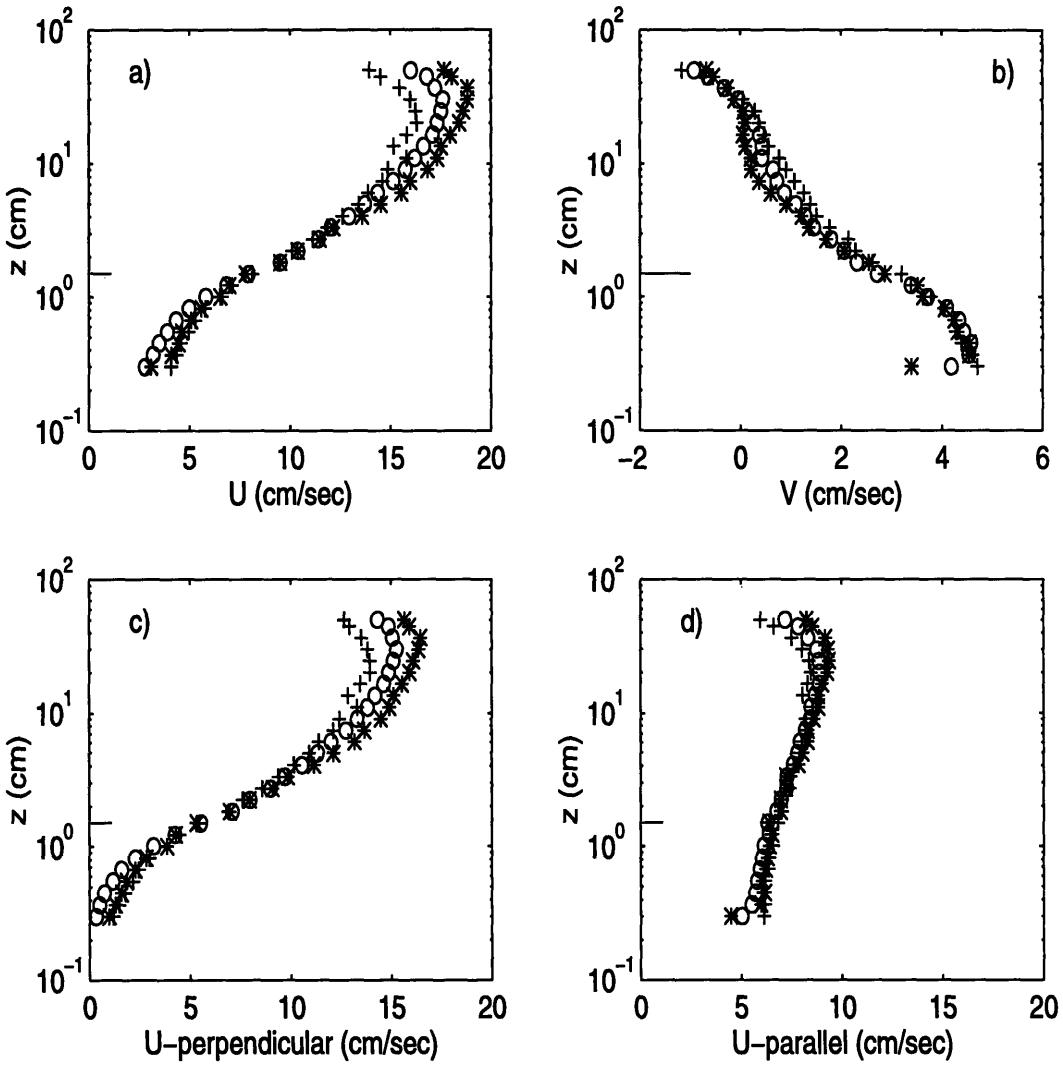

Figure A-9: Spatial average velocity profiles of experiments WITHOUT BEADS as a function of y measured for $\theta = 30^o$. a) U, b) V, c) $U_\perp$ and d) $U_\parallel$ - component. The symbols correspond to + $y/b = 3/8$, o $y/b = 1/2$ and * $y/b = 5/8$. The top of the roughness element is indicated by the horizontal solid line.

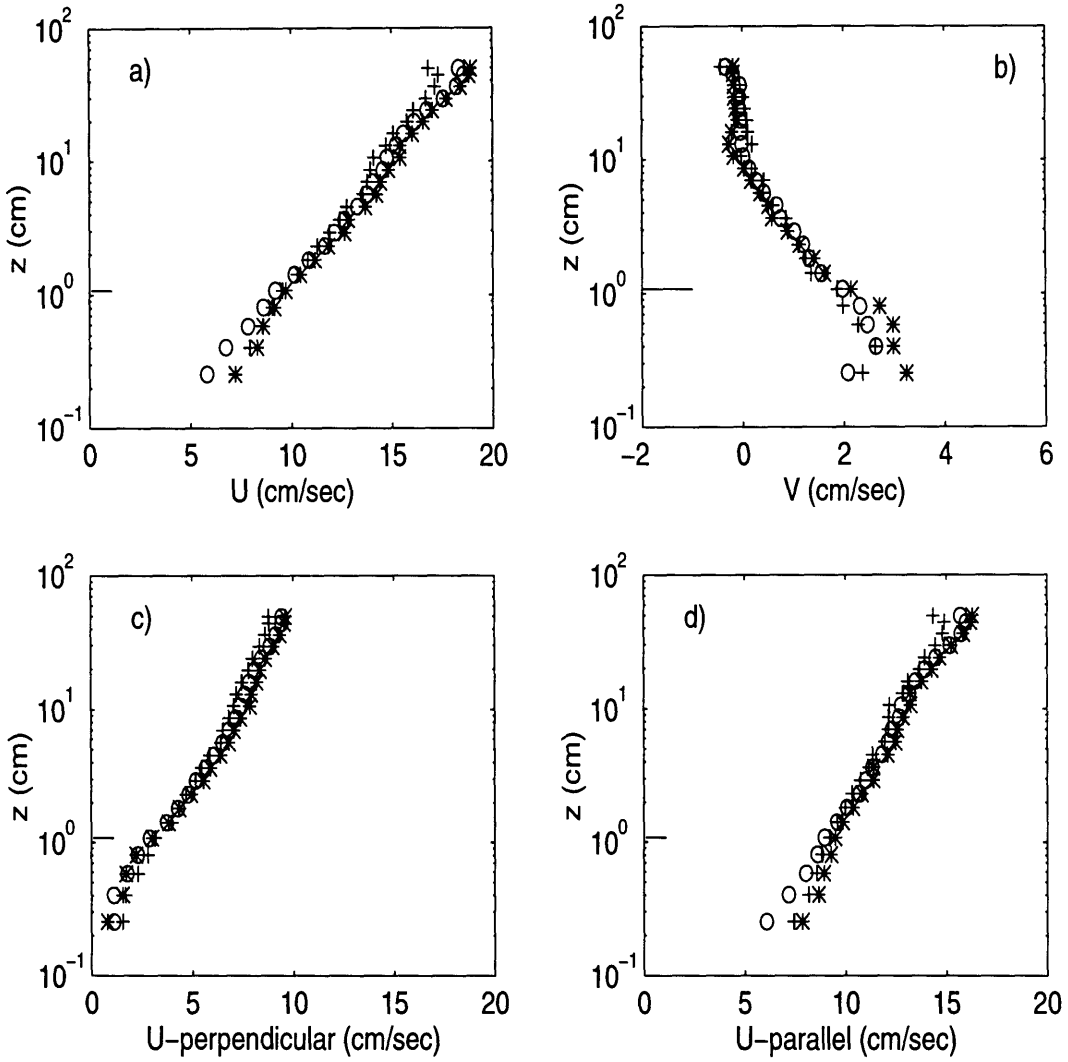

Figure A-10: Spatial average velocity profiles of experiments WITH BEADS as a function of y measured for $\theta = 60^o$. a) U, b) V, c) $U_\perp$ and d) $U_\parallel$ - component. The symbols correspond to + $y/b = 3/8$, o $y/b = 1/2$ and * $y/b = 5/8$. The top of the roughness element is indicated by the horizontal solid line.

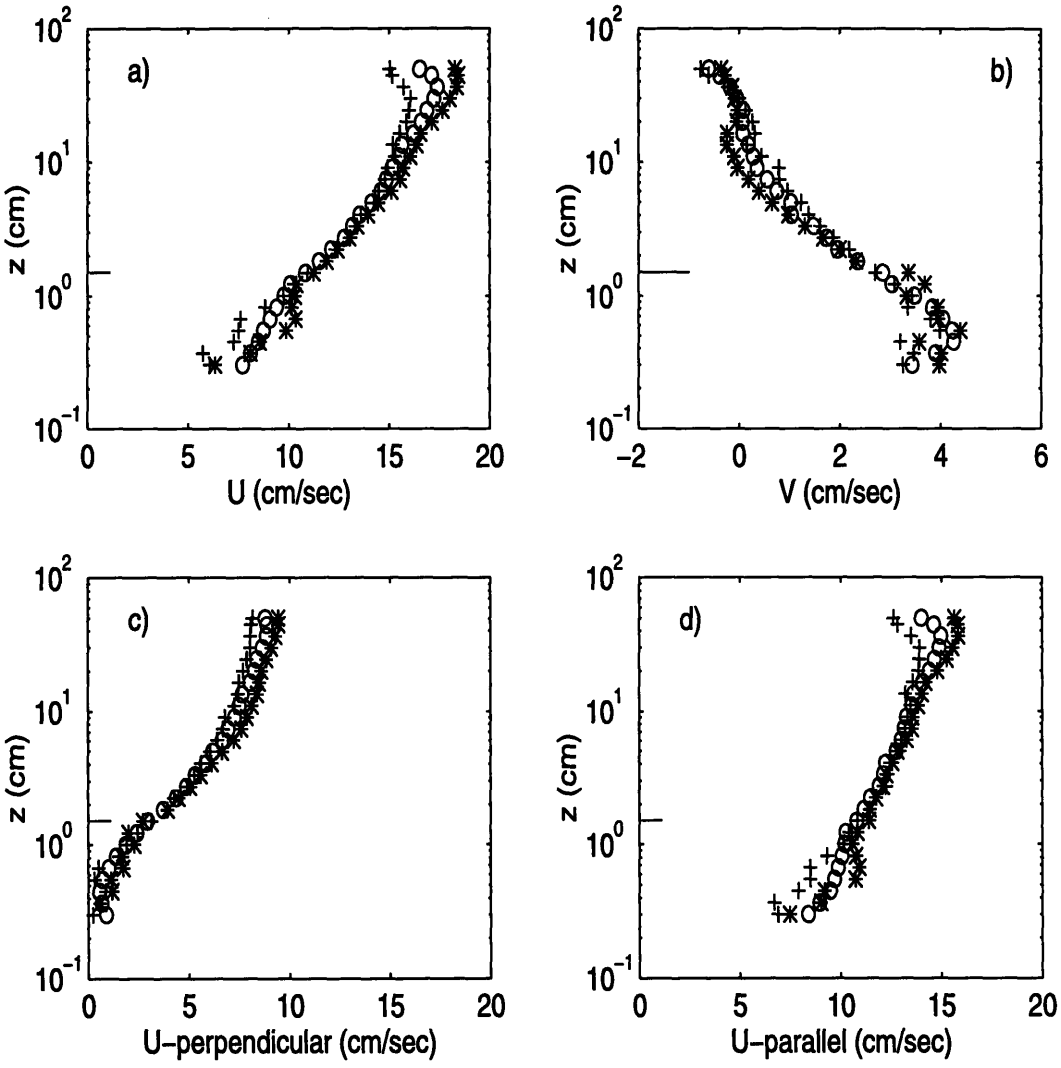

Figure A-11: Spatial average velocity profiles of experiments WITHOUT BEADS as a function of y measured for $\theta = 60^o$. a) U, b) V, c) $U_\perp$ and d) $U_{||}$ - component. The symbols correspond to + $y/b = 3/8$, o $y/b = 1/2$ and * $y/b = 5/8$. The top of the roughness element is indicated by the horizontal solid line.

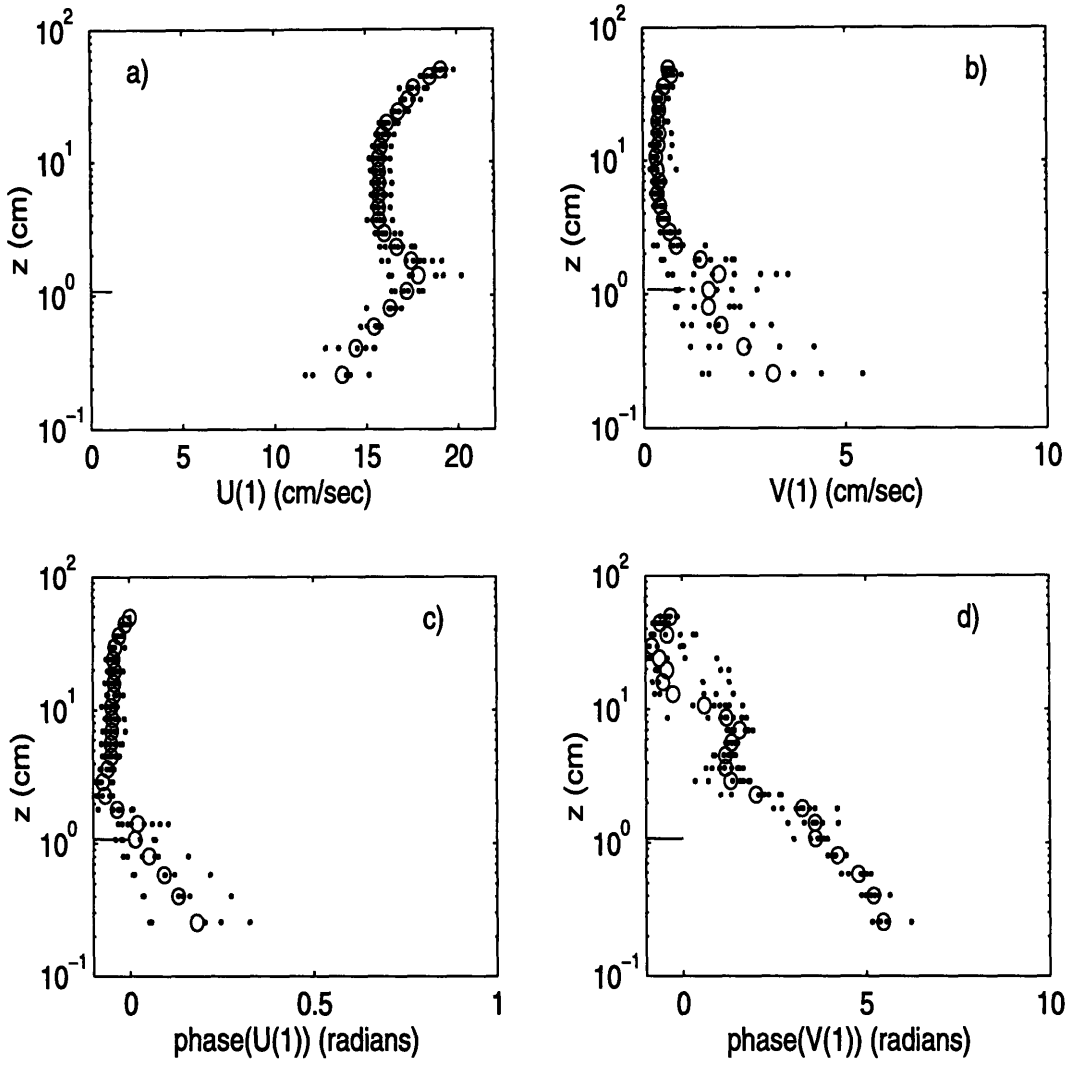

Figure A-12: First harmonic of the wave amplitude and phase measured for the case of $\theta = 45^o$ in the experiments WITH BEADS. a) $U_{(1)}$ is the amplitude of the component of the velocity in the $\hat{x}$ - direction. b) $V_{(1)}$ is the amplitude of the component of the velocity in the $\hat{y}$ - direction. c) phase of the velocity component in the $\hat{x}$ - direction. d) phase of the velocity component in the $\hat{y}$ - direction.

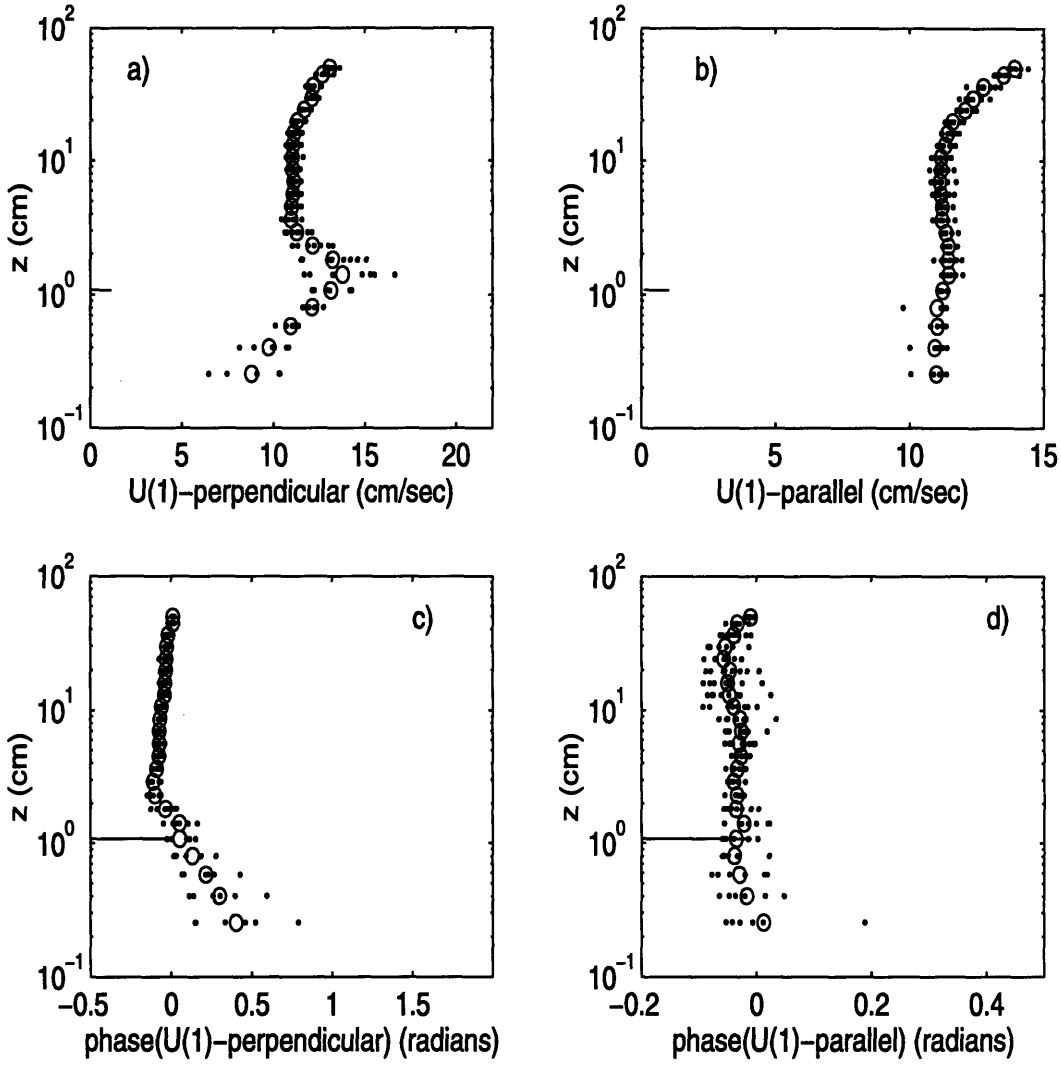

Figure A-13: First harmonic amplitude and phase for the case of $\theta = 45^o$ in the experiments WITH BEADS. a) $U_{(1)\perp}$ the amplitude of the component of the velocity in the $\hat{x}-$ $\perp$ - direction. b) $U_{(1)\|}$ the amplitude of the component of the velocity in the $\hat{x}_{\|}$ - direction. c) phase of the velocity component in the $\hat{x}_{\perp}$ - direction. d) phase of the velocity component in the $\hat{x}_{\|}$ - direction.

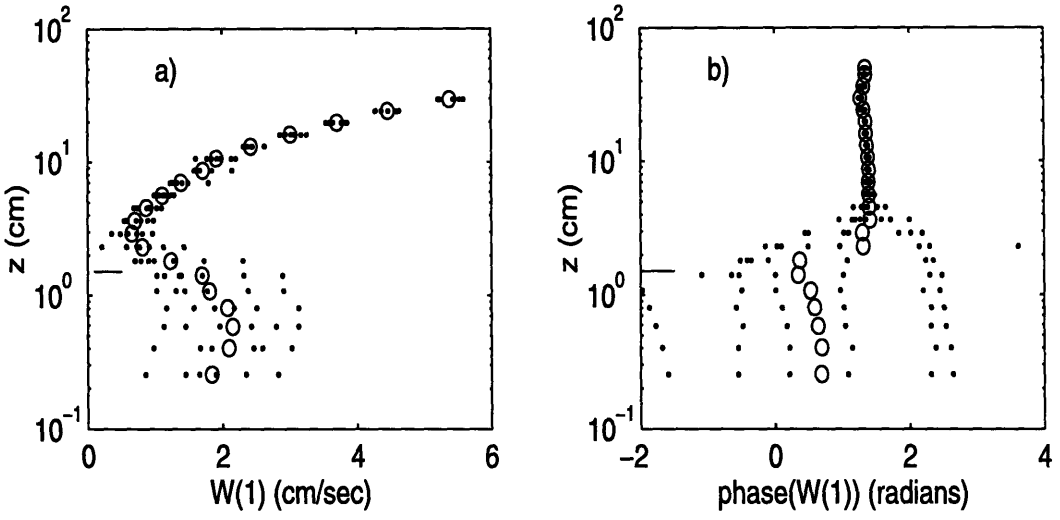

Figure A-14: First harmonic wave amplitude and phase of the component of the wave velocity in the $\hat{z}$ direction obtained for $\theta = 45^o$ in the experiments WITH BEADS

Appendix B

Details of the Numerical Scheme used in the Pure Current model

In order to solve Eqs. (4.20) to (4.26) numerically, the physical variables consisting of $u_{\|}$, the time t, and the distance above the bottom z in the equations, are non-dimensionalized by defining the new variables:

$$\begin{aligned} u &= \frac{u_{\|}\ \kappa}{u_*\ \sin\theta} \\ Z &= \frac{z}{\eta} \\ T &= t\,\frac{\kappa u_*}{\eta} \end{aligned}$$

The flow depth is divided into two regions: the lower region defined as $Z_o \leq Z \leq 1$, and the upper region defined as $1 < Z \leq H$, where $Z_o = z_o'/\eta$ and $H = h/\eta$. The dimensionless parallel component of the velocity in the lower region is denoted by U_1 and the one in the upper region by U_2. One difficulty in solving the equations is that the velocity has a logarithmic singularity as $z_o' \to 0$. This difficulty can be avoided by making the change of variable:

$$Z_1 = \ln\frac{Z}{Z_o} \tag{B.1}$$

Using the change of variables Eqs. (4.20) and (4.21) becomes:

$$\frac{\partial U_1}{\partial T} = 1 + \sqrt{\alpha}\sqrt{\sin\theta}\,\frac{e^{-Z_1}}{Z_o}\,\frac{\partial^2 U_1}{\partial Z_1^2} \tag{B.2}$$

for the lower region: $0 \leq Z_1 \leq 1$, and

$$\frac{\partial U_2}{\partial T} = \frac{\partial}{\partial Z}\left[Z(1 - \frac{Z}{H})\frac{\partial U_2}{\partial Z}\right] \tag{B.3}$$

for the upper region: $1 < Z \leq H$.

Eqs. (B.2) and (B.3) are solved numerically by using a finite difference method. The spatial derivatives are discritized using second order accurate (i.e. $O(\Delta Z^2)$ where ΔZ is the grid spacing) centered difference formulae. The equations are time stepped with a standard explicit Euler scheme (Press *et. al.* (1992)). Different grid spacings are used for the upper and lower regions of the flow. For the lower region the grid spacing used is $h_1 = 1/(N_1 - 1)$ and for the upper region $h_2 = (H-1)/(N_2 - 1)$. The convergence of the solution was studied by increasing the number of points in each region and decreasing the time step, dT. As a result of this study, it was found that a good solution was obtained when the number of points used was $N_1 = 40$, $N_2 = 200$, and $dT \approx 10^{-4}$ for the experiments with beads and $dT \approx 10^{-5}$ for the experiments without beads.

The boundary condition in Eq. (4.26), continuity of the shear stress at $z = \eta$, is written in the dimensionless variables as:

$$\sqrt{\alpha}\sqrt{\sin\theta}\,\frac{\partial U_1}{\partial Z_1} = Z(1 - \frac{Z}{H})\frac{\partial U_2}{\partial Z} \tag{B.4}$$

To obtain an expression for the first derivative of the velocity at $z = \eta$ in Eq. (B.4), a second order polynomial was used with its origin at the grid point respresenting $z = \eta$.

The velocity in the lower region was expressed as $U_1 = A_1 Z_1^2 + B_1 Z_1 + C_1$, and the velocity in the upper region as $U_2 = A_2 Z^2 + B_2 Z + C_2$. To obtain the coefficients

for the lower region (N_1 corresponds to $z = \eta^-$):

$$\begin{aligned} U_1(N_1) &= C_1 \\ U_1(N_1 - 1) &= A_1 h_1^2 - B_1 h_1 + C_1 \\ U_1(N_1 - 2) &= A_1 4h_1^2 - B_1 2h_1 + C_1 \end{aligned} \tag{B.5}$$

and for the upper region ($N_2 = 1$ corresponds to $z = \eta^+$):

$$\begin{aligned} U_2(1) &= C_2 \\ U_2(2) &= A_2 h_2^2 + B_2 h_2 + C_2 \\ U_2(3) &= A_2 4h_2^2 + B_2 2h_2 + C_2 \end{aligned} \tag{B.6}$$

Solving Eq. (B.5) and (B.6) the coefficients B_1 and B_2 are obtained:

$$B_1 = \frac{\partial U_1(\eta)}{\partial Z_1} = \frac{-4U_1(N_1 - 1) + U_1(N_1 - 2) + 3U_1(N_1)}{2h_1} + O(h_1^2) \tag{B.7}$$

$$B_2 = \frac{\partial U_2(\eta)}{\partial Z} = \frac{4U_2(2) - U_2(3) - 3U_2(1)}{2h_2} + O(h_2^2) \tag{B.8}$$

Eqs (B.7) and (B.8) give an expression of the derivative of the lower and upper flow velocities at $z = \eta$ with the same accuracy of $O(h_i^2)$ as the one used in the numerical scheme. The same procedure was used to express the derivative of the velocity at $z = z_o'$ to obtain the time dependent component of the shear stress Eq. (4.16) and evaluate the parameter α.

Bibliography

[1] Anderson, S., A. Lohrmann. 1994. Open water test of the SonTek acoustic Doppler velocimeter, IEEE Fifth Working Conference on Current Measurement.

[2] Bakker, W. T., T. van Doorn. 1978. Near-bottom velocities in waves with a current. Proc. 16th Int. Conf. Coast. Eng., pp. 1394-1413.

[3] Christoffersen, J. B. , I. G. Jonsson. 1985. Bed friction and dissipation in a combined current and wave motion, *Ocean Engng* 12 (5):387-423.

[4] Davies, A. G., R. L., Soulsby, H. L., King. 1988. A numerical model of the combined wave and current bottom boundary layer. *J. Geophys. Res.* 93 (C1):491-508.

[5] Drake, D. E., D. A. Cacchione, W. D. Grant. 1992. Shear stress and bed roughness estimates for combined wave and current flows over rippled bed. *J. Geophys. Res.* 97 (C2):2319-2326.

[6] Einstein, H. A., H. Li. 1958. Secondary Currents in Straight Channels. *Transaction American Geophysical Union* 39(6):1085-1088.

[7] Grant, W. D., O. S. Madsen. 1979. Combined wave and current interaction with a rough bottom, *J. Geophys. Res.* 84 (C4):1797-1808.

[8] Grant, W. D., O. S. Madsen. 1982. Movable bed roughness in unsteady oscillatory flow, *J. Geophys. Res.* 87 (C1): 469-481.

[9] Grant, W. D., O. S. Madsen. 1986. The continental-shelf bottom boundary layer , *Annual Review of J. Fluid Mech* 18:265-305.

[10] Jackson, P. S. 1981. On the displacement height in the logarithmic velocity profile. *J. Fluid Mech.* 111: 15-25.

[11] Kajiura, K. 1968. A model of the bottom boundary layer in water waves. *Bulletin of the Earthquake Reasearch Institute* 46. pp 75-123.

[12] Kemp, P. H., R. R. Simons. 1982. The interaction of waves and a turbulent current: waves propagating with the current, *J. Fluid. Mech* 116:227-250.

[13] Kemp, P. H., R. R. Simons. 1983. The interaction of waves and a turbulent current: waves propagating against the current, *J. Fluid. Mech* 130:73-89.

[14] Kraus, N. C., A. Lohrmann, R. Cabrera. 1994. New acoustic meter for measuring 3D laboratory flows, *Journal of Hydraulic Engineering*, 120 (3):406-412.

[15] Lundgren, H. 1972. Turbulent currents in the presence of waves. Proc. 13 th Int. Conf. Coastal Eng. Chap. 33, pp 623-634.

[16] Madsen, O. S. 1991. Combined wave-current flows over a rippled bottom: Theoretical considerations (abstract), . *Eos Trans. AGU 72* (44), Fall Meet. suppl., 299.

[17] Madsen, O. S. 1994. Spectral wave-current bottom boundary layer flows, Proc. 24 th Int. Conf. Coastal Eng. Res. Council/ASCE, Held October 23-28, Kobe, Japan, pp 384-398.

[18] Mathisen, P. P. 1989. Experimental study on the response of fine sediments to wave agitation and associated wave attenuation. M.S. thesis, MIT.

[19] Mathisen, P. P., O. S. Madsen. 1996. Waves and currents over a fixed rippled bed, 1, Bottom roughness experienced by waves in the presence and absence of currents, *J. Geophys. Res.* 101 (C7):16,533-16,542.

[20] Mathisen, P. P., O. S. Madsen. 1996. Waves and currents over a fixed rippled bed, 2, Bottom roughness experienced by currents in the presence of waves, *J. Geophys. Res.* 101 (C7):16,543-16,550.

[21] McLean, S. R. 1981. The role of non-uniform roughness in the formation of sand ribbons. *Marine Geology* 42:49-74.

[22] W.H. Press, W. H., Teukolsky, S. A., Vetterling W. T., and Flannery , B. P. *Numerical Recipes.* Cambridge University Press, 1992

[23] Ranasoma, K. I. M., J. F. A. Sleath. 1994. Combined oscillatory and steady flow over ripples, *Journal of Waterway, Port, Coastal, and Ocean Enigineering* 120 (4):331-346.

[24] Rosengaus, M. 1987. Experimental study on wave generated bedforms and resulting wave attenuation. Ph.D. thesis, MIT.

[25] Schlichting, H. 1968. Boundary layer Theory, 6th ed., McCraw-Hill

[26] Simons, R. R., T. J. Grass, M. Mansour-Tehrani. 1992. Bottom shear stresses in the boundary layers under waves and currents crossing at right angles. Proc. 23 rd Conf. on Coastal Eng. ASCE, pp 604-617.

[27] Sleath, J. F. A. 1991. Velocities and shear stresses in wave-current flows. *J. Geophys. Res.* 96 (C8):15,237-15,244.

[28] Smith, J. D., S. R. McLean. 1977. Spatially averaged flow over a wavy surface, *J. Geophys. Res.* 82 (12):1735-1746.

[29] Smith, J. D. 1977. Modelling of sediment transport on continental shelves. In *The sea*, Vol 6, Interscience, N. Y., pp 538-577.

[30] Sorenson, K. S. 1995. Moveable bed roughness and sediment resuspention in the field. M.S. thesis, MIT.

[31] Tanaka, H., N. Shuto 1981. Friction coefficient for a wave-current coexisting system. *Coastal Engineering in Japan* 24:105-128.

[32] Townsend, A. A. 1956. The Structure of Turbulent Shear Flow, Cambridge University Press, Cambridge, England, pp 258.

[33] Tracy, H. J. 1965. Turbulent Flow in a Three-Dimensional Channel. Journal of the Hydraulics Division, ASCE, Vol. 91, No. HY6, Proc. Paper 4530, pp. 9-35.

[34] Trowbridge, J. H., Y. C. Agrawal. 1995. Glimpses of a wave boundary layer. *J. Geophys. Res.* 100 (C10):20,729-20,743.

[35] Wiberg, P. L., D. M. Rubin. 1989. Bed roughness produced by saltating sediment, *J. Geophys. Res.* 94:5011-5016.

[36] Wiberg, P. L., C. K. Harris. 1994. Ripple geometry in wave-dominated environments, *J. Geophys. Res.* 99 (C1):775-789.

[37] Wikramanayake, P. N. 1993. Velocity profiles and Suspended Sediment transport in wave-current flows. PhD thesis, MIT.